AD-A141 960 PHASE CONJUGATE OPTICS(U) HUGHES RESEARCH LABS MALIBU CA G J DUNNING ET AL. FEB 84 RADC-TR-84-18 F19628-80-C-0185 1/3

UNCLASSIFIED F/G 20/6 NL

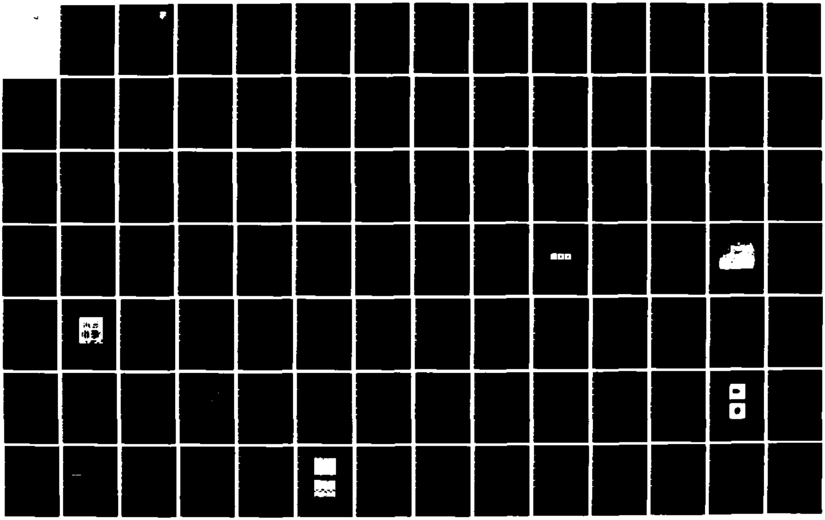

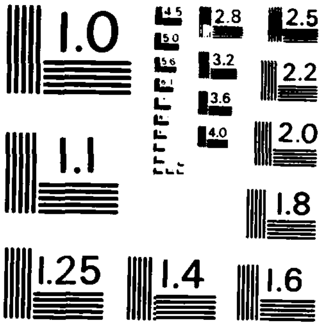
1.0
4.5
5.0
5.6
2.8
3.2
3.6
4.0
2.5
2.2
2.0
1.1
1.8
1.25
1.4
1.6

MICROCOPY RESOLUTION TEST CHART
NATIONAL BUREAU OF STANDARDS-1963-A

12

AD-A141 960

RADC-TR-84-18
Final Technical Report
February 1984

PHASE CONJUGATE OPTICS

Hughes Research Laboratories

G. J. Dunning
M. B. Klein
R. C. Lind

BTIC FILE COPY

APPROVED FOR PUBLIC RELEASE; DISTRIBUTION UNLIMITED

DTIC
ELECTE
JUN 1 1 1984
S D
E

ROME AIR DEVELOPMENT CENTER
Air Force Systems Command
Griffiss Air Force Base, NY 13441

84 06 08 002

This report has been reviewed by the RADC Public Affairs Office (PA) and is releasable to the National Technical Information Service (NTIS). At NTIS it will be releasable to the general public, including foreign nations.

RADC-TR-84-18 has been reviewed and is approved for publication.

APPROVED: Charles L Woods

CHARLES L. WOODS
Project Engineer

APPROVED: Harold Roth

HAROLD ROTH, Director
Solid State Sciences Division

FOR THE COMMANDER: John A. Ritz

JOHN A. RITZ
Acting Chief, Plans Office

If your address has changed or if you wish to be removed from the RADC mailing list, or if the addressee is no longer employed by your organization, please notify RADC (ESO) Hanscom AFB MA 01731. This will assist us in maintaining a current mailing list.

Do not return copies of this report unless contractual obligations or notices on a specific document requires that it be returned.

REPORT DOCUMENTATION PAGE

READ INSTRUCTIONS
BEFORE COMPLETING FORM

1. REPORT NUMBER RADC-TR-84-18	2. GOVT ACCESSION NO. AD-A141960	3. RECIPIENT'S CATALOG NUMBER
4. TITLE (and Subtitle) PHASE CONJUGATE OPTICS		5. TYPE OF REPORT & PERIOD COVERED Final Technical Report 1 Aug 80 - 31 Jan 83
		6. PERFORMING ORG. REPORT NUMBER N/A
7. AUTHOR(s) G. J. Dunning M. B. Klein R. C. Lind		8. CONTRACT OR GRANT NUMBER(s) F19628-80-C-0185
9. PERFORMING ORGANIZATION NAME AND ADDRESS Hughes Research Laboratories 3011 Malibu Canyon Road Malibu CA 90265		10. PROGRAM ELEMENT, PROJECT, TASK AREA & WORK UNIT NUMBERS 61102F 2306J236
11. CONTROLLING OFFICE NAME AND ADDRESS Rome Air Development Center (ESO) Hanscom AFB MA 01731		12. REPORT DATE February 1984
		13. NUMBER OF PAGES 234
14. MONITORING AGENCY NAME & ADDRESS(if different from Controlling Office) Same		15. SECURITY CLASS. (of this report) UNCLASSIFIED
		15a. DECLASSIFICATION DOWNGRADING SCHEDULE N/A

16. DISTRIBUTION STATEMENT (of this Report)

Approved for public release; distribution unlimited

17. DISTRIBUTION STATEMENT (of the abstract entered in Block 20, if different from Report)

Same

18. SUPPLEMENTARY NOTES

RADC Project Engineer: Charles L. Woods (ESO)

19. KEY WORDS (Continue on reverse side if necessary and identify by block number)

Phase Conjugation	Degenerate Four-Wave Mixing
Optical Data Processing	Photorefractive Materials

20. ABSTRACT (Continue on reverse side if necessary and identify by block number)

The purpose of this program has been the study, both theoretically and experimentally, of the use of phase conjugate optics for information processing and image transmission applications. A significant portion of effort was directed toward an improved understanding of the photorefractive effort and its application to two-wave and four-wave mixing. We have developed a model for grating formation in photorefractive materials and have derived expressions for figures of merit, which aid

in the selection of materials and the optimization of efficiency and speed. ~~We have~~ also developed a model for two-wave mixing in the transient regime, and have measured response times for both two-wave and four-wave mixing. Other devices and materials considered for ODP applications include the Hughes liquid crystal light valve and long-chain organic molecules.

Measurements on several ODP configurations were performed. First, we ~~have~~ used optical phase conjugation to transmit an image through a 1.75 m multimode fiber, with a resolution of better than 15 lines/mm. Secondly, ~~we~~ have demonstrated several static convolution and correlation operations, using character masks. Finally, ~~we~~ have investigated the use of phase conjugation for real-time optical correlation. Results of each of these experiments will be described.

Accession For
NTIS GRA&I ☒
DTIC TAB ☐
Unannounced ☐
Justification
By
Distribution/
Availability Codes

Dist	Avail and/or Special
A-1	

TABLE OF CONTENTS

SECTION PAGE

1 INTRODUCTION.................................. 7

2 MECHANISMS AND MATERIALS FOR PHASE CONJUGATION.................................. 11

A. Photorefractive Materials................. 13

B. Liquid Crystal Light Valve................ 35

C. Organic Materials......................... 39

3 IMAGE TRANSMISSION THROUGH FIBERS USING PHASE CONJUGATION............................ 49

A. Transmission of Images Through Fibers Using Phase Conjugation.................. 49

B. Phase Conjugation Using Optical Fibers as the Non-Linear Medium................. 57

4 TWO-WAVE MIXING............................... 61

5 OPTICAL CONVOLUTION AND CORRELATION............ 71

A. Static Two Dimensional Optical Convolution and Correlation............... 71

B. Real Time Correlation..................... 76

6 CONCLUSIONS AND RECOMMENDATIONS................ 91

REFERENCES..................................... 95

APPENDICES

A PRELIMINARY REPORT ON THE MATHEMATICS OF PHOTOREFRACTIVITY.............................. A-1

B SELECTION OF PHOTOREFRACTIVE MATERIALS FOR DEGENERATE FOUR WAVE MIXING.................. B-1

C OPTIMAL PROPERTIES OF PHOTOREFRACTIVE MATERIALS FOR OPTICAL DATA PROCESSING.......... C-1

D TWO-WAVE MIXING IN THE TRANSIENT REGIME........ D-1

E DEMONSTRATION OF IMAGE TRANSMISSION THROUGH FIBERS BY OPTICAL PHASE CONJUGATION.................................. E-1

LIST OF ILLUSTRATIONS

FIGURE PAGE

2-1 Typical geometry for hologram writing or DFWM in a nonlinear medium.......... 15

2-2 Geometry for hologram writing or DFWM in a uniaxial crystal such as $BaTiO_3$.......... 16

2-3 Experimental geometry. E_f, E_b and E_p are the forward pump, backward pump, and probe waves, respectivity.......... 24

2-4 Charge density for an incident probe pulse width of 30 τ_{di}.......... 25

2-5 Charge density for an incident pulse width of 9 τ_{di}.......... 26

2-6 Charge density for an incident probe pulse width of 1.5 τ_{di}.......... 27

2-7 Geometry for beam coupling experiments in $BaTiO_3$ at 4416Å.......... 29

2-8 Weak beam (probe) gain versus grating spacing for 3 $BaTiO_3$ samples.......... 30

2-9 Schematic of LCLV.......... 36

2-10 Configurations for microwatt phase conjugation using liquid crystal valve.......... 37

2-11 Measured MTF of liquid crystal light valve..... 40

2-12 Long conduction paths have large dipole moments. 42

2-13 Advantage of π bonds.......... 43

2-14 Free electron model: One-dimensions box with reflecting walls.......... 44

3-1 Demonstration of image transmission through a fiber.......... 50

3-2 Schematic of experiment used for image transmission through fibers.......... 52

3-3 Photograph of experimental apparatus used for image transmission through fibers.......... 53

PREVIOUS PAGE
IS BLANK

FIGURE PAGE

3-4 Reconstructed image after double passing the fiber.................................. 56

3-5 Schematic of degenerate four wave mixing experiments using silica fiber as nonlinear medium.................................. 58

4-1 Two-beam coupling experiment schematic........... 62

4-2 Single pulse data for two-beam coupling experiment incident probe pulse lower trace, amplified probe pulse upper trace................ 64

4-3 Repetitive waveform data for two-beam coupling experiment.................................. 67

4-4 Degenerate four wave mixing signal when probe is (i) A single pulse, (ii) a repetitive waveform, (iii) constant value........................... 68

5-1 Geometry used in two-dimension correlation experiment.................................. 72

5-2 Character mask used in 2-D correlation experiment.................................. 73

5-3 Normalized cross-correlation matrix.............. 75

5-4 Two-dimensional correlation experiment schematic.................................. 75

5-5 Relative indensity and frequency of diffracted orders produced by acousto-optic devices......... 77

5-6 Optical multiplication experiment schematic...... 79

5-7 Electronics used to drive acousto-optic devices block diagram.................................. 80

5-8 Fringe pattern created by pump beam and probe beam at position of conjugator.................. 82

5-9 Data for optical multiplication of the function, $F_1(t)$ and $F_2(t)$. A. $F_1(t) = 0.01$ Hz sawtooth, $F_2(t) = 0.9$ Hz square wave. B. $F_1(t) = 0.5$ Hz square wve, $F_2(t) = 0.05$ Hz sqare wave........... 83

5-10 Stability of various mounting techniques......... 85

5-11 Real time correlation experiment schematic....... 87

5-12 Real time auto correlation data................. 89

SECTION 1

INTRODUCTION

The purpose of this program has been the study, both theoretically and experimentally, of the use of phase conjugate optics for information processing and image transmission applications. The objectives are to analyze and develop phase conjugation techniques for optical signal processing, to determine the usefulness of phase conjugation for restoring spatial information transmitted over multimode optical fibers, and to study real-time optical convolution and correlation of two spatially or temporally modulated input waves. The contract was modified after its inception to include a task covering the theoretical and experimental study of materials for use in performing phase conjugation of spatially modulated optical waves.

The key theoretical and experimental results obtained under this program have been to:

- Develop a model of grating formation in photorefractive materials and derive expressions for figures of merit, which aid in the selection of materials and the optimization of efficiency and speed.
- Measure efficiency and response time for four-wave mixing and two-wave mixing in photorefractive materials.
- Demonstrate real-time holographic capabilities of the Hughes liquid crystal light valve.
- Analyze nonlinear optical behavior of long-chain organic molecules and estimate limiting values of the third order nonlinear susceptibility in the visible and microwave spectral regions.
- Demonstrate image transmission through a multimode fiber using optical phase conjugation.
- Perform two-dimensional optical correlation using phase conjugation.
- Investigate the application of phase conjugation to real-time optical information processing.

During the course of this program, we have studied three separate materials or devices for phase conjugation via degenerate four-wave mixing (DFWM). Photorefractive materials have the advantage of very large efficiences at cw power levels, and have moderate response times (10^{-3}-10^{-1} sec). We have developed a model for grating formation in photorefractive materials and have derived expressions for figures of merit for comparison and optimization of materials. At present, $BaTiO_3$ or SBN are preferred when high efficiency is required, while BSO is preferred when speed of response is most important. Our analysis suggest that significant improvements in the response times of $BaTiO_3$ and SBN can be obtained by improved control of the quantity and valence state of the dopants.

The second device of interest is the Hughes liquid crystal light valve, a high-sensitivity, high-gain device for large screen projection. We have demonstrated that the light valve can be considered as a real-time, thin holographic medium, and is capable of correcting for aberration in optical beams. We have shown how this device can be adapted for conventional four-wave mixing.

Finally, we have considered the possible use of long-chain organic molecules for DFWM. We have developed a simple model for calculating third-order nonlinear susceptibilities in these materials. The important result of this model is that the susceptibility scales as the third power of the length of this molecule, suggesting that giant values of susceptibility may be obtainable in sufficiently long molecules.

The transmission of spatial information through a multimode fiber is degraded for several reasons, two of which are modal dispersion and mode mixing. The process of phase conjugation — that is, passing a spatially modulated wave through a fiber, conjugating, and then retransmitting the beam back through the same fiber — can compensate for these effects and produce a restored image. We have used optical phase conjugation to transmit an image through a 1.75 meter multimode optical fiber with a resolution of better than 15 lines/mm.

The ability of one nonlinear technique, (DFWM), to perform the multiplication of two (or three) input signals in a nonlinear medium provides the capability of generating the optical convolution or correlation of spatially modulated waves. The use of a nonlinear optical process to generate the optical correlation/convolution is esentially a generalized Van der Lugt Holographic filter technique in which a nonlinear medium operating as a four-wave mixer replaces a conventional holographic film recording. The key advantage of such a system is that the "hologram" may be written and played back almost instantaneously (i.e., real-time signal processing can be performed). Because of this potential, we have investigated experimentally both spatial and temporal correlation geometries.

We have performed two dimensional correlation between a single character and matrix of characters using phase conjugation. The phase conjugator is placed at the common back focal plane of three lenses. The fields at this position are proportional to the Fourier transform of the front focal plane fields. A mask of characters is placed at the front focal plane of two of the lenses and the focal point of a fourth lens is positioned at the remaining front focal plane. The phase conjugate signal generated is proportional to the correlation of the illuminated characters.

In contrast to the static spatial masks used in the above experiments we also investigated the use of acousto-optic Bragg cells for imposing temporal information to be correlated. In this case, the signals, $f_1(t)$ and $f_2(t)$, to be correlated are encoded on the optical beam by two acousto-optic (A.O.) modulators. The first A.O. modulator is used to encode $f_1(t)$ as a temporal intensity variation. The second A.O. modulator is used as a delay line which produces a spatial variation proportional to $f_1(t) \cdot f_2(t-\tau)$. The modulated probe then propagates to the phase conjugator. The phase conjugate signal produced is proportional to the correlation of $f_1(t)$ and $f_2(t)$. In this manner we investigated the application of phase conjugation to real-time optical correlation.

MECHANISMS AND MATERIALS FOR PHASE CONJUGATION

A large number of nonlinear mechanisms have been proposed or demonstrated which have promise for phase conjugation of spatially-modulated optical signals via degenerate four-wave mixing (DFWM). We have performed a preliminary survey of these mechanisms, along with the performance of specific materials; the results are given in Table 1. Several of the tabulated materials have the desirable properties of requiring modest (cw) pump power levels and having response times in the millisecond or sub-millisecond region. It is expected that most of the materials should operate at spatial frequenices approaching 1000 lines/mm (1 μm resolution in the material), and thus be suitable for handling high spatial bandwidth signals

Among the mechanisms and materials listed in Table 1, we have chosen three for further study: photorefractive materials, the liquid crystal light valve and long-chain organic polymers. Photorefractive materials operate over a relatively wide wavelength range at modest cw power levels, and have response times in the 10^{-3}-10^{-1} sec range. Photorefractive materials with high promise include $BaTiO_3$ and SBN (with demonstrated high DFWM reflectivity), $KNbO_3$ (moderate reflectivity with fast response), and BSO (lower reflectivity with very fast response). Some characteristics of $BaTiO_3$, $KNbO_3$ and BSO are included in Table 1.

Although BSO is an electro-optic crystal[15] with optical activity[16], it has been used to demonstrate high sensitivity holographic storage[17], joint transform processing[13], and incoherent optical conversion[18].

The liquid crystal light valve is a state-of-the-art device developed at Hughes Research Laboratories for large screen projection at TV scan rates. It is basically an optical-to-optical image transducer that has high input sensitivity (~50 μW/cm^2) and high gain, allowing projection with intense light sources. Although the LCLV was developed for real-time imaging applications, it is readily adaptable for real-time holography and the optical data processing functions derived from its holographic properties.

PREVIOUS PAGE
IS BLANK

Table 1. Mechanisms and Materials for Phase Conjugation of Spatially Modulated Signals via Degenerate Four Wave Mixing

[illegible]	Typical Material	Wavelength, [illegible]	Typical Operating Power Level W/cm^2	Response Time	Typical DFWM Reflectivity	Comments
[illegible]	BaTiO$_3$	0.35-1.6	1	10-100 msec	[illegible]	High quality samples
[illegible]	KNbO$_3$	0.41-0.65	1	1-10 msec	[illegible]	hard to obtain
	[illegible]	[illegible]	1	1 msec	[illegible]	Optically active
[illegible]	[illegible]	[illegible]	10^6 (pulsed)	10 nsec	[illegible]	High power required
	[illegible]	[illegible]	50	10 nsec	[illegible]	narrow band
	[illegible]	[illegible]	100	4 msec	[illegible]	
	[illegible]	0.48-0.54	1	4 msec	[illegible]	
[illegible]	[illegible]	0.53	10^9 (pulsed)	1 sec	[illegible]	High power required
[illegible]	[illegible]	1.06	10^6	1 sec	[illegible]	High power required
[illegible]	Liquid solvent with dissolved dye	0.4-1.[illegible]		10 [illegible]		Prefers pulsed operation
	Liquid crystal near phase transition	[illegible]	0.1	100 msec		[illegible]
[illegible] orientation in liquid crystal near phase transition	MBBA	0.4-1.2	1	1 sec	[illegible]	[illegible]
[illegible] in [illegible] crystal [illegible]	MBBA	0.4-1.[illegible]	5 x 10^{-5}	[illegible]	[illegible]	[illegible]
[illegible]	Latex spheres in water	0.4-1.5	5 x 10^3	140 [illegible]	[illegible]	High power required
[illegible]	Epoxy resin with dissolved dye	0.4-1.5	0.4	10 msec	[illegible]	[illegible]
[illegible] nonlinearity [illegible] materials ([illegible] polymers)	[illegible]	0.5-2.0	10^6	1 [illegible]	[illegible]	[illegible] with [illegible]

Organic molecules in the form of long-chain polymers with conjugated bonds are very promising nonlinear materials because of the large induced dipole which results from the long length of the molecule. Experiments performed to date show the expected scaling of the nonlinear coefficient with chain length. The analysis described below allows the estimation of the required length to yield values of $\chi^{(3)}$ on the order of 10^{-2} esu. Such a nonlinearity would allow high efficiency DFWM with low-power cw lasers.

In this section we describe the results of analysis and experiments on photorefractive materials, allowing the design and selection of materials for a given application. We next describe measurements intended to characterize the real-time holographic properties of the liquid crystal light valve. Finally, we describe our analysis of the nonlinear optical behavior of long-chain polymers, leading to the estimation of the requirements for third-order susceptibilities on the order of 10^{-2} esu.

A. PHOTOREFRACTIVE MATERIALS

1. Analysis

Photorefractive materials are the most promising candidate materials for optical data processing at the present time. In this program we have carefully analyzed and expanded upon existing models for grating formation in photorefractive materials, and we have established figures of merit for selecting an optimum material for a given experiment.

The major part of our analysis of photorefractive materials is summarized in Appendices A, B and C. Appendix A is a report by Marshall Sparks which details the physical assumptions used in this and subsequent analytical work and derives expressions for the steady state space charge electric field in a number of operating regimes. The time response of the space charge field was also calculated for certain limiting assumptions.

Appendix B is a manuscript which was prepared for the SPIE San Diego Meeting in August, 1982. It reviews the analysis of grating formation and presents exact expressions for the time constants in the limit of small modulation depth. Several performance parameters were also discussed, and the application to materials selection was considered.

Appendix C is a preprint of a draft manuscript to be submitted to a special issue of Optical Engineering on Optical Data Processing. In this manuscript the analysis of grating formation is again reviewed. Various material figures of merit are then considered in detail, and these parameters are evaluated for $BaTiO_3$ and BSO in order to compare their performance in a number of applications.

The simple holographic picture of grating formation and DFWM is outlined in Figure 2-1. In this scheme a holographic grating is written by the beams, E_1 and E_2. A third beam, E_3, scatters from this grating and creates the signal beam, E_4, which propagates in the backward E_2 direction. The nonlinear reflectivity is defined as $R = |E_4/E_2|^2$.

It is also important to keep in mind that the nonlinear crystals used for photorefractive applications are highly anisotropic. In particular, the effective electro-optical coefficient depends strongly on the polarization of the beams and on the angle, θ. between the c-axis and the grating wave vector (see Figure 2-2). For extraordinary polarized beams in $BaTiO_3$, the effective electro-optic coefficient for $\theta=0$ is r_{33}. However, for $\theta>0$ there is an added contribution from r_{42}. Since r_{42} is much larger than r_{33} (see Table 3), the grating efficiency or DFWM reflectivity increases rapidly with θ up to value of ~40°. Because of the large refractive indices of $BaTiO_3$, this optimum angle cannot be obtained unless the crystal is immersed in index matching fluid. In all our experiments with $BaTiO_3$ the crystal is in air and the maximum value of θ is ~20°. Even at this value of θ, two-wave mixing gains on the order of 20, and four-wave mixing reflectivities on the order of 200-400%, can easily be observed.

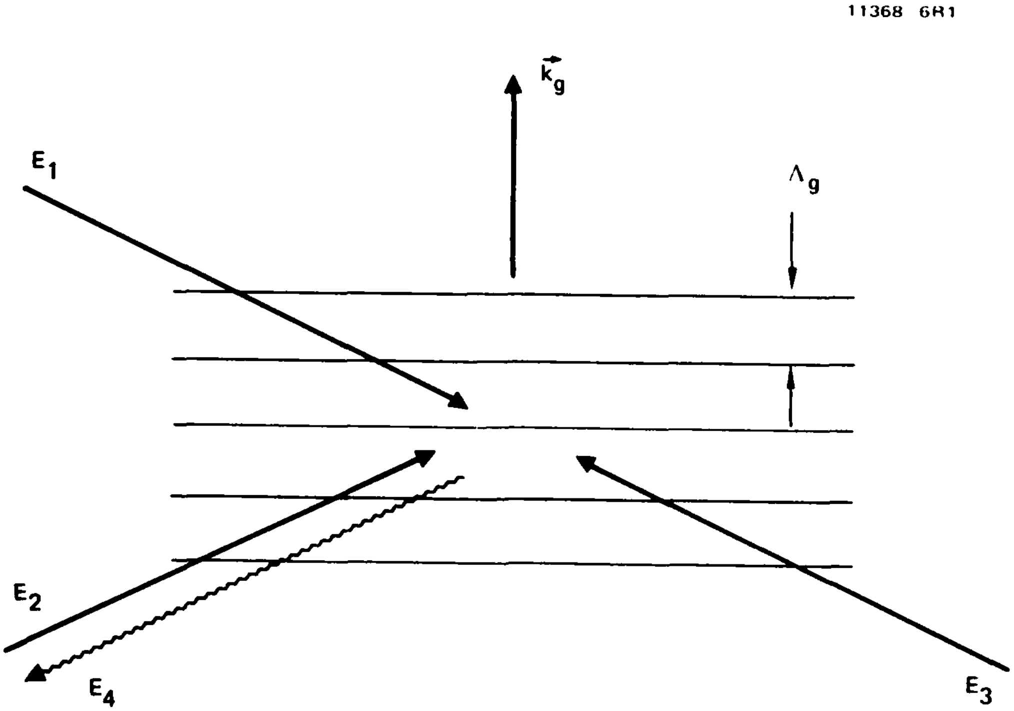

Figure 2-1. Typical geometry for hologram writing or DFWM in a nonlinear medium. In holographic language, E_1 is the reference writing beam, E_2 is the image writing beam, E_3 is the radout beam, and E_4 is the signal beam. In the language of DFWM, E_1 and E_3 are the pump beams, E_2 is the probe beam, and E_4 is the signal beam. The parameter Λ_g is the grating spacing.

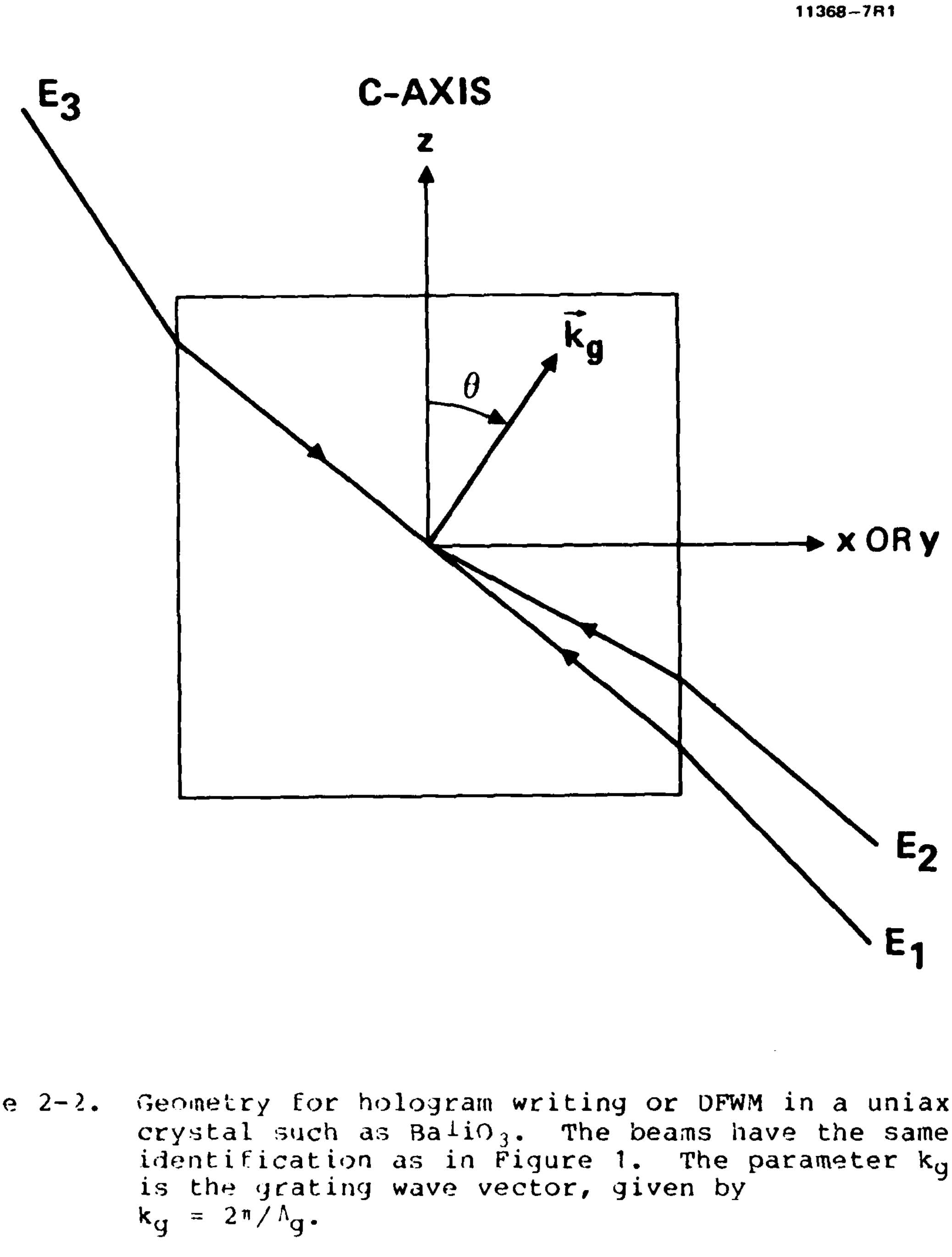
11368-7R1
C-AXIS
z
E3
$\vec{k}_g$
θ
x OR y
E2
E1

Figure 2-2. Geometry for hologram writing or DFWM in a uniaxial crystal such as $BaTiO_3$. The beams have the same identification as in Figure 1. The parameter k_g is the grating wave vector, given by $k_g = 2\pi/\Lambda_g$.

Two separate models for describing charge transport in photorefractive materials have been formulated. The hopping model[1] assumes that carrier transport occurs via hopping from a filled donor site to a neighboring empty trap. This model was originally developed to describe electrical conduction in semi-insulating materials and amorphous semiconductors. The band transport model[2,3,14] assumes that electrons (or holes) are optically excited from filled donor (or acceptor) sites to the conduction (or valence) band where they migrate to dark regions in the crystal by drift or diffusion before recombining into an empty trap. In both models the transported charges result in an ionic space charge grating which is, in general, out of phase with the incident irradiance. The space charge grating is balanced by a periodic space charge electric field in accordance with Poisson's equation. This space charge field modulates the refractive index through the electro-optic effect. The band transport model has been developed to a greater degree and is in wider use in the literature; this is the model which we have used in our analysis.

In order to analyze the DFWM properties of ferroelectrics, we first require expressions for the amplitude and spatial phase of the space charge electric field. In the Appendices the required expressions have been derived (using the band transport model) for specific limiting cases. One case of relevance for many experiments is $m \ll 1$, where m is the fractional modulation of the input irradiance. For this case[2,3,14] the solution for the steady state space charge field amplitude is

$$E_{sc} = m\,E_q \,{\frac{(E_o^2+E_D^2)}{E_o^2 + (E_D+E_q)^2}}^{1/2} \qquad (1)$$

where

E_o = Applied drift field (normal to grating planes),

$E_D = \frac{kT}{e} k_g$ (diffusion field).

and

$E_q = \frac{4\pi e N_A}{\epsilon k_g}$ (limiting spacecharge field).

In the above expressions, k is the Boltzman constant, k_g is the grating wave number, N_A is the density of empty traps, and ϵ is the dielectric constant. The field E_q is that which results from the separation of all available charges by one grating period. The spatial phase, ψ of E_{sc} (relative to the irradiance), is given by

$$\tan \psi = \frac{E_D}{E_o} \left[1 + \frac{E_D}{E_o} + \frac{{E_o}^2}{E_D E_q} \right] . \tag{2}$$

The general, $E_D << E_q$, so that with no applied drift field $E_{sc} \approx m E_D$, and $\psi = \pi/2$. This is the diffusion limit, for which a characteristic spatial phase shift between the irradiance and the space charge field is observed. As the applied drift field is increased from zero, we have $E_{sc} \approx m ({E_o}^2 + {E_D}^2)^{1/2}$, and the spatial phase is intermediate between 0 and $\pi/2$. Finally, for large values of drift field ($E_o > E_q$), the space charge field saturates at $E_{sc} \approx m E_q$, and the phase shift, ψ, is once again $\pi/2$.

Note that for small values of the drift field ($E_o < E_q$), the space charge field is independent of all material parameters. In this case the induced refractive index variation is determined entirely by the relevent electro-optic coefficient. Thus, for large values of index modulation, materials with large values of electro-optic coefficient are desirable. However, materials in this category (e.g., $BaTiO_3$, SBN) tend to be slow. Specifically, the band transport solutions for small modulation fraction give the write or erase time[3] as

$$\tau_e = \tau_w = \tau_{di} \; f(k_g, E_o) \quad , \qquad (3)$$

where τ_{di} is the dielectric relaxation time,

$$\tau_{di} = \frac{\varepsilon}{4\pi\sigma} = \frac{\varepsilon}{4\pi n e \mu} \quad , \qquad (4)$$

where σ is the conductivity, n is the free carrier density, and μ is the mobility. The function, $f(k_g, E_o)$, accounts for the spatial variation of the free carrier density (see Appendices B and C). In many cases of physical interest, $f(k_g, E_o) \approx 1$ and $\tau_e = \tau_w = \tau_{di}$.

If the conductivity, σ, is dominated by the contribution from photocarriers, then a simple rate equation solution gives

$$n = \frac{sI_o}{\gamma_R} \frac{N_D - N_A}{N_A} \quad , \qquad (5)$$

where s is the photoionization cross section, γ_R is the recombination rate coefficient, $N_D - N_A$ is the density of filled traps, N_A (as defined earlier) is the density of empty traps, and I_o is the average irradiance. By combining Equations (4) and (5), we obtain

$$\tau_{di} = \frac{\varepsilon \gamma_R}{4\pi e \mu s} \frac{1}{I_o} \frac{1}{R} \quad , \qquad (6)$$

where the reduction ratio R is defined as

$$R = \frac{N_D - N_A}{N_A} \quad . \qquad (7)$$

The quantity in parentheses in Equation (6) can be considered as a material figure of merit, having units of energy/unit area. Once a material is chosen, only limited experimental control over this quantity is possible (see Appendix C). However, the quantity R can be varied over many orders of magnitude by reduction or oxidation of a given sample. It is clear from Equation (6) that increasing R through chemical reduction can significantly reduce τ_{di}. Values of R as high as 10 are not hard to achieve in many cases, and in some materials (e.g., BSO) values of R on the order of 10^3 are typical.[4] Note, however, that large increases in R, if accompanied by a reduction in N_A, can reduce the limiting grating efficiency by reducing E_q (see Appendix C). Note also the I_o^{-1} dependence in Equation (6), indicating the direct relation between speed and irradiance.

In this review of grating formation in photorefractive materials, it was assumed that the incident fields in each volume element are known. In an actual beam coupling or DFWM experiment, only the incident optical fields on the sample boundaries are known. The complete grating solution requires the substitution of the refractive index change (as a function of the local optical fields) into the wave equations which describe the variation of the optical fields with position in the material. This results in four coupled-wave equations for DFWM, and two equations for the simpler case of beam coupling (or two-wave mixing). In these equations, the contribution from both the small-period and large-period gratings must be considered, as well as self-interaction effects. Several approaches to the solution of the coupled-wave equations have been presented.[5-7] In the limit of low pump depletion and small beam coupling, the coupled wave approach is not necessary, and the volume grating solutions are adequate for analysis. Even when large beam coupling is present, the volume grating solutions for the write and erase times are still correct.

On the basis of the above analysis, we may define four performance parameters (or figures of merit) which characterize a given material for a particular application. These parameters (described in detail in Appendix C) are: steady state index change

(Δn_{ss}), response time ($\tau_w=\tau_e$), write energy (w), and photorefractive sensitivity (S=dn/dw). The relevance of each parameter will vary with the application. For example, when high diffraction efficiency or four-wave mixing reflectivity is required, the steady-state index change will be the most important parameter. If high speed operation is desirable, then the response time will be most important. If limited optical energy is available, then the write energy will be most relevant. And finally, if sensitivity to small changes is critical, then the sensitivity will be most relevant.

In Table 2 we have listed performance parameters for $BaTiO_3$ and BSO for two values of grating spacing and applied drift field. The relative advantages of these two materials is discussed in Appendix C. Essentially, the large electro-optic coefficient of $BaTiO_3$ makes this material preferred when high efficiency is required. On the other hand, BSO is preferred where fast response time or low writing energy is required. Note that neither material has been optimized for photorefractive applications. In particular, it is expected that control of the dopant species, valence state and concentration in $BaTiO_3$ should reduce the response time by a significant amount.

The volume grating solutions summarized above provide the steady state and step function response for the charge density and space charge field, but are not directly applicable for pulsed excitation. In Appendix D we present a model for grating formation with pulsed excitation. This model (summarized below) also applies to two-wave mixing and four-wave mixing for the case of nondepleted, strong pumps and a weak probe wave. This work was supported by Hughes IR&D funds and the purpose of including this model is to allow comparision with the pulsed-probe two-wave mixing studies described in Section 5.

Our model relies on the following asumptions:

- The pumps are cw.
- The incident probe is a pulse of duration, t_p, and magnitude, $\mathcal{E}_p$.

Table 2. Figures of Merit for BSO and $BaTiO_3$

MATERIAL	GRATING SPACING Λ_g (μm)	ELECTRIC FIELD E_o (KV/cm)	STEADY STATE INDEX CHANGE Δn_{ss}	RESPONSE TIME τ_e FOR 1 W/cm^2 (mSEC)	WRITING ENERGY W (mJ/cm^2)	SENSITIVITY S (cm^3/KJ)
BSO	1	0	5×10^{-6}	0.6	1.8	4.5
	1	10	17×10^{-6}	2.3	1.8	4.5
	10	0	1×10^{-6}	0.1	1.2	6.5
	10	10	38×10^{-6}	2.5	0.5	15
$BaTiO_3$	1	0	150×10^{-6}	350	30	1.5
	1	10	270×10^{-6}	200	9	4.2
	10	0	40×10^{-6}	900	210	0.1
	10	10	1700×10^{-6}	800	6	6

- The interaction geometry is as shown in Figure 2-3.

  For DFWM, all three input waves are present. For two-wave missing, we shall set $\mathcal{E}_b=0$.

- The pump waves are nondepleted during the nonlinear interaction.

Using the charge transport model of Kukhtarev[2,3] and Laplace transform techniques, we have obtained solutions for this charge density and the space charge electric field. We then calculated the two-wave response of $BaTiO_3$ to a square-wave probe pulse, with three possible time durations. The assumed conditions are:

Dielectric Relaxation Rate: $3.0\ \text{sec}^{-1}$

Diffusion Rate: $1.0\times10^{4}\ \text{sec}^{-1}$

Photoionization Rate: $1.0\times10^{4}\ \text{sec}^{-1}$

Electron Recombination Rate: $1.0\times10^{9}\ \text{sec}^{-1}$

Ion Recombination Rate: $1.0\times10^{2}\ \text{sec}^{-1}$

In Figure 2-4 we have plotted the charge density versus time for a pulse width of 30 τ_{di}. Because of the long pulse width, the material is in the steady state during most of the pulse duration. In Figure 2-5 the pulse width is only 10 τ_{di} and the material is only briefly in the steady state. For a sufficiently short pulse (Figure 2-6) the system does not reach steady state and the peak signal is reduced. The results of section 5 clearly follow the behavior plotted in Figures 2-4-2-6.

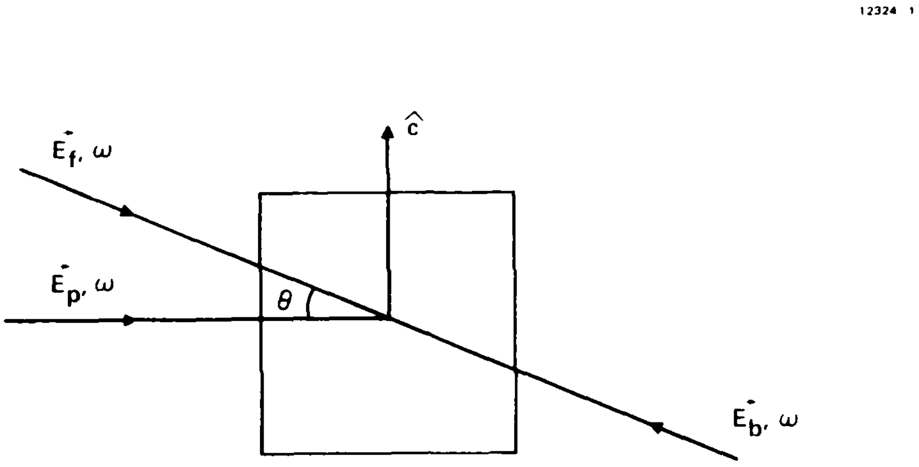
12324 1
$\hat{c}$
$\vec{E}_f, \omega$
$\vec{E}_p, \omega$
θ
$\vec{E}_b, \omega$

Figure 2-3. Experimental geometry. E_f, E_b and E_p are the forward pump, backward pump, and probe waves, respectively.

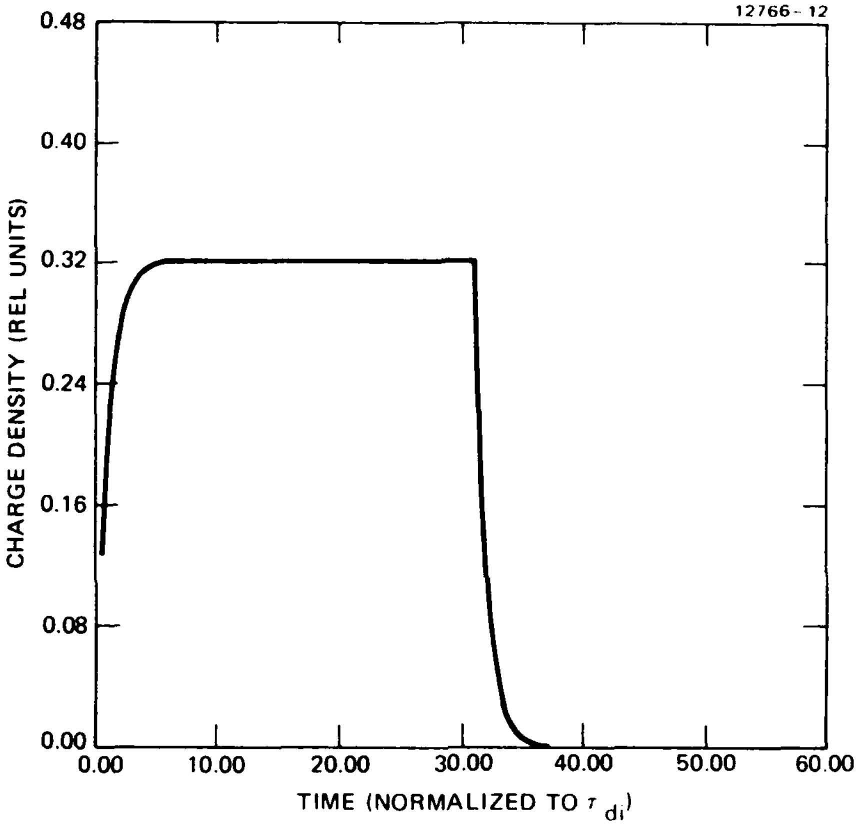

Figure 2-4. Charge density for an incident probe pulse width of 30 τ_{di}.

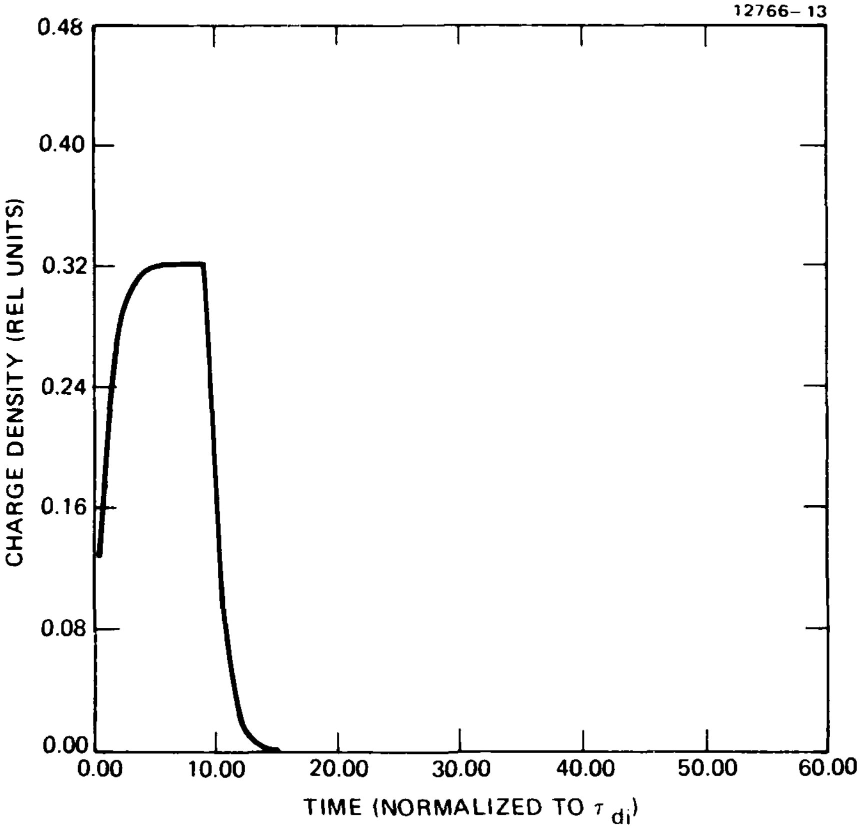

Figure 2-5. Charge density for an incident pulse width of 9 τ_{di}.

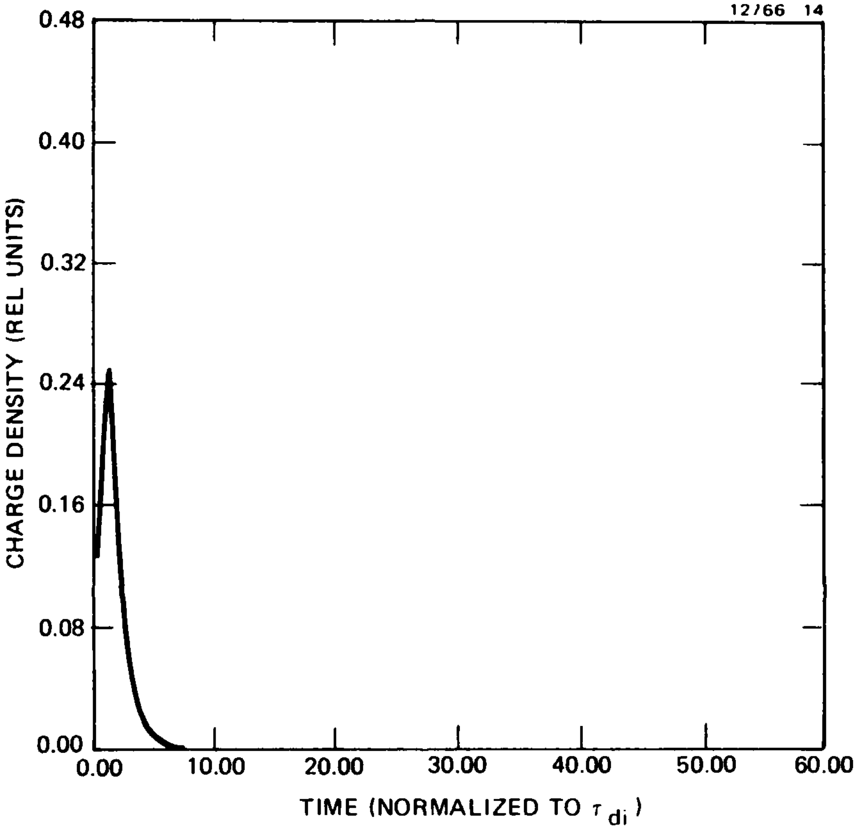

Figure 2-6. Charge density for an incident probe pulse width of 1.5 τ_{di}.

2. Experiments

In the experimental phase of our materials study, we have measured the photorefractive properties of a number of materials via two-wave mixing (beam coupling) and four-wave mixing. We have also developed a technique for poling the $BaTiO_3$ crystals required for our experiments.

In our beam coupling experiments, we have measured the steady-state weak-beam gain at 4416Å as a function of grating spacing for several $BaTiO_3$ samples. The geometry for our experiment is shown in Figure 2-7. Both input beams were derived from a Liconix He-Cd laser; the pump power was 25 mW and the probe power was 3 mW. The beams were unfocused and the spot diameter at the crystal was ~2 mm. The crystal was oriented so that the grating wave vector, k_g, was aligned parallel to the crystal c-axis. For p-polarized input beams (extraordinary polarization inside the crystal) the induced refractive index change depends in a complicated manner on the electro-optic coefficients, r_{13} and r_{33}. Furthermore, extraordinarily polarized beams are subject to beam fanning,[8] which creates significant beam distortion. We have thus chosen to use beams with ordinary polarization in the crystal; the appropriate electro-optic coefficient is thus r_{13}. For this orientation the beam coupling is relatively small (since $r_{13}<r_{33}$), so that the effects of pump depletion are not significant.

In Figure 2-8 we plot the weak beam gain, G (output intensity divided by input intensity), as a function of grating spacing, Λ_g, for three $BaTiO_3$ samples (all purchased from Sanders Associates). the gain can be written as

$$G = e^{\gamma L} \tag{8}$$

where γ is the gain coefficient and L is the interaction length. Kukhtarev[9] has shown that the gain coefficient, γ, is proportional to the space charge field, E_{sc}. Thus, from Equation (1)

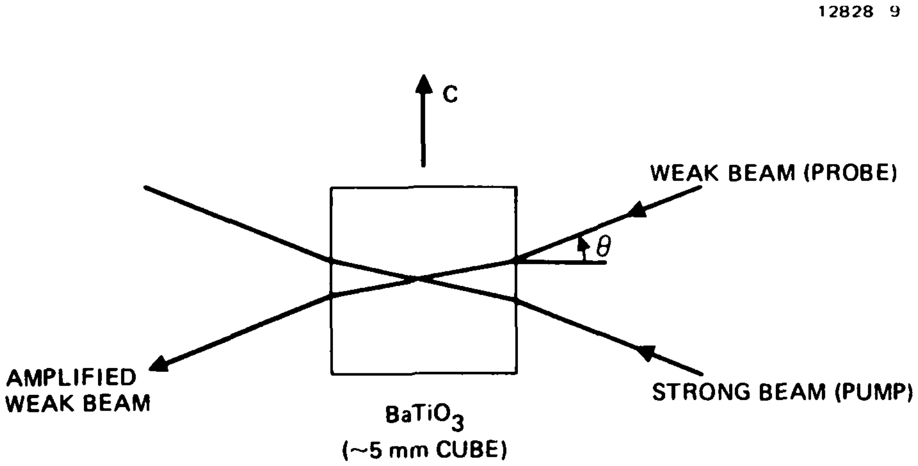
12828 9
C
WEAK BEAM (PROBE)
θ
AMPLIFIED
WEAK BEAM
STRONG BEAM (PUMP)
$BaTiO_3$
(~5 mm CUBE)

Figure 2-7. Geometry for beam coupling experiments in $BaTiO_3$ at 4416Å.

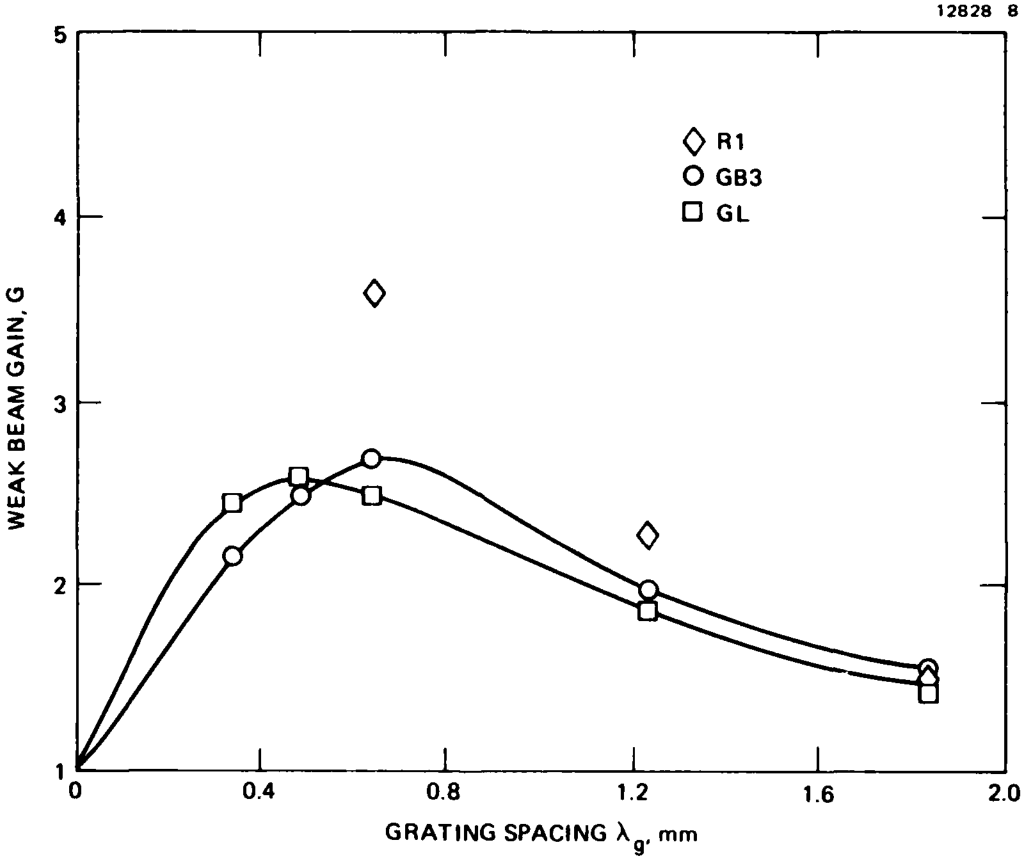

Figure 2-8. Weak beam (probe) gain versus grating spacing for 3 $BaTiO_3$ samples.

$$\gamma \sim E_{sc} \sim \frac{E_q E_d}{E_q + E_d} , \qquad (9)$$

since $E_o=0$.

By substituting the definitions for E_d and E_q, we find that

$$\gamma \sim \frac{\frac{4\pi kT}{\epsilon} N_A}{\frac{kT}{e}\frac{2\pi}{\Lambda_g} + \frac{2eN_A}{\epsilon}\Lambda_g} . \qquad (10)$$

Thus, for small values of Λ_g, $\gamma \sim E_q \sim \Lambda_g$. For large values of Λ_g, $\gamma \sim E_d \sim \Lambda_g^{-1}$. The peak value of γ(or G) as a function of Λ_g occurs for $E_d=E_q$ or $\Lambda_{g_o}^2 = \pi \epsilon kT/e^2 N_A$. Thus, measurement of Λ_{g_o} allows the determination of N_A.

The data of Figure 2-8 are consistent with the above model. For large Λ_g, the gain for all crystals approaches the same value (E_d is independent of N_A). For small Λ_g, the curves rise with different slopes and peak at different values of Λ_g, consistent with different values of N_A. For crystal GB3 we find $N_A = 2x10^{16}/cm^3$, while $N_A = 4x10^{16}/cm^3$ in crystal GL. The value for GB3 is close to that measured in a separate sample[1] by a similar technique. This consistency lends support to the numerical value $N_A = 2x10^{16}/cm^3$, which was chosen for the figure of merit calculations in Appendix C.

In a separate set of experiments, we have measured the reflectivity and response time for DFWM in four different crystals at 6471Å. In our experiments the two counterpropagating pump beams both had incident intensities of ~10 mW/cm^2, while the probe intensity was ~1 mW/cm^2. The angle between the probe and forward pump was 40°, corresponding to a grating spacing of 1.1 μm. The results of our experiments are summarized in Table 3. For each material the laser polarization and crystal orientation were adjusted to exploit a particular component of the electro-optic

Table 3. DFWM Reflectivity and Response Time at 6471 Å

MATERIAL	DOMINANT ELECTRO-OPTICAL COEFFICIENT		DFWM REFLECTIVITY	RESPONSE TIME (SECONDS)
	COMPONENT	VALUE * (10^{-10} cm/V)		
$Bi_{12}GeO_{20}$ (BGO)	r_{41}	5	.02%	.01
$BaNaNb_5O_{15}$(BNN)	r_{33}	48	1%	20
$BaTiO_3$	r_{42}	1640	>100%	4
$LiNbO_3$	r_{33}	32	.5%	50

*Unclamped (low frequency) value.

coefficient. Note that the DFWM reflectivity varies monotonically with the value of the electro-optic coefficient, as expected if the charge transport is dominated by diffusion. The material with the shortest response time is BGO, which is consistent with the large values of reduction ratio expected in this material. The particularly slow response times in BNN and $LiNbO_3$ suggest that the reduction ratios are much lower in these materials.

To conclude this section, we will describe our experiments on the poling of $BaTiO_3$. An as-grown crystal of $BaTiO_3$ consists of small spontaneously polarized regions called domains. These domains can be polarized in one of 6 possible directions: along one of the three cubic axes and with positive or negative polarity. The domains generally arrange themselves so that the net macroscopic polarization is zero in any direction. The possible number of polarization directions can be reduced to two by pressing the crystal on 2 pairs of cubic faces. This is known as mechanical poling, and it leaves the crystal with only one axis of polarization, but with both possible senses along this axis. The remaining domains (called 180° domains) must be removed electrically; i.e., an applied electric field will cause the parallel-polarized domains to grow and the antiparallel-polarized domains to shrink and disappear. As-purchased crystals from Sanders Associates have been mechanically poled by the supplier; thus, the required task is electrical poling.

There are two well-known problems associated with the electrical poling of $BaTiO_3$: (1) the crystals are very susceptible to fracture if they are heated or cooled through the Curie transition; (2) the crystal face in contact with the positive poling electrode suffers severe localized fractures, the extent of which are proportional to the temperature of the crystal and the amount of time the poling voltage is applied. To circumvent these problems, we only heat the crystal to ~5° below the Curie temperature, and we start cooling the crystal as soon as the poling field (5-10 kV/cm) is applied. We use silver paint as electrodes, and we immerse the crystal in a heated beaker of high viscosity dielectric oil in order to provide a stable temperature environment. A complete heating/cooling cycle requires approximately 3 hours.

After the completion of a poling run, it is important that an accurate system for measuring the degree of poling be available. We use two techniques for measuring the degree of poling. The preferred technique is the measurement of the electro-optic coefficient, $r_c=r_{33}-(n_o/n_e)^3r_{13}$. This coefficient is most easily measured by applying a modulating field along the c-axis and measuring the amplitude modulation induced on a beam propagating at 90° to the c-axis, and polarized at 45° to the c-axis. In an unpoled crystal the induced retardation from domains polarized along +C approximately cancels the retardation from domains polarized along -C, and very small amplitude modulation is observed. When the crystal is 100% poled, the amplitude modulation is large and the measured value of r_c is at a maximum. We have poled two crystals since the poling technique described above was developed. In each case the measured value of r_c before poling was approximately 100 times smaller than the literature value. After electrical poling, the measured coefficient was a factor of 2.4 smaller than the literature value for both crystals. It is, of course, possible that both crystals are only ~40% poled. However, the similarity in the two measured values suggests that the literature value may be in error.

A second technique for measuring degree of poling is to measure the weak beam gain in a beam coupling experiment. This should be done for values of $\Lambda_g > 2$ μm, in order to eliminate the contribution of N_A to the results (i.e., the diffusion limit is preferred). The weak-beam gain coefficient is proportional to the degree of poling. This technique has the advantage of not requiring an electroded crystal; the major disadvantage is that the experimental arrangement is more complicated.

B. LIQUID CRYSTAL LIGHT VALVE

As mentioned earlier, the liquid crystal light valve (LCLV) is an optical-to-optical image transducer which has high input sensitivity (~50 μW/cm^2) and high gain, allowing projection with intense light sources. As shown in Figure 2-9, the device consists of a sandwich of thin-films that electrically control the optical birefringence of a thin liquid crystal layer. With no writing illumination ("off" state) the applied voltage does not appear across the liquid crystal layer because the resistivity of the silicon photoconductive layer is high. Polarizers are arranged in the projection beam so that with no writing illumination there is no output signal (dark output). When a spatially varying writing beam illuminates the silicon photoconductive layer, the resistivity of this layer is reduced in the illuminated regions, and part of the applied voltage appears across the liquid crystal in proportion to the strength of the illumination. This applied voltage alters the birefringences of the liquid crystal layer, and thus a transmitted signal appears in projection. One important feature of the LCLV is that the dielectric mirror and light blocking layer provide high optical isolation between input and output, thereby allowing large optical gain. The performance characteristics of the LCLV are summarized below:

- Resolution: 70 lines/mm (35 cycles/mm)
- Sensitivity: 20 μW/cm^2
- Rise/decay times: 5 mS (liquid crystal limited)
- Wavelength range: 400-1100 nm
- Aperture: 2 inches diameter.

The important advantages of the LCLV for phase conjugation are the low operating power levels and the relatively fast response time. Two schemes for utilizing the light valve for phase conjugation are shown in Figure 2-10. In its standard configuration, the light valve is analogous to a conventional

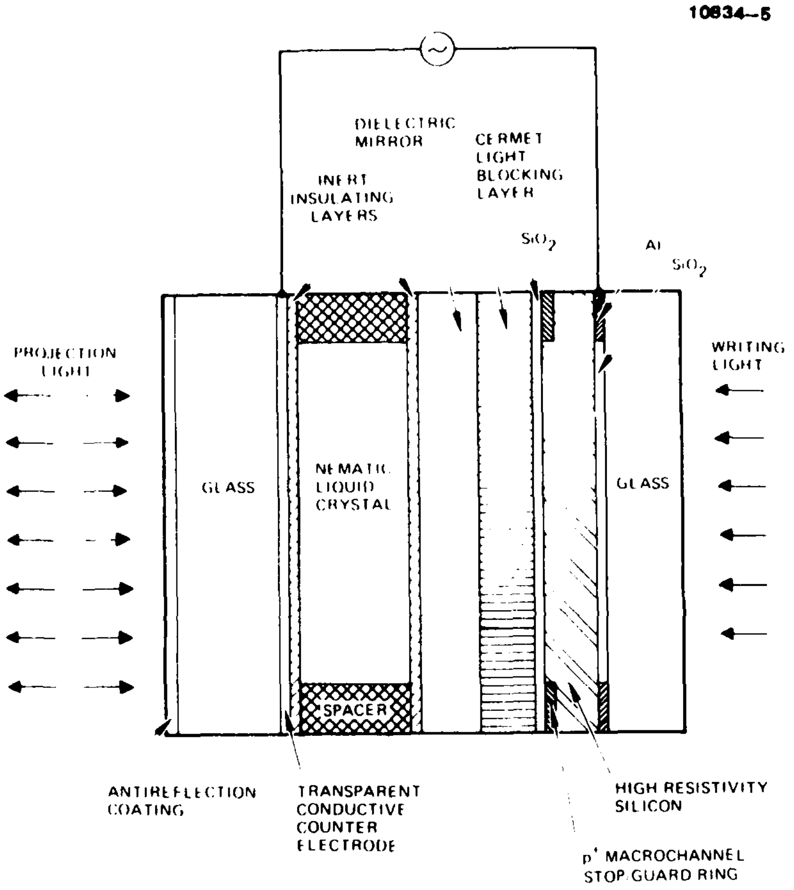
10834-5
DIELECTRIC MIRROR
CERMET LIGHT BLOCKING LAYER
INERT INSULATING LAYERS
SiO$_2$
Al
SiO$_2$
PROJECTION LIGHT
WRITING LIGHT
GLASS
NEMATIC LIQUID CRYSTAL
GLASS
SPACER
ANTIREFLECTION COATING
TRANSPARENT CONDUCTIVE COUNTER ELECTRODE
HIGH RESISTIVITY SILICON
p$^+$ MACROCHANNEL STOP GUARD RING

Figure 2-9. Schematic of LCLV.

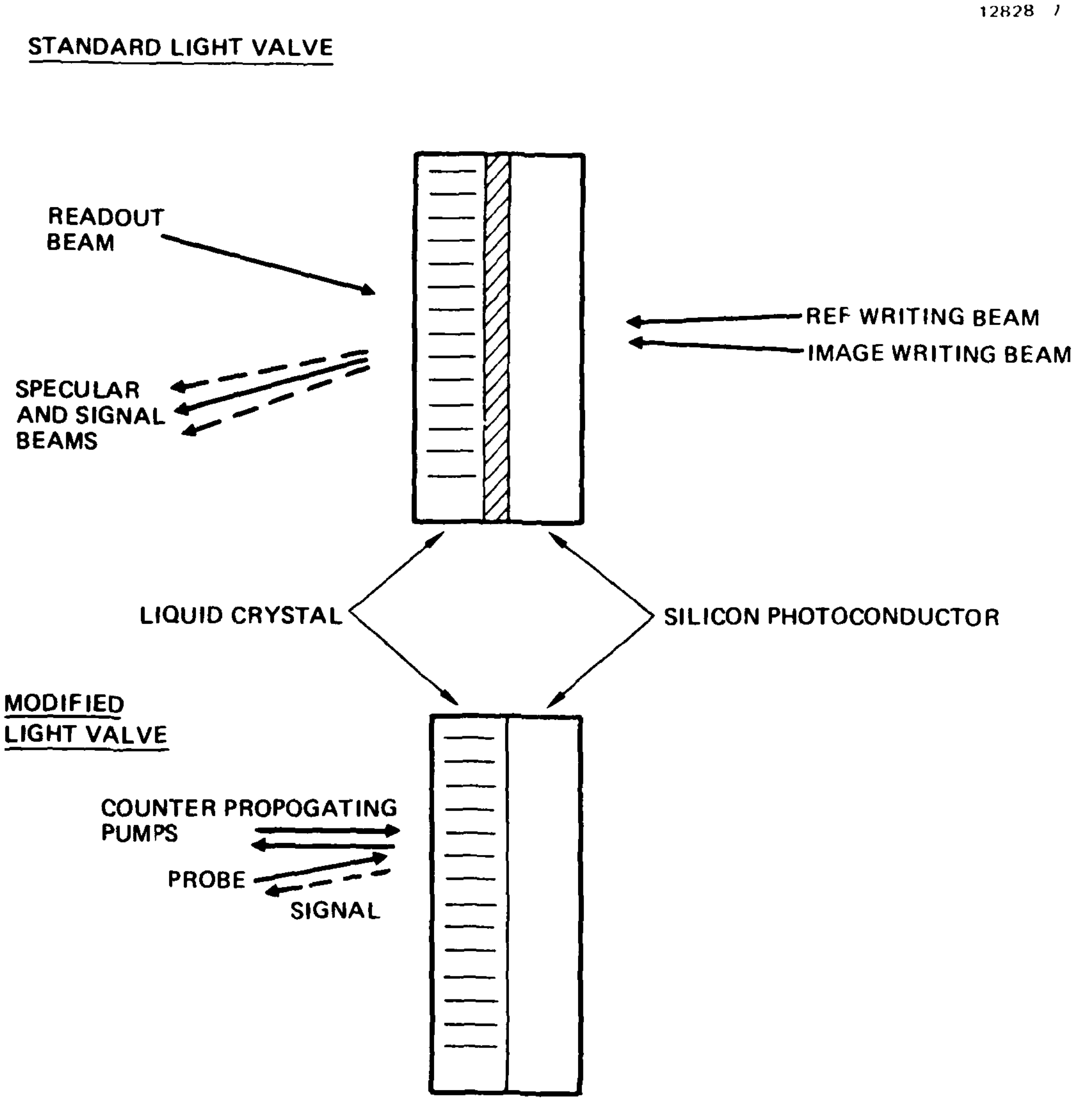

12828 7
STANDARD LIGHT VALVE
READOUT BEAM
SPECULAR AND SIGNAL BEAMS
REF WRITING BEAM
IMAGE WRITING BEAM
LIQUID CRYSTAL
SILICON PHOTOCONDUCTOR
MODIFIED LIGHT VALVE
COUNTER PROPOGATING PUMPS
PROBE
SIGNAL

Figure 2-10. Configurations for microwatt phase conjugation using liquid crystal valve.

holographic medium. The two write beams produce a grating pattern in the photoconductor which is transferred to a thin phase grating in the liquid crystal, which is read out on the output side. The advantage of this scheme is the large optical gain; however, the scheme is awkward for aberration compensation. On the other hand, by removal of the blocking layer and dielectric coating all beams can be brought in from the output side of the device, resulting in a more conventional four-wave mixing geometry. The only disadvantage is that no optical gain is present; all beams must have intensities in the 50 $\mu W/cm^2$ range. The phase conjugation mechanism in this configuration is as follows: The reference (pump) and image (probe) beams interfere in the photoconductive layer, producing a spatial variation in conductivity. This spatial pattern is then transferred to the liquid crystal as a spatial pattern in the refractive index, which is then read out by the reflected pump beam, producing a signal (phase conjugate) beam in the retro probe direction. The major advantages of such a device are its high sensitivity (20 $\mu W/cm^2$) and broad wavelength coverage. Because of the thin-film nature of the liquid crystal layer, the DFWM reflectivity is not expected to exceed ~20%. The resolution (70 lines/mm) is not a severe limitation because of the large aperture available.

We have recently performed several holographic grating experiments with an "off-the-shelf" Hughes LCLV. In the first experiment, the two write beams (derived from a He-Ne laser) were collimated beams wilth ~5 mm diameter incident at an adjustable relative angle. The readout beam (from a separate He-Ne laser) were also collimated and had a diameter of ~2 mm. The locations of beams on opposite faces of the LCLV were set for optimum spatial overlap. With no voltage applied to the LCLV, only a specular reflected readout beam was observed. With the voltage set for optimum operation, a holographic grating is produced in the liquid crystal layer, leading to diffraction orders in the reflected readout beam. We have measured the first order scattering efficiency as a function of angular separation of the write beams. This measures the modulation transfer function (MTF) of the light valve since the spatial frequency is uniquely determined by the angular separation and the operating wavelength. An experimental plot of MTF is given in Figure 2-11. The limiting spatial frequency is ~25 cycles/mm, compared with ~35 cycles/mm obtained from improved Hughes light valves.

In a second experiment with the LCLV, the principle of aberration correction was demonstrated. The writing beams consisted of a collimated beam and a beam from a lens. The readout beam was also collimated, and the diffraction signal beam was shown to be converging, with a convergence angle equal to the divergence angle of the image writing beam. If we consider a lens as a simple phase aberrator, then a second lens placed in the signal beam (at the same distance from the LCLV as the lens in the image writing beam) would collimate the signal beam. This was, in fact, demonstrated, showing that the aberration of the lens was corrected.

C. ORGANIC MATERIALS

As mentioned earlier, long-chain organic polymers have been considered as possible candidates for DFWM (a third order nonlinear mechanism) by virtue of their large third-order nonlinear coefficients. The required value of the third order nonlinear susceptibility, $\chi^{(3)}$, for efficient DFWM with typical cw lasers is $\chi^{(3)} > 10^{-2}$ cm^3/erg = 10^{-2} esu. This value will be used as a standard in evaluating candidate organic materials.

In analyzing the nonlinear optical properties of organic materials, several questions should be considered. The first is, "Do solid and liquid organics that have large values of the second-order nonlinear susceptibility $\chi^{(2)}$ also have large values of the third-order nonlinear susceptibility $\chi^{(3)}$?" A literature search revealed that the answer is yes, and that this result is well known.

The second question is, "Can organics with large $\chi^{(3)}$ be predicted?" Again, the answer was found in the literature. The requirements to obtain large $\chi^{(3)}$ include π bonds, long straight molecules, and large charge displacement. A very simple, free-electron model is developed to illustrate these results.

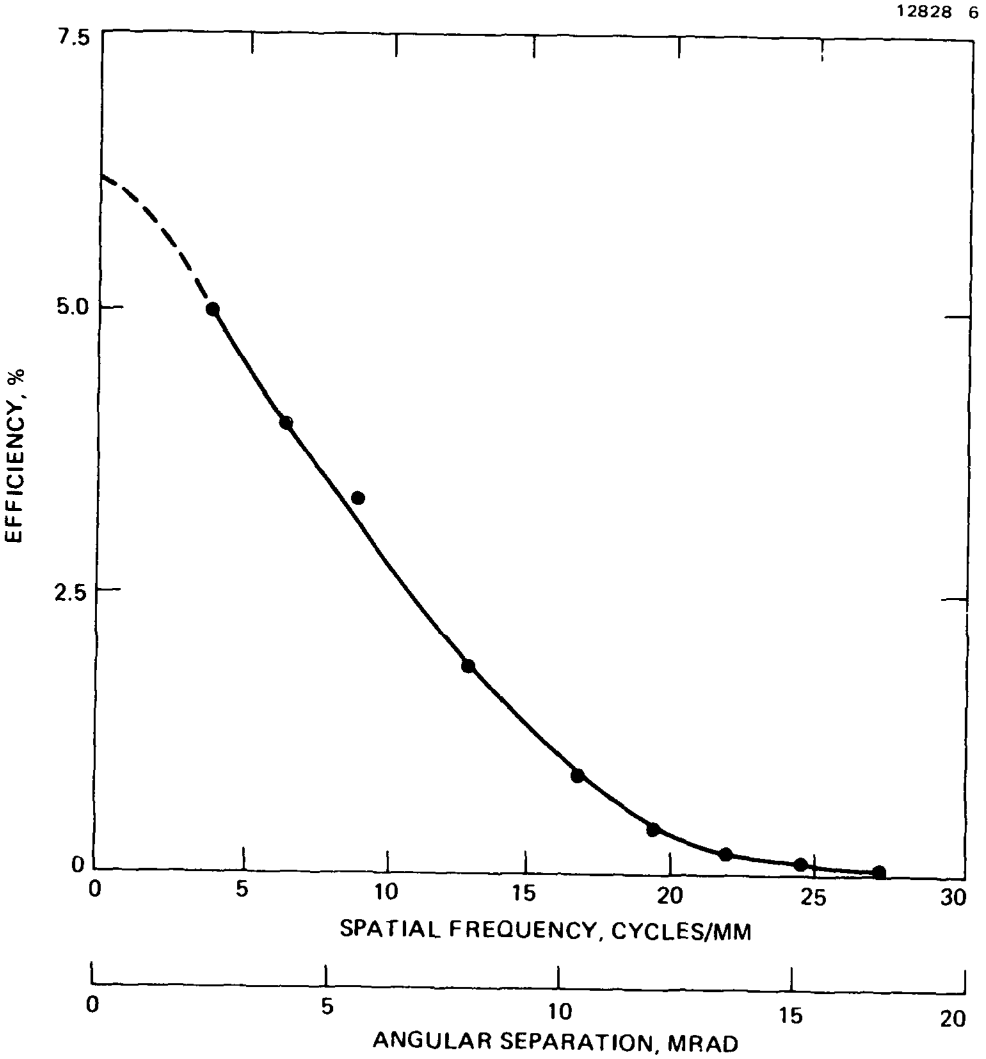

Figure 2-11. Measured MTF of liquid crystal light valve.

Additional questions that arose during the investigation are as follows: What maximum values of $\chi^{(3)}$ and time constant are attainable? The preliminary answer is that the limit is set by the conditions $L_{eff} = L_{\omega} = v/\omega$ and $L_{eff} = \Lambda_{mfp} = v\tau$, very roughly, where L_{eff} is the effective molecular length, ω is the optical infrared, or microwave frequency, and v and τ are the electron velocity and relaxation time. These condition appear to preclude the possibility of attaining exceptionally large values of $\chi^{(3)}$ in the visible region, but large values of $\chi^{(3)}$ are predicted at microwave frequencies below 100 GHz.

Donors and acceptors, which increase the value of $\chi^{(2)}$, also increase the value of $\chi^{(3)}$. The final question remains unanswered: Are the individual $\chi^{(1)}$, $\chi^{(2)}$, $\chi^{(3)}$, etc. meaningful when the χ's have such large values as $\chi^{(3)} = 10^{-2}$ cm^3/erg? A different approach, not treating the $\chi^{(n)}$ as small, may be necessary.

1. Physical Description of Large Susceptibilities

As illustrated in Figure 2-12, large dipole moments and large susceptibilities result from displacements of charge over great distances. In organic molecules, the strongly overlapping π bonds afford good conduction paths, as illustrated in Figure 2-13. Thus, long, π-bonded molecules have large susceptibilities.

It is known that the periodic structure of molecules that are not straight impedes the electron motion and slightly reduces the susceptibilities. However, this effect is less important than π bonds and great lengths.

2. Free-Electron Model

A simple free-electron model illustrates the central features of the large nonlinear susceptibilities. The molecule is represented by a box of length L with perfectly reflecting walls (see Figure 2-14). The applied electric field, E, accelerates the electron when it moves in the direction opposite to

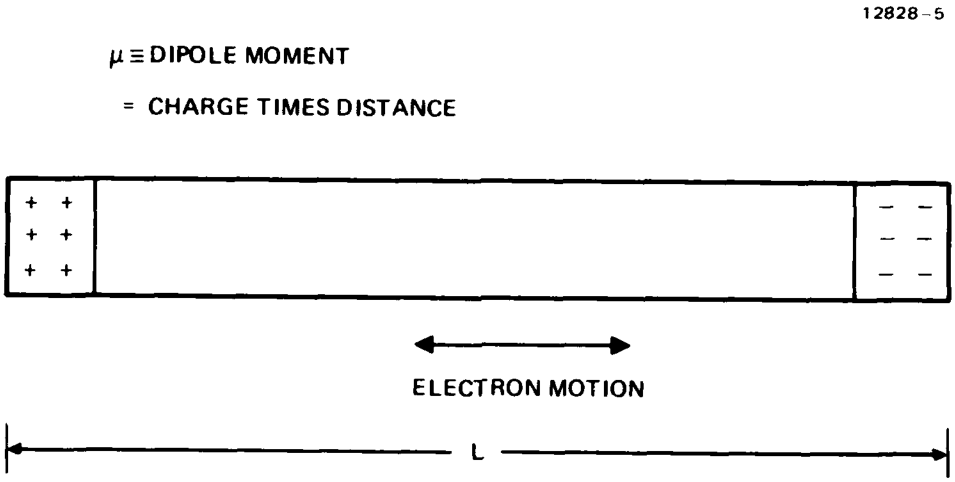
12828-5
μ ≡ DIPOLE MOMENT
= CHARGE TIMES DISTANCE
+ +
+ +
+ +
– –
– –
– –
ELECTRON MOTION
L

Figure 2-12. Long conduction paths have large dipole moments.

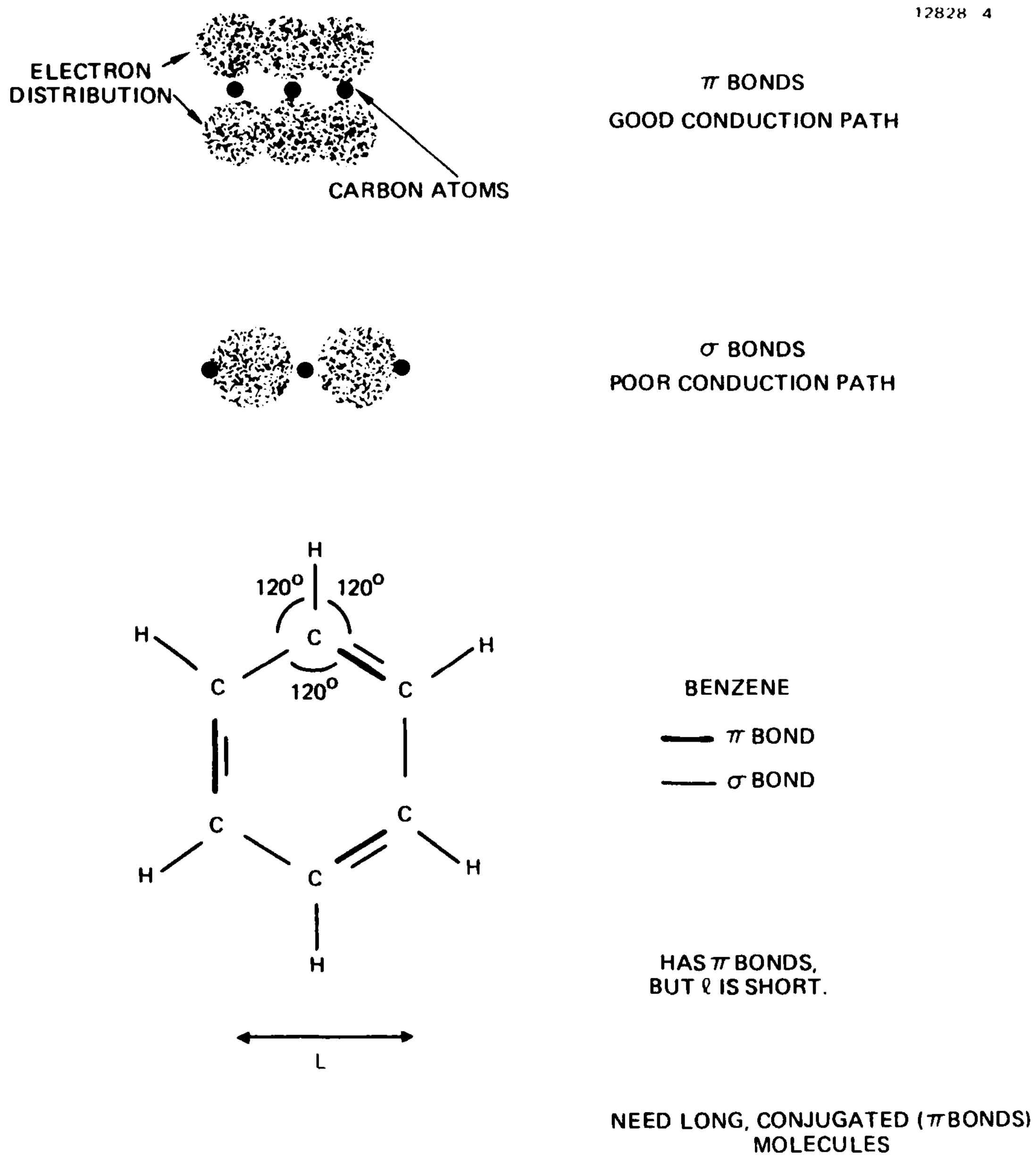
12828 4
ELECTRON DISTRIBUTION
CARBON ATOMS
π BONDS
GOOD CONDUCTION PATH
σ BONDS
POOR CONDUCTION PATH
H
120°
120°
C
H
H
C
120°
C
C
C
C
H
H
H
BENZENE
π BOND
σ BOND
HAS π BONDS,
BUT ℓ IS SHORT.
L
NEED LONG, CONJUGATED (π BONDS)
MOLECULES

Figure 2-13. Advantage of π bonds.

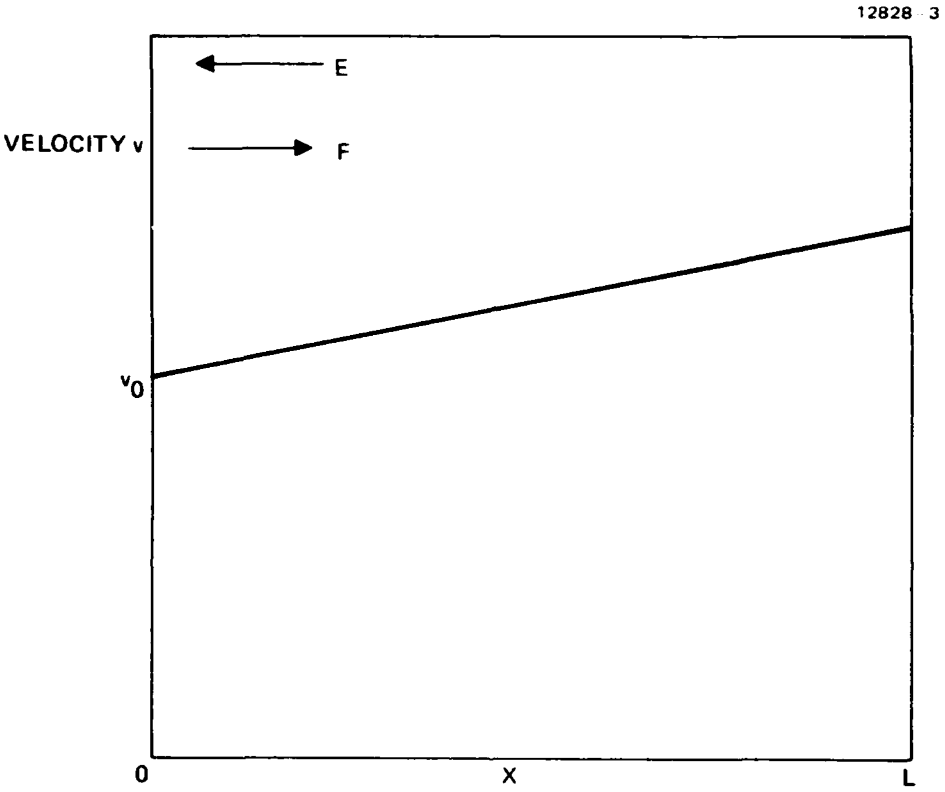
12828 3
E
F
VELOCITY v
v_0
0
X
L

Figure 2-14. Free electron model: One-dimensions box with reflecting walls.

E (force $F = -|e| E = e E$), and slows it down when it moves in the direction of E. The equation of motion is

$$m \frac{dv}{dt} = e E \quad . \tag{11}$$

The solution is

$$v = v_o + \frac{eEt}{m} = v_o(1+\delta) \quad , \tag{12}$$

where $\delta = e\,Et/mv_o$, $v_o = (2\varepsilon/m)^{1/2}$, and ε is the initial electron energy. The probability that an electron is between x and $x+dx$ is proportional to v^{-1}:

$$P_x dx = \frac{v^{-1}dx}{{}_o\int^L v^{-1}dx} \quad . \tag{13}$$

The dipole moment is easily calculated from P_x using the expression

$$\mu = e \int_o^L P_x(x-L/2)dx \tag{14}$$

$$= \alpha E + \beta E^2 + \gamma E^3 \quad , \tag{15}$$

where α, β and γ are known as hyperpolarizabilities. The induced polarization is

$$P = R\mu/V = \chi^{(1)}E + \chi^{(2)}E + \chi^{(3)}E^3 \quad . \tag{16}$$

where R is a form factor, and V is the volume, proportional to L, the length of the box.

To continue with our solution for μ, we consider the limit of small E ($\delta<<1$):

$$v^{-1} \approx v_o^{-1} (1-\delta+\delta^2-\delta^3+ \ldots) \quad . \tag{17}$$

We can relate t to z by integrating the equation of motion for v:

$$x = \int_0^t vdt = vot + (eE/2m)t^2 \quad . \qquad (18)$$

We thus find that

$$\delta = \frac{eEt}{mv_o} = -1 + \left(1 + \frac{2exE}{mv_o^2}\right)^{1/2} \quad . \qquad (19)$$

Finally, by combining Equations (13), (14), (15), (17), and (19), we find that

$$\begin{aligned} \gamma &= \frac{1}{36} \frac{e^4 L^4}{\varepsilon^3} \\ &= 3.6 \times 10^{-36} L^4 \varepsilon^{-3} \text{ cm}^6/\text{erg}, \end{aligned} \qquad (20)$$

where L is in Å and ε is in eV. Using typical values[10] for the local field correlation factor, and taking into account the linear dependence of molecular volume on length, we find that

$$\chi^{(3)} \approx 3.6 \times 10^{-15} L^3 \varepsilon^3 \text{ cm}^3/\text{erg} \quad . \qquad (21)$$

Experiments by Hermann and Ducuing[10] have confirmed the predicted L^4 dependence of γ. Molecules with as many as 30 double bonds were considered, corresponding to $\gamma \approx 10^{-31}$ cm^6/erg. The model also gives the correct order of magnitude for γ if $\varepsilon \approx 1$ eV is used.

3. Giant Values of Nonlinear Suscepibilities

The formal use of the above model, which gives such good agreement with experimental values for molecules up to ~20 bonds in length, predicts enormous values of $\chi^{(3)}$ for sufficiently long molecules. For example, we find from Equation (18) that a length of L = 2.3 μm gives rise to $\chi^{(3)} = 10^{-2}$ cm^3/erg.

Intuitively, such giant values of $\chi^{(3)}$ seem unlikely. In order to determine if these are fundamentally possible, we ask that the practical limit is to L. Polymer physicists believe that molecules 3 μm long are possible; so the physical length is not believed to be the limit.

The first limit is the electron mean free path, Λ_{mfp}. If $\Lambda_{mfp} \ll L$, then the velocity is $v \cong \mu E$ (where the mobility is $\mu = e\tau/m$, and τ is the electron relaxation time for momentum reversal), rather than $v = v_o + eEt/m$, and given in Equation (12). In this case of $\Lambda_{mfp} \ll L$, the velocity is nearly constant so that the probability P_x is nearly constant, and μ is small.

As an estimate of the value of Λ_{mfp} for organics, use

$$\Lambda_{mfp} = v\tau \quad . \tag{22}$$

With

$$v = (2\ \varepsilon/m)^{1/2} \cong 10^8\ \text{cm/S}$$

for free electron and

$$\begin{aligned} \tau &= m\mu/e \\ &= 2.8 \times 10^{-13}\text{s} \end{aligned} \tag{23}$$

for $\mu = 500\ \text{cm}^2/\text{Vs} = 1.5\text{x}10^5\ \text{cm}^2/\text{statvolts}$, Equation (22) gives

$$\Lambda_{mfp} \cong 0.28\ \mu\text{m} \quad .$$

With $L = \Lambda_{mfp} = 0.28\ \mu\text{m}$, we find that

$$\begin{aligned} \chi^{(3)} &\cong (10^{-2}\ \text{cm}^3/\text{erg})(0.28\ \mu\text{m}/2.8\ \mu\text{m})^3 \\ &\cong 10^{-5}\ \text{cm}^3/\text{erg} \quad , \end{aligned} \tag{24}$$

as a very rough estimate.

Next, consider the frequency restriction. The distance the electron travels before the electric field reverse is, roughly, for $\lambda = 0.53\ \mu m$,

$$L_{\omega} = v/\omega$$
$$= 2.8 \times 10^{-8}\ cm = 2.8 \times 10^{-4}\ \mu m \quad .$$

Formally setting $L = L_{\omega} = 2.8 \times 10^{-4}\ \mu m$ gives

$$\chi^{(3)} = 10^{-14}\ cm^{3}/erg \quad ,$$

which is not large because L = 2.8 Å is short. This example illustrates that giant values of $\chi^{(3)}$ are precluded at optical frequencies by the frequency limitation.

For a microwave frequency of, say, 10 GHz, the value of L_{ω} is

$$L_{\omega} = 1.6 \times 10^{-3}\ cm = 16\ \mu m \quad .$$

With $L = L_{\omega} = 16\ \mu m$, we find that

$$\chi^{(3)} = 1.9\ cm^{3}/erg \quad .$$

This large value of $\chi^{(3)}$ indicates that the frequency limitation for $\chi^{(3)}$ in the microwave region is not the final limitation. The mean-free-path limitation restricts the value of $\chi^{(3)}$ in the microwave region to $\chi^{(3)} \cong 10^{-5}\ cm^{3}/erg$, according to Equation (24), which is a very rough estimate. These very rough estimates suggest that values of $\chi^{(3)} \cong 10^{-5}\ cm^{3}/erg$ may be attainable at microwave frequencies.

SECTION 3

IMAGE TRANSMISSION THROUGH FIBERS USING PHASE CONJUGATION AND THE USE OF FIBERS AS THE PHASE CONJUGATOR

In this portion of the program we demonstated the transmission of images through optical fibers using phase conjugation. We also investigated the suitability of commercially available fibers to serve as the nonlinear medium.

A. TRANSMISSION OF IMAGES THROUGH FIBERS USING PHASE CONJUGATION

During this portion of the program we demonstrated the transmission of images through multimode fiber waveguides using optical phase conjugation[11] or wavefront reversal techniques. The transmission of spatial information through fibers is degraded due to mode mixing and modal dispersion. By making use of the wavefront reversal property of nonlinear optical techniques[12] we can compensate for these effects. In our preliminary experiments an image was transmitted through a fiber, conjugated, and made to retraverse the same fiber, resulting in the reconstruction of the image at the input end of the fiber. For this to be a useful forward transmission technique, operation with two nearly identical fibers will be required. The image will be transmitted through the first fiber, conjugated, and then transmitted through the second fiber which reconstructs the image at its output.

The preliminary demonstration[3] was accomplished by utilizing a multimode (85 μm diameter, 1.75 m long) step-index fiber. The results of this experiment were published in Optics Letters 7, No. 11, p.558, in an article entitled "Demonstration of image transmission through fibers by optical phase conjugation". The manuscript is included as Appendix E. The output of an argon laser (5145 Å) was transmitted through a portion of an Air Force resolution chart and imaged at the input end of the fiber. The fiber output was directed into a crystal of barium titanate ($BaTiO_3$) in which DFWM was used to generate the phase conjugate signal. The phase conjugate signal then retraversed the same fiber and reconstructed the image of the resolution chart. The results of this experiment are shown in Figure 3-1. The first photograph shows the input image of an Air Force resolution chart. The second photograph shows the output at the end of the fiber. The output is typical of a highly multimode fiber where a large number of modes are

11210-2R2

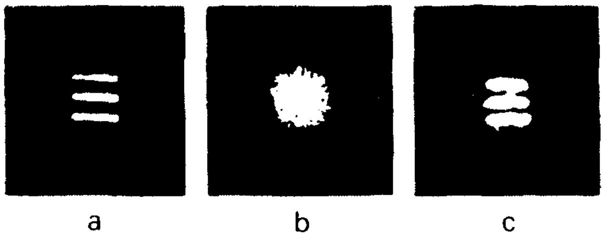

Figure 3-1.
Demonstration of image transmission through a fiber. (a) Image of Air Force resolution chart at input end of fiber. (b) Output after a single pass through the fiber. (c) Reconstruction of resolution chart after output has been phase conjugated and retraverses fiber.

excited. From the output, it is impossible to discern that any spatial information has been transmitted through the fiber. The reconstructed image after double passing the fiber is shown in the last photograph.

Geometry employed for the four-wave mixing experiments in this work is shown in Figure 2-3. It consists of two counterpropagating pumps (E_f,E_b) and a probe wave (E_p) (which is the beam with the image information imposed on it) incident on the nonlinear medium. These beams interact to generate the phase conjugate signal (E_s).

A schematic of the experiment is shown in Figure 3-2 and the experimental apparatus is shown in Figure 3-3. The argon-ion laser (5145 Å) used as the illumination source has an intracavity prism and etalon for single longitudinal mode operation giving coherence lengths on the order of 10 m. In order to have useful interference between the pump and probe the coherence length of the laser must be comparable to the path length differences encountered in the experiment. For our experiments the probe path length is longer than the path length of the pump beams by at least the length of the fiber, thus requiring the ~10 m coherence length.

The laser output is continually monitored by a scanning Fabry-Perot etalon. Because of crystal orientation, p-polarization of the input beams is required in our experiments. Therefore, a λ/2 plate and Faraday rotator were used to rotate the plane of polarization of the argon laser. The Faraday rotator was also used in conjunction with a polarizer to prevent any return beams from entering the laser and destroying single mode operation. The beam splitter, BS2, picks off the pump beams. A 100 cm f.l. lens was used to reduce the pump beam size in the crystal. The beam splitter, BS3, picked off a secondary probe signal which was used to optimize the crystal orientation. The beam splitter, BS4, was used to generate the individual counterpropagating pumps. The pumps typically have a power ratio of 2:1. The throughput of the beam splitter, BS2, is used

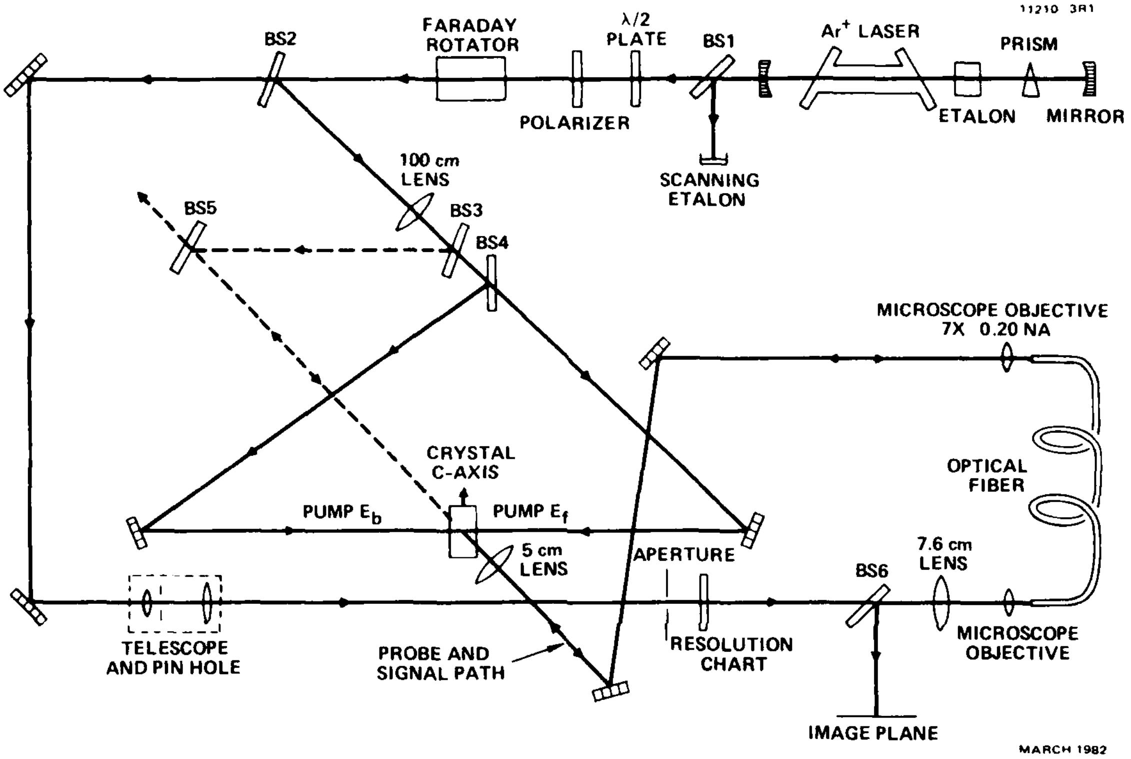
11210 3R1
FARADAY ROTATOR
λ/2 PLATE
BS2
BS1
Ar+ LASER
PRISM
POLARIZER
ETALON
MIRROR
100 cm LENS
SCANNING ETALON
BS5
BS3
BS4
MICROSCOPE OBJECTIVE 7X 0.20 NA
CRYSTAL C-AXIS
OPTICAL FIBER
PUMP Eb
PUMP Ef
5 cm LENS
APERTURE
7.6 cm LENS
BS6
TELESCOPE AND PIN HOLE
PROBE AND SIGNAL PATH
RESOLUTION CHART
MICROSCOPE OBJECTIVE
IMAGE PLANE
MARCH 1982

Figure 3-2. Schematic of experiment used for image transmission through fibers.

MC14076

11368 8

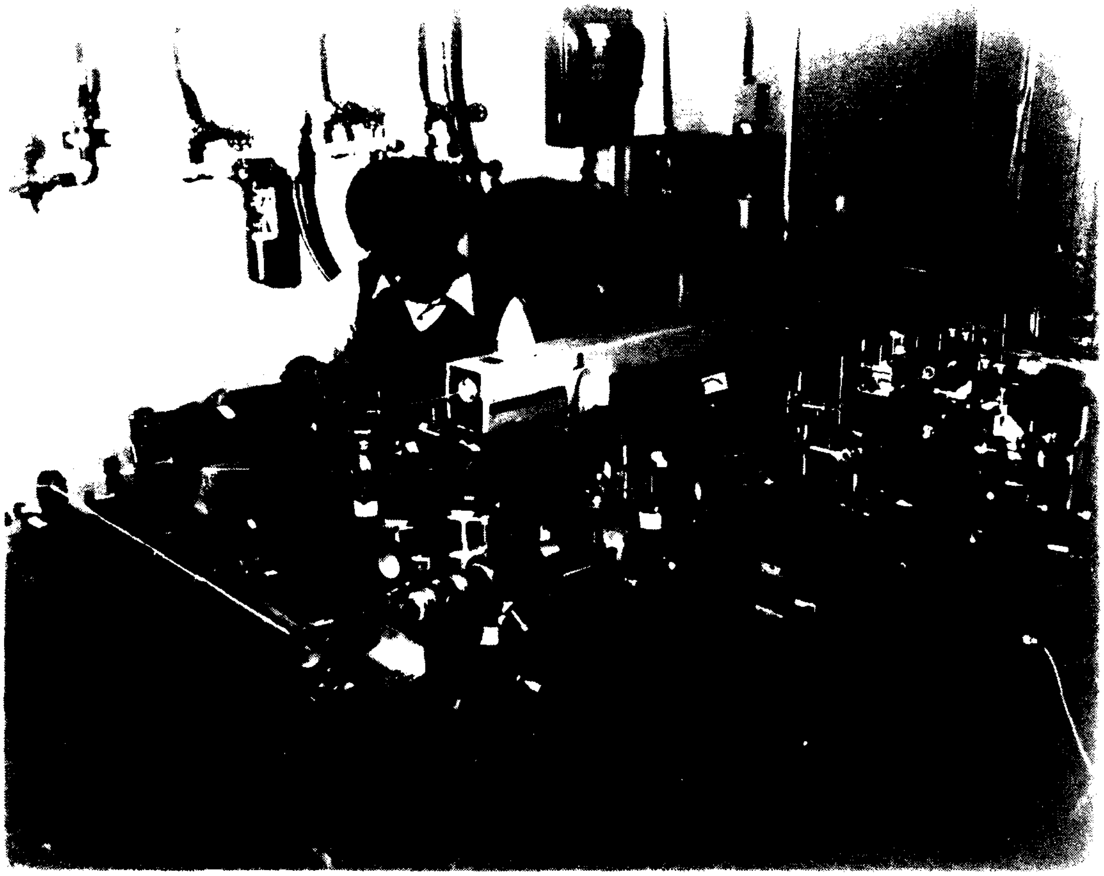

Figure 3-3. Photograph of experimental apparatus used for image transmission through fibers.

to obtain the probe used in the fiber. This probe beam was expanded by a beam expanding telescope to illuminate the Air Force resolution chart. Following the resolution chart is a beam splitter, BS6. This element is used to pick off the return signal which forms an image on a sheet of cardboard. The image plane is the exact same distance from the beam splitter as the original Air Force chart. An f.l., 7.6 cm focal length relay lens was used to capture the light diffracted by the patterns of the resolution chart. This diffracted light would otherwise miss the entrance aperture at the microscopic objective. The microscope objectives are 7X, 0.20 N.A. The first microscope objective couples the light into the fiber. The fibers are held by a unique Hughes-designed fiber holder and fiber assembly which has five degrees of freedom: x - y - z translation and azimuthal and polar rotations.

In our studies we have used four types of fibers which are representative of the various fiber designs. The first fiber is a "single" or lower mode number fiber from Bell Laboratories. It has a step index with a core diameter of 8.5 μm and a numerical aperture, N.A., of 0.052. There are several lengths, the longest being 60 m. At the wavelengths of interest, ~5000 Å, we can propagate three discrete modes, of which two are degenerate. The number of modes, M, is given by $M = k^2a^2(N.A.)^2$, where a is the core diameter. The second fiber is a multimode graded index fiber supplied by ITT. The core diameter is 50 μm, the N.A. is 0.25 and the length is 6 m. Theoretically, approximately 10^4 modes can propagate in this fiber at the wavelengths of interest. The third fiber is a Corning 85 μm step index fiber (N.A. = 0.184) which is 1.75 m in length. It also can propagate ~10^4 modes. The fourth fiber is a multimode step index fiber supplied by Quartz Products. The core diameter is 200 μm and the N.A. is 0.20. This fiber can support on the order of 10^5 modes. We have measured the properties of fiber transmission at three different wavelengths, 4131 Å, 5145 Å, and 6471 Å, so that we can optimize both the wavelength and fiber for a particular experiment. As mentioned for the initial image transmission studies, we used the Corning 85 μm fiber.

A second microscope objective (see Figure 3-2) quasicollimates the output beam from the fiber. A 5 cm focal length lens is then used to reduce the probe beam to a diameter smaller than the diameter of the pump beams inside the crystal. The pumps typically make an angle of 75° with respect to the c-axis and the probe, which has an angle of 68°. This implies that the angle of the grating normal is 18° with respect to the c-axis. The highest reflectivity is obtained when the grating vector is inclined to the positive c-axis direction, as predicted by Feinberg and Hellwarth.[1] Using this geometry we have obtained reflectivities in excess of 133%.

These large returns have enabled us to easily reconstruct the image and show image amplifiction. At present we have been able to resolve better than 15 lines/mm (67 μm spacing), see Figure 3-4. (The resolution of the optical system without the fiber is >20 lines/mm; and we have seen in a separate high resolution set-up greater than 114 lines/mm (9 μm spacing) in $BaTiO_3$ by itself.) The imaging geometry used for these preliminary demonstrations is not optimized. In addition, effects such as damping of the higher order modes relative to the lower order modes (which could cause a scrambling or loss of informtion) and polarization scrambing can effect the image quality. In the latter case typical commercial fibers do not preserve polarization. Hence, the linearly polarized input probe beam will emerge randomly polarized. For our DFWM experiments the pumps are linearly polarized in the plane of the experiment and only this component of polarization is conjugated.

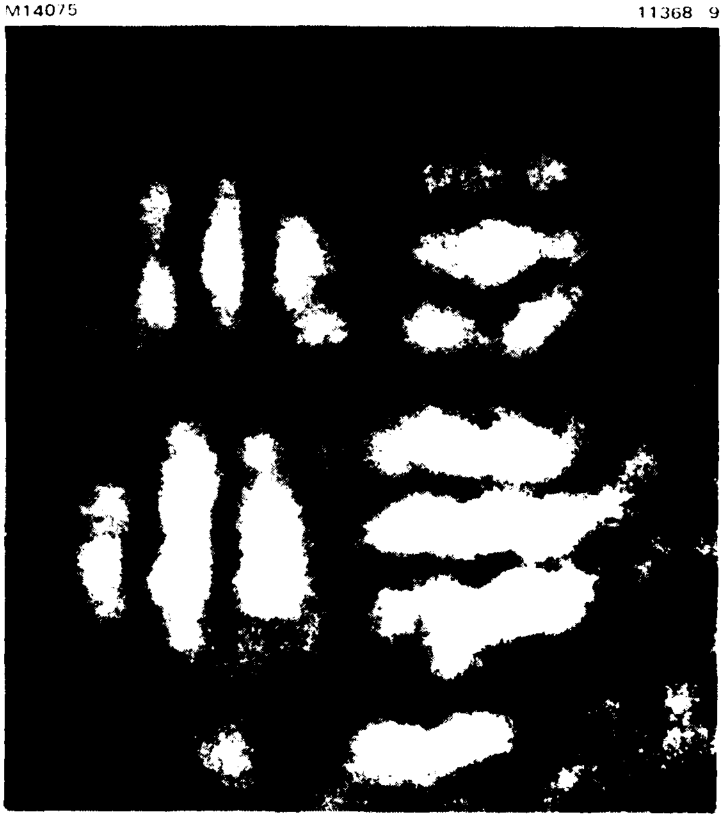
M14075
11368 9

Figure 3-4. Reconstructed image after double passing the fiber. These experiments show the resolution is in excess of 15 lines/mm.

B. PHASE CONJUGATION USING OPTICAL FIBERS AS THE NON-LINEAR MEDIUM

Because of the possible systems applications it was of interest to see if a fiber could be used as the nonlinear medium itself. The experimental arrangement for the DFWM experiments using fused silica fibers as the phase conjugate medium is shown in Figure 3-5. The forward pump and probe were brought in parallel to each other and were symmetrically displaced from the optic axis of the first lens. This lens was designed to couple the forward pump and probe into the low order modes of the fiber. The backward pump was coupled into the other end of the fiber by a microscope objective. The backward pump was also aligned to launch only low order modes. The fibers used were typically 5 m in length and have been discussed in Section 3A.

In performing these tests we encountered difficulties in determining if, in fact, a DFWM signal was observed because of signal-to-noise problems fundamental to a DFWM experiment in fibers. There are two basic noise sources, one arising from the backward traveling pump and the other due to Fresnel reflection of the probe from the input end of the fiber. Both signals limit the DFWM reflectivity that can be detected and are larger than the expected signal based on a simple calculation (see below). (To understand these noise sources refer to Figure 3-5.) The experimental arrangement allowed us, in principle, to spatially separate the forward pump, backward pump and probe. The signal was separated from the probe path by the signal-beam splitter. There were two competing design considerations. For best coupling it was necessary for the forward pump and probe to be physically collinear with the optic axis of the first lens. But for good phase conjugate signal separation the probe should be as far from the optic axis as is physically possible; i.e., as close to the edge of the lens aperture as

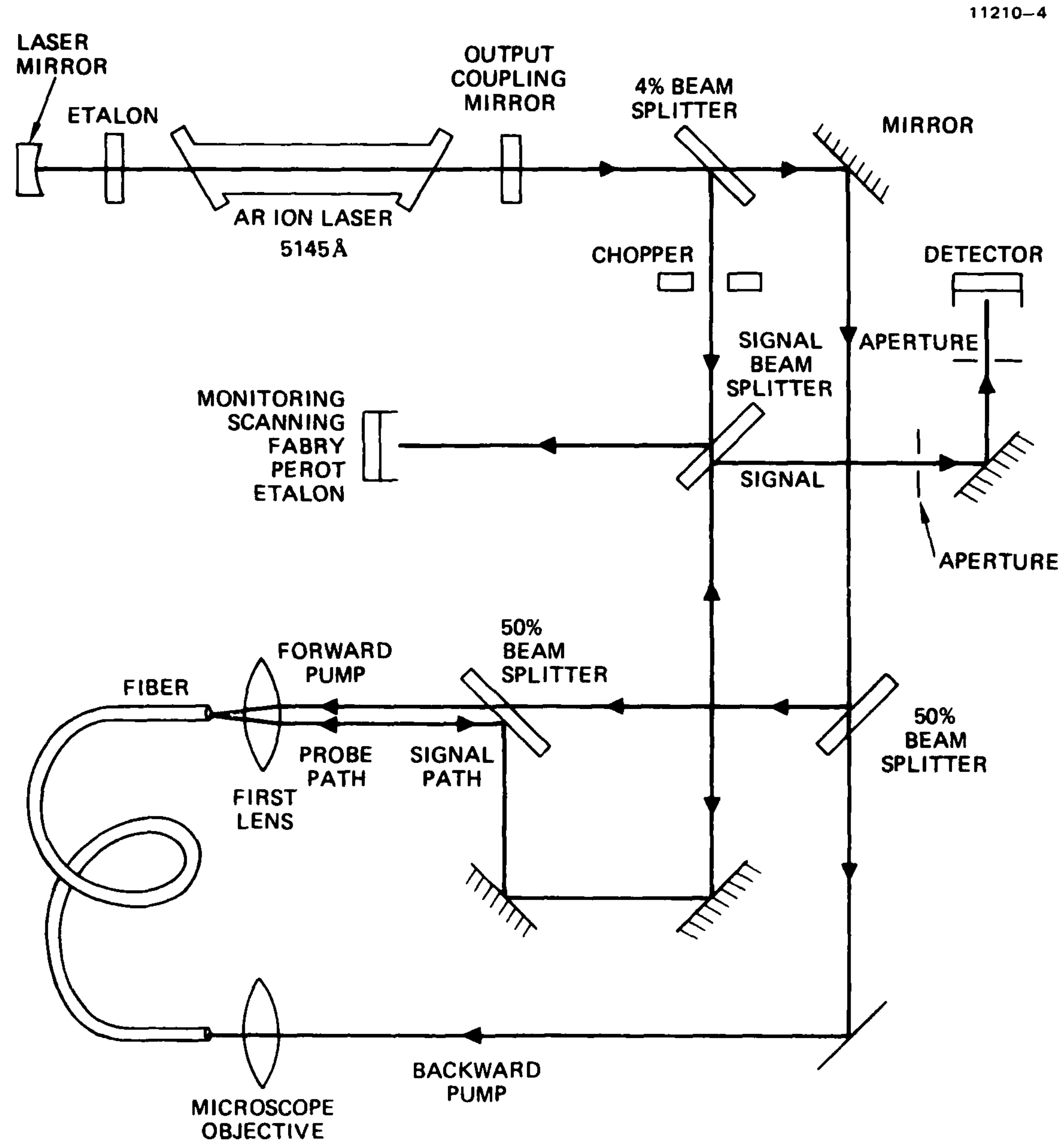
11210–4
LASER MIRROR
ETALON
AR ION LASER 5145Å
OUTPUT COUPLING MIRROR
4% BEAM SPLITTER
MIRROR
CHOPPER
DETECTOR
SIGNAL BEAM SPLITTER
APERTURE
MONITORING SCANNING FABRY PEROT ETALON
SIGNAL
APERTURE
50% BEAM SPLITTER
FORWARD PUMP
FIBER
PROBE PATH
SIGNAL PATH
FIRST LENS
50% BEAM SPLITTER
BACKWARD PUMP
MICROSCOPE OBJECTIVE

Figure 3-5. Schematic of degenerate four wave mixing experiments using silica fiber as nonlinear medium.

possible. In our preliminary work we attempted a compromise between these conditions. Unfortunately, because of mode coupling in the fiber there was enough energy coupled from the backward pump into higher order modes that the energy in these modes traveled back along the same path as the signal. Phase lock detection was used (while chopping the probe), but the scattered backward pump prevented a conclusive measurement. The second source was the probe retro-reflection off the end of the fiber and coupling optics. We were able to reduce this retro-reflection by incorporating a polarizer/quarter wave plate combination. The linearly polarized light from the polarizer passed through the $\lambda/4$ plate at 45°, with respect to the ordinary and extraordinary axis. The emergent light was then circularly polarized and impinged on the fiber end. The reflected light was also circularly polarized. The light then retraversed the $\lambda/4$ plate and emerged linearly polarized but now perpendicular to the input polarization and was attenuated by the polarizer. The signal polarization is not preserved in the fiber and emerged with a random polarization and the component parallel to the polarizer was passed. Even with this solution to the retro reflection problem, we were unable to detect a DFWM signal, which is not surprising if one does a simple calculation of the expected conjugate signal strength, as given below.

For a nonresonant material the phase conjugate reflectivity is given by

$$R = \tan^2 |K|\ell \quad , \tag{5}$$

where

$$|K| \ (\mathrm{cm}^{-1}) = \left(32 \times 10^7 \frac{\pi^3}{C}\right) \frac{\chi^{(3)} \ (\mathrm{esu})}{\lambda \ (\mathrm{cm}) \ n^2} \quad I_1 I_2 \ (\mathrm{w/cm}^2) \ . \tag{6}$$

For silica glass the linear and nonlinear indices of refraction are:

$$n_0 = 1.5$$

and

$$n_2 = 1.8 \times 10^{-13} \text{ esu},$$

giving

$$\chi^{(3)} = \frac{n_2 n_0}{2\pi} = 4.3 \times 10^{-14} \text{ esu} .$$

For fiber diameters of 100 μm and for an input powr of 1 W, $I = 2 \times 10^2$. Thus ,for a wavelength of 0.5 μm and a fiber length of 100 cm, $R = 10^{-5}\%$. In order to increase this reflectivity one should dope the fiber, thus increasing the nonlinear susceptibility. The use of optical fibers as the nonlinear medium for phase conjugation will require the development of fibers with a higher nonlinear susceptibility than are presently available.

SECTION 4

TWO-WAVE MIXING

One technique for studying the photorefractive effect is to examine the energy coupling between a probe beam and a pump beam in a two-wave mixing experiment*. The probe and pump interfere in the crystal, forming a fringe pattern throughout the volume. These fields cause a migration and separation of changes in the crystal, thereby creating an internal space charge electric field. This field produces a change in the refractive index by the electro-optic effect and creates a volume phase hologram. In photorefractive materials the refractive index grating and the two beam interference pattern are shifted in phase spatically. The phase shift for $BaTiO_3$ is typically 90° out of phase; this causes energy to be transferred betwen the pump and probe beams. (See Figure 2 in Appendix C).

An experiment to investigate beam coupling in $BaTiO_3$ was conducted, a schematic of which is shown in Figure 4-1. In the probe path were two acousto-optic (A.O.) modulators. By modulating the carrier frequency of the first A.O. modulator it is possible to generate a temporal variation in intensity of the probe beam. The diffracted order is a replica of the waveform of the envelope of the acoustic carrier frequency. The diffracted order, however, is shifted from the original input laser frequency by the acoustic carrier frequency. Because useful interference in the $BaTiO_3$ requires that the probe and pump must be at the same frequency, a second unmodulated A.O. cell is used to shift the probe frequency back to the original laser frequency.

After diffracting from the A.O. modulators, the probe beam propagates to the $BaTiO_3$ crystal where it interacts with the pump beam. In these experiments the pump is cw and is unmodulated. The pump flux is typically ten to one hundred times the probe flux.

---

*This work was supported by IR&D funding and is included here due to its relevence to this program.

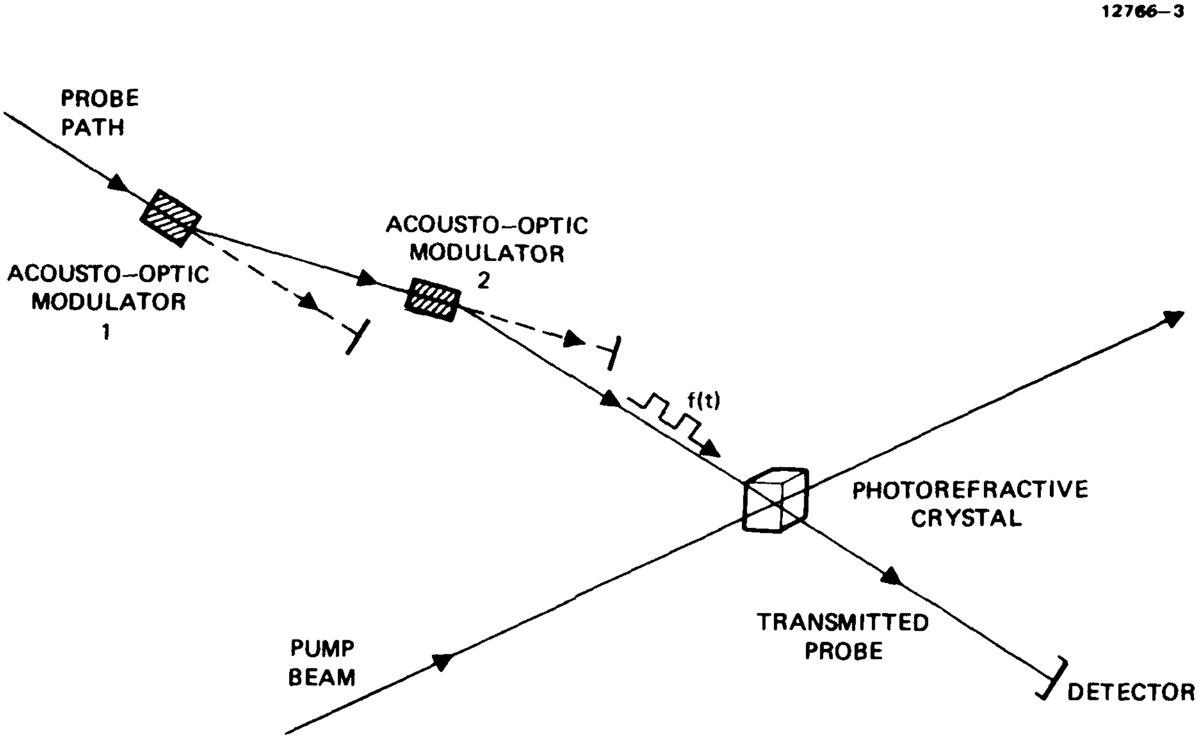
12766-3
PROBE
PATH
ACOUSTO-OPTIC
MODULATOR
1
ACOUSTO-OPTIC
MODULATOR
2
f(t)
PHOTOREFRACTIVE
CRYSTAL
TRANSMITTED
PROBE
PUMP
BEAM
DETECTOR

Figure 4-1. Two-beam coupling experiment schematic.

After experiencing amplification in the crystal, the transmitted probe beam is detected by a photomultiplier tube. The signal is then displayed on either an oscilloscope or a chart recorder.

Three types of modulation on the probe beam were investigated. The first is a single pulse event, the second is a continuous unmodulated beam, and the third is a repetitive waveform. An example of the single pulse event is shown in Figure 4-2a. The lower trace shows the transmitted probe in the absence of the pump beam. It is seen to be a square wave of 20 mV amplitude and 1300 msec duration. The upper trace is the transmitted probe when the pump beam is present. Because of two-beam coupling, some of the energy of the pump beam is diffracted in the direction of the transmitted probe. This results in amplification of the transmitted probe. In Figure 4-2a the amplification is a factor of twenty-three at the highest value. This result was obtained for an internal pump-probe angle of 3.5° and an angle between the c-axis and grating normal of 16.8°. The power in the pump was 33 mW, while the probe power was 83 μW.

The rise time of the transmitted probe pulse is related to the time constant associated with the grating formation. The flat portion is equal to the steady-state value when the probe is unmodulated. The decay of the transmitted probe is characterized by a very fast initial change, followed by a slower decay associated with grating erasure. It is believed that the fast decay is a coherent effect due to removal of the input probe beam. If we consider the grating to have an amplitude reflectivity η, and we assume that the transmitted probe results from the coherent addition of the diffracted pump and the undiffracted probe, then the transmitted probe intensity can be approximated as

$$I_{probe}(z=L) = (1-\eta)^2 I_{probe}(z=0) + \eta^2 I_{pump}(z=0) + \eta^2(1-\eta)^2 (I_{pump} I_{probe})^{1/2} .$$

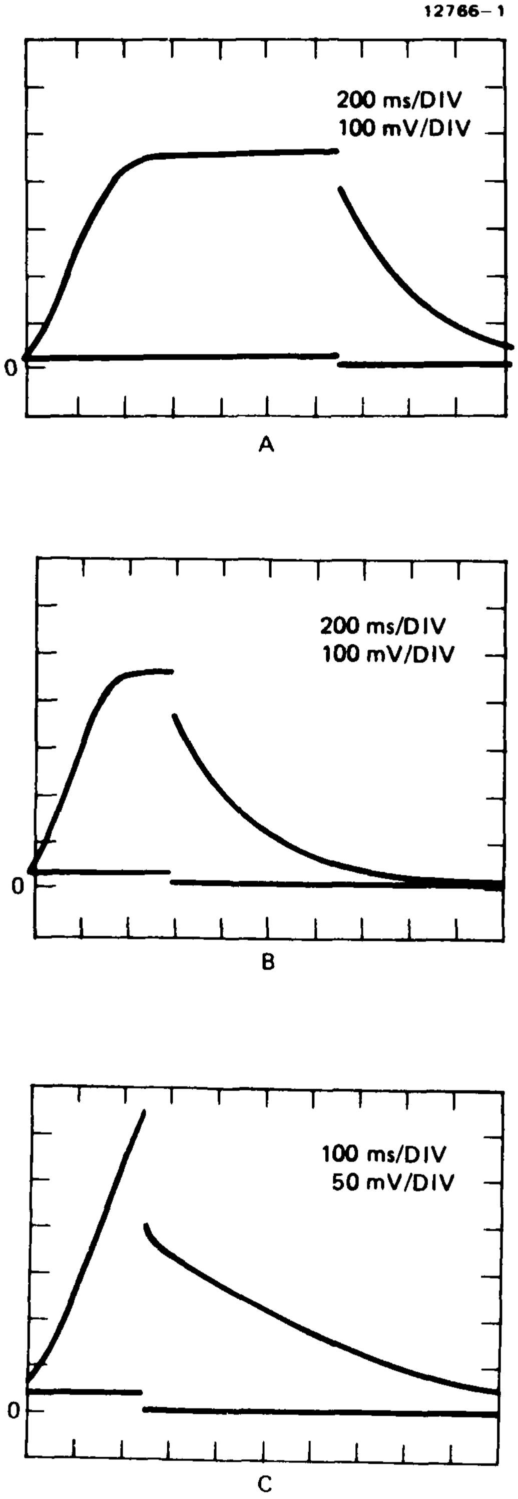

Figure 4-2.
Single pulse data for two-beam coupling experiment incident probe pulse lower trace, amplified probe pulse upper trace.

When the probe is turned off, the first and third terms go to zero in the probe switching time (200 nsec). The difference in magnitude between the probe signal when switched off (lower trace) and the amplified signal when switched off (upper trace) is the contribution of the third term. Affer the probe is turned off the grating which was formed continues to be read by the pump beam and energy is diffracted in the transmitted probe direction. As the pump beam is reading the grating it is simultaneously erasing the grating. Thus, the contribution from the second term decays at a rate characteristic of the refractive index grating erasure time in photorefractive materials. This is demonstrated by the exponentially decaying tail (τ = 0.35 sec).

If the pulse length of the probe beam is shorter than the write time (typically on the order of the decay time, 350 msec), the transmitted probe will not reach the maximum value obtained in Figure 4-2a. The transmitted probe will build up with the same rise time but will not reach the steady-state value, as illustrated in Figure 4-2c. (Note that the vertical scale in Figure 4-2a and 4-2b are 100 mv/division, and for 50-2c the vertical scale is 50 mV/division.) The magnitude of the discontinuity is independent of the pulse length. The decay time of the trailing edge is also seen to be independent of pulse length.

The theory presented in Section 1 and Appendix D describes the charge densities generated for a pulse probe beam and cw pump beam. The amplified probe beam will qualitatively follow the charge density. The computer generated graphs in Section 1, Figures 4, 5 and 6 are for probe pulse greater than, equal to, and less than the dielectric relaxation time. The theory is seen to agree well with the data of Figures 4-2(a), 4-2(b) and 4-2(c).

The second modulation regime occurs when the incident probe is unmodulated. When the probe is first tuned on, the two wave coupling signal rises to a constant "saturated" value. This value is represented by curve A in Figure 4-3. This signal level will be refered to as the cw level. This is the same level obtained by a single pulse if the pulse duration is greater than the write and erase times.

The third regime occurs when the modulation of the probe is a repetitive waveform. In this case the transmitted probe signal depends upon whether the period of the waveform is greater than or less than the dielectric relaxation time (τ). If the period is greater than τ the depth of modulation is one hundred percent. This case is shown in the data of Figure 4-3, curve B. The signal rises from zero with the characteristic material response rise time to the cw steady-state value. When the probe pulse is switched off, the diffracted pump energy decay back down to the zero point. This waveform is repeated and is similar to a continuous train of individual pulse response. However, when the waveform period is less than τ several interesting things occur. These are illustrated in the data shown in Fiure 4-4a. In the first cycle the transmitted probe (upper trace) is superimposed over that of a single pulse (lower trace). However, instead of decaying back down to the zero level it has a finite value when the next increasing portion of the probe waveform occurs. The signal then rises until the probe waveform begins to decrease. This increase and decrease in the signal finally evolves in to a steady-state waveform which is comprised of a dc level added to a periodic component proportional to the incident probe waveform.

Further examination of Figure 4-3 reveals other information about two-wave mixing. It is evident that the depth of modulation is a function of the period, and is demonstrated by comparing traces B(T=10 sec), C(T=1 sec), and D(T=0.1 sec). The dc component in the signal tends toward the cw level (curve A) times the duty cycle (50%). This was verified in other

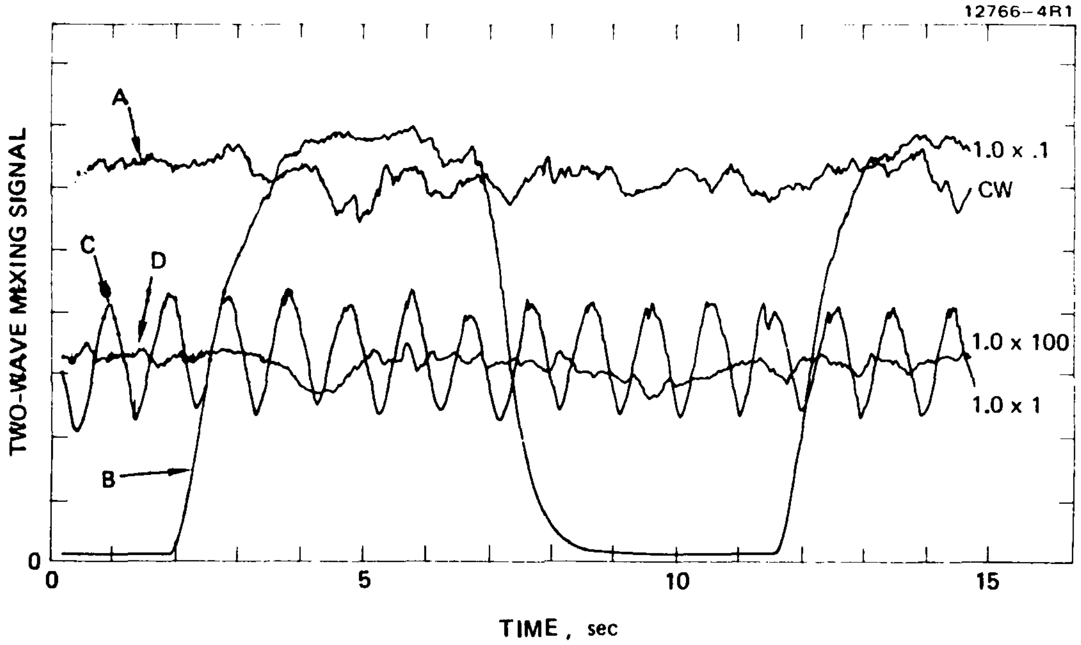

Figure 4-3. Repetitive waveform data for two-beam coupling experiment. A. Probe cw. B. Probe 0.1 Hz square wave. C. Probe 1.0 Hz square wave. D. Probe 100 Hz square wave.

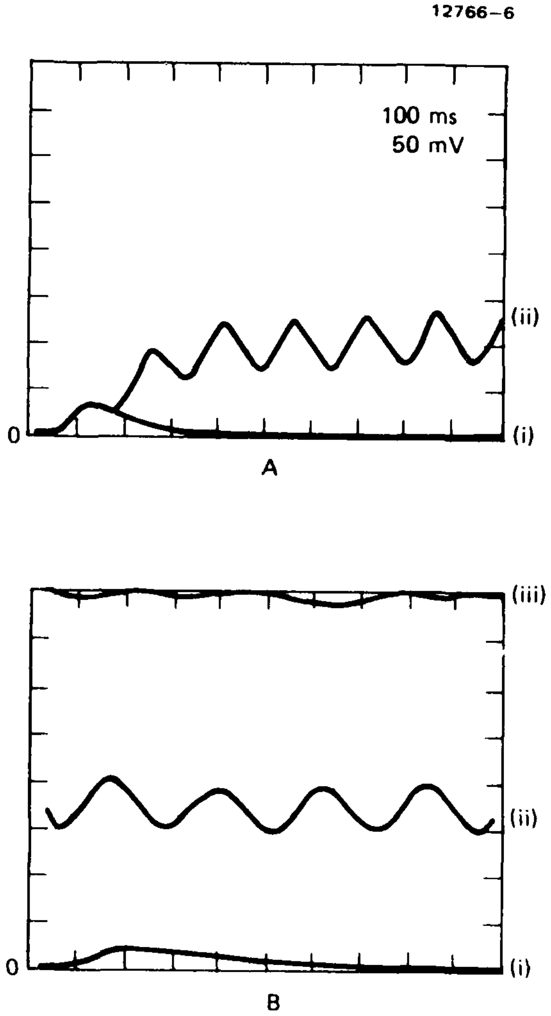

Figure 4-4. Degenerate four wave mixing signal when probe is (i) A single pulse, (ii) a repetitive waveform, (iii) constant value.

experiments, the results of which are not shown. These three cases are clearly illustrated in Figure 4-4b. The upper trace (iii) is obtained when the probe is cw. The middle trace (ii) results from a continuous waveform, while the lower trace (i) is the result of a single pulse.

SECTION 5

OPTICAL CONVOLUTION AND CORRELATION

This portion of the program was directed toward the demonstration of optical convolution and correlation. The first section addresses static two-dimensional optical processing. The second section describes efforts toward demonstrating real-time optical correlation.

A. STATIC TWO DIMENSIONAL OPTICAL CONVOLUTION AND CORRELATION

The major thrust of these experiments was the generation of convolutions and correlations of two spatially modulated input waves. The geometry of the experiment is shown in Figure 5-1. The geometry is basically the standard degenerate four-wave mixing (DFWM) scheme, consisting of two counterpropagating pumps and a probe. However, amplitude and/or phase information are now encoded on the beams. The phase conjugator is placed at the common back focal plane of lenses L1, L2 and L3. The fields at this position are proportional to the Fourier transforms of the inputs at input planes 1, 2 and 3. The phase conjugate signal monitored at the viewing plane is proportional to the convolution or correlation of the inputs under the following conditions. The correlation operation is performed by placing information at input planes 1 and 2 and a point source at plane 3. The convolution of input 2 and 3 is generated if a delta function (spatial) exists at input plane 1.

Preliminary correlation experiments have used $BaTiO_3$ as the phase conjugate medium. These experiments are similar to those reported by White and Yariv.[13] However, in our experiments we are using a specially generated character mask. The characters are shown in Figure 5-2. These characters are chosen for ease evaluation of the two-dimensional cross-correlation function defined as

$$\Phi\alpha\beta(v) = \int\alpha(\mu)\beta(\mu+v)\,d\mu,$$

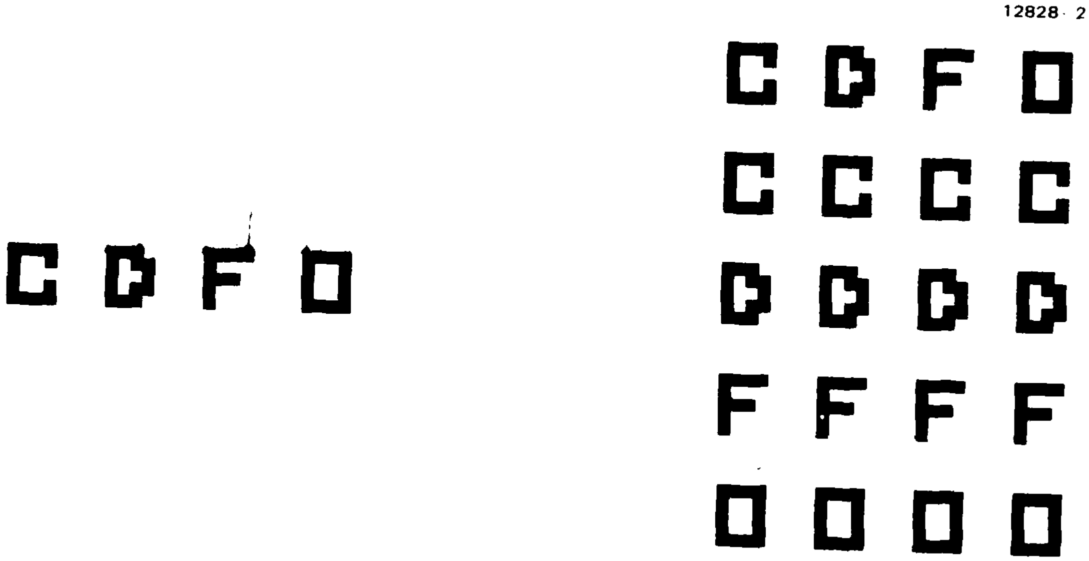

Figure 5-2. Character mask used in 2-D correlation experiment.

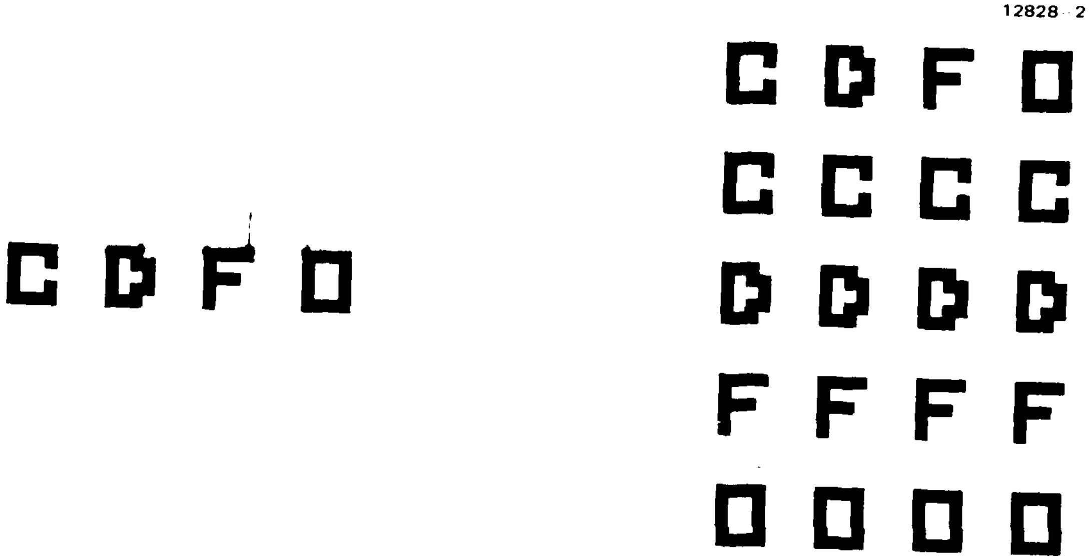

Figure 5-2. Character mask used in 2-D correlation experiment.

where $\mu = (\mu_1, \mu_2)$ are the two-dimensional vector coordinates and $v = (\nu_1, \nu_2)$ are the two-dimensional displacement coordinates. The four characters chosen represent values of high correlation, as between the "C" and the "O", and relatively low values, as between the "F" and the "D". The normalized correlation values defined below are given in Figure 5-3:

$$\tilde{\phi}_{\alpha\beta} = \frac{\phi_{\alpha\beta}}{\sqrt{\phi_{\alpha\alpha}\ \phi_{\beta\beta}}} \quad .$$

A schematic of the experiment is shown in Figure 5-4. A Krypton ion laser (6471A) has an oven-controlled etalon for single longitudinal mode operation. The laser output is controlled and monitored by a scanning Fabry-Perot etalon. Because of orientation, p-polarization of the input beams is required in our experiments. Therefore, a $\lambda/2$ plate and Faraday rotator were used to rotate the plane of polarization of the Krypton laser. The Faraday rotator was also used in conjunction with a polarizer to prevent any return beams from entering the laser and destroying single-mode operation. A beam-expanding telescope and pinhole were used to increase the beam diameter to fully illuminate the character matrix and to spacially filter the beams. Beam splitter 1 reflects a portion of the beam which is used for the forward pump. Beam splitter 2 reflects the probe beam, while the transmitted beam is used as the backward pump. Lenses 1, 2 and 3 have a f=50 cm focal length, with the crystal placed at the Fourier transform plane of these lenses. Each mask is placed a distance f away from the appropriate lens. The mask was ion-beam etched in gold film on glass, and the characters are one millimeter in height. By illuminating one of the characters of mask 2 and the entire matrix of mask 1, the phase conjugate signal will be a matrix. The intensity of each element corresponds to the correlation of the characters illuminated. The phase conjugate signal is directed by beam splitter 3 to a convenient viewing plane.

12828 1

	C	D	F	O
C	1.0	0.815	0.703	0.972
D	0.815	1.0	0.592	0.859
F	0.703	0.592	1.0	0.676
O	0.972	0.859	0.676	1.0

Figure 5-3. Normalized cross-correlation matrix.

12254-1

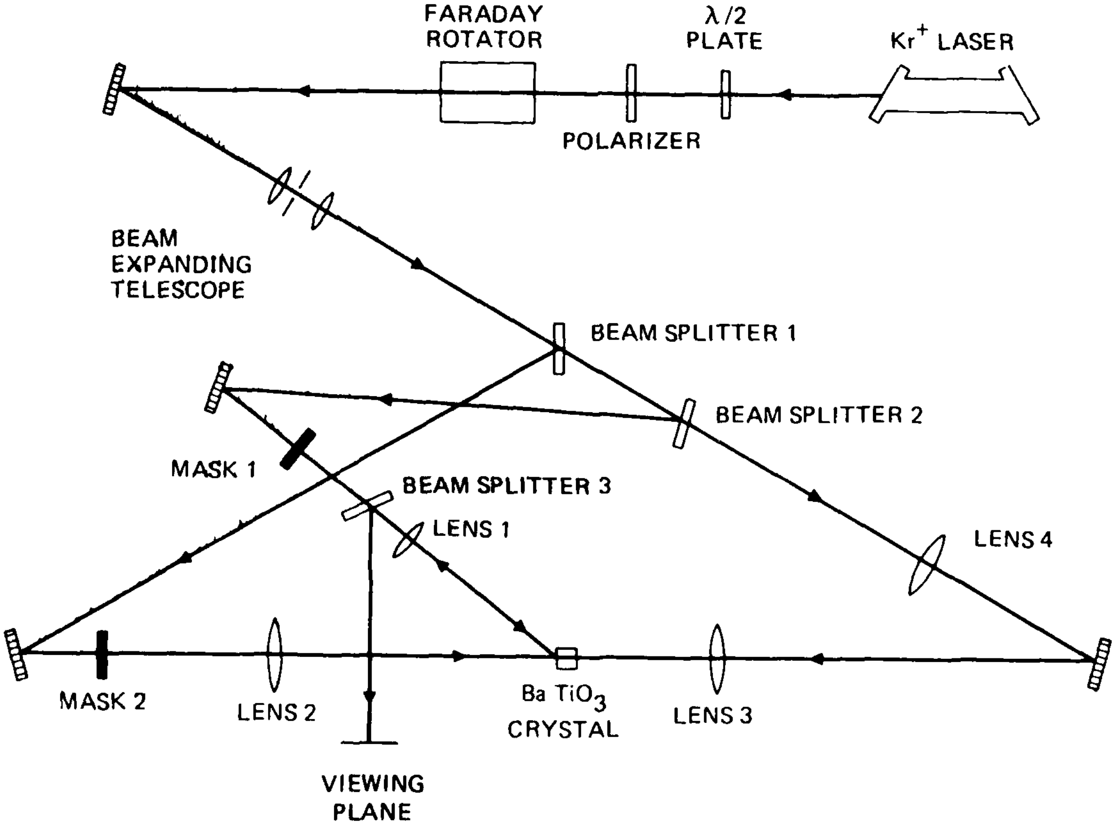

FARADAY ROTATOR
λ/2 PLATE
Kr+ LASER
POLARIZER
BEAM EXPANDING TELESCOPE
BEAM SPLITTER 1
BEAM SPLITTER 2
MASK 1
BEAM SPLITTER 3
LENS 1
LENS 4
MASK 2
LENS 2
Ba TiO3 CRYSTAL
LENS 3
VIEWING PLANE

Figure 5-4. Two-dimensional correlation experiment schematic.

The correlation of a single character and the matrix of characters was successfully demonstrated. However, due to a redirection of the objectives of this contract toward investigating real-time optical correlation further work was not pursued.

B. REAL TIME CORRELATION

This portion of the program was directed toward demonstrating the temporal correlation of signals using four-wave mixing configurations. This signal processing concept was proposed by William Micelli of RADC.

The scheme uses acousto-optic modulators to impose a traveling replica, of a finite time segment, from an input electrical signal onto the transmitted wavefront. By using barium titanate (a photorefractive crystal) as the phase conjugator, the degenerate four-wave mixing (DFWM) signal should be proportional to the time integrated product of the two electrical signals.

The experiments to be described use two acousto-optic modulators to generate the function, $F_1(t) \cdot F_2(t-\tau)$. This is done by using an acousto-optic delay line. The output intensities and frequencies are shown in Figure 5-5 where the diffraction efficiency of the A.O. modulator is α and the incident probe amplitude is A. The resulting outputs are also shown where the upshifted, downshifted or undiffracted beams are taken into a second A.O. modulator, with diffraction efficiency, β. It is seen that there are several terms proportional to $F_1(t) \cdot F_2(t)$. However, it is important to note that in order for interference to occur in the phase conjugator (which is $BaTiO_3$) the beams with the correct temporal information must be at the same frequency. This is because of the slow response time of the $BaTiO_3$. If two beams at different frequencies interfere, a moving grating results. If the material cannot respond to this motion, then the grating is washed out. This is the case in $BaTiO_3$, since its response

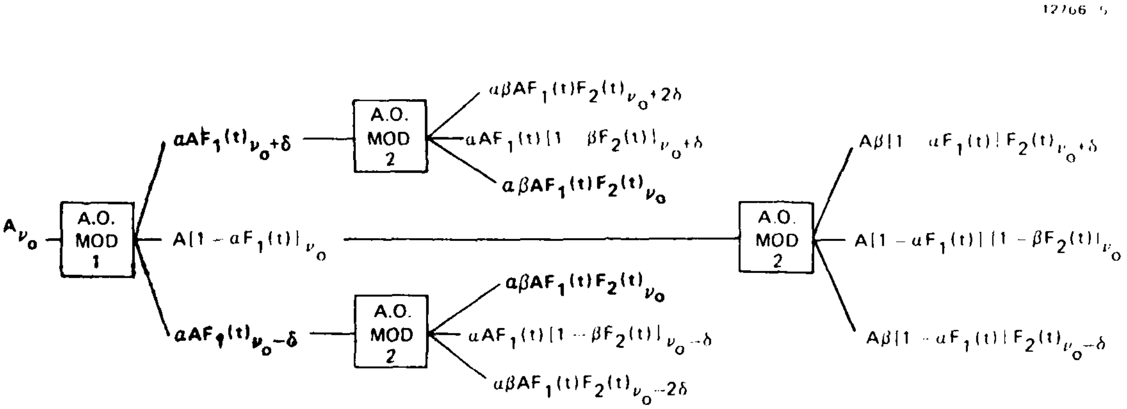
12766-5
A_{ν_0}
A.O. MOD 1
$\alpha A F_1(t)_{\nu_0+\delta}$
$A[1-\alpha F_1(t)]_{\nu_0}$
$\alpha A F_1(t)_{\nu_0-\delta}$
A.O. MOD 2
$\alpha\beta A F_1(t) F_2(t)_{\nu_0+2\delta}$
$\alpha A F_1(t)[1-\beta F_2(t)]_{\nu_0+\delta}$
$\alpha\beta A F_1(t) F_2(t)_{\nu_0}$
A.O. MOD 2
$\alpha\beta A F_1(t) F_2(t)_{\nu_0}$
$\alpha A F_1(t)[1-\beta F_2(t)]_{\nu_0-\delta}$
$\alpha\beta A F_1(t) F_2(t)_{\nu_0-2\delta}$
A.O. MOD 2
$A\beta[1-\alpha F_1(t)] F_2(t)_{\nu_0+\delta}$
$A[1-\alpha F_1(t)][1-\beta F_2(t)]_{\nu_0}$
$A\beta[1-\alpha F_1(t)] F_2(t)_{\nu_0-\delta}$

Figure 5-5. Relative indensity and frequency of diffracted orders produced by acousto-optic devices

time is a fraction of a second (10 Hz), whereas the frequency difference is 40 MHz. Therefore, in order for useful interference to occur between the pumps and the probe in the phase conjugator, they must be at the same frequency. The diffracted orders are shifted from the zero order by $\pm f_c$, so care must be taken to utilize the correct orders. (See Figure 5-5). If the -1 order from the acousto-optic modulator is used, then the +1 order from the A.O. delay line must be used. Similarly, if the +1 order from the A.O. modulator is used, then the -1 order from the A.O. delay line is used. Therefore, only the bold face terms in Figure 5-5 are useful in these experiments.

The first experiment performed using this A.O. cell configuration was optical multiplication of two signals. A schematic of the experiment is given in Figure 5-6. The laser source is a Krypton ion laser (6471Å). A beam compacting telescope and pinhole were used to reduce the beam size inside the acousto-optic modulator and to spatially filter the beam. Beam splitter 1 transmits the backward pump beam, while the reflected beam enters the A.O. modulator. Both the A.O. modulator and A.O. delay line are driven in phase at 40 MHz. The schematic of the electronics is shown in Figure 5-7

A master oscillator generates the 40 MHz carrier frequency for both A.O. devices. The output is split into two branches by a power divider. The signals $F_1(t)$ and $F_2(t)$ are impressed on the carrier frequency by an electronic attenuator. The modulated signal is then amplified by power amplifiers to a level sufficient to drive the A.O. devices, typically 4W.

For phase matching, the functions $F_1(t)$ and $_2(t)$ are constants. When $F_1(t)$ is non-zero, diffracted orders exist and the intensity is proportional to the magnitude of F_1.

12300-2 R1

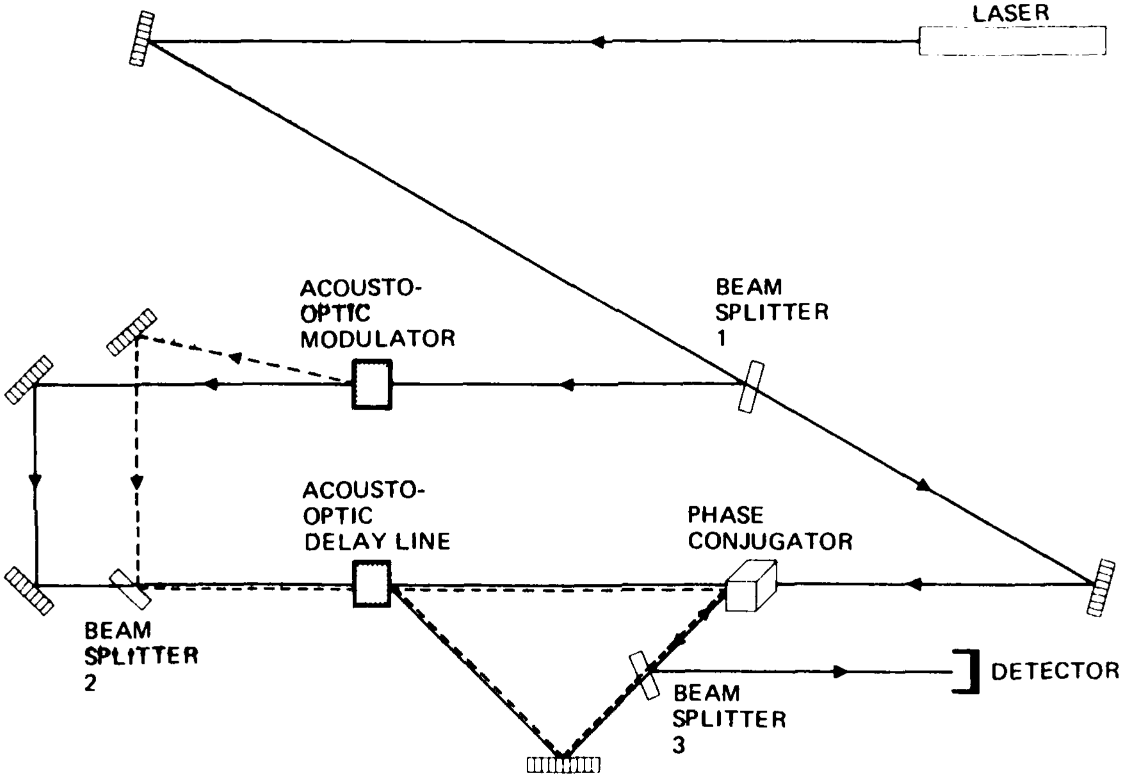
LASER
ACOUSTO-
OPTIC
MODULATOR
BEAM
SPLITTER
1
ACOUSTO-
OPTIC
DELAY LINE
PHASE
CONJUGATOR
BEAM
SPLITTER
2
DETECTOR
BEAM
SPLITTER
3

Figure 5-6. Optical multiplication experiment schematic.

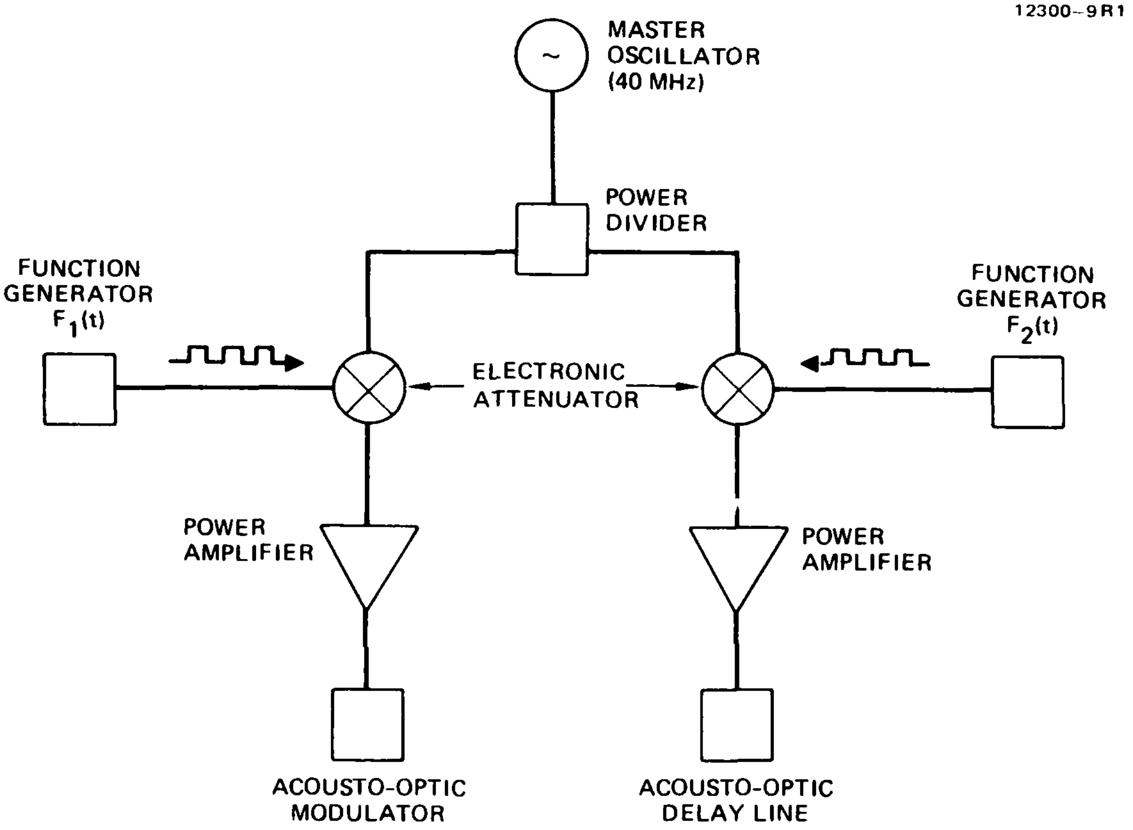
12300-9R1
MASTER OSCILLATOR (40 MHz)
POWER DIVIDER
FUNCTION GENERATOR $F_1(t)$
FUNCTION GENERATOR $F_2(t)$
ELECTRONIC ATTENUATOR
POWER AMPLIFIER
POWER AMPLIFIER
ACOUSTO-OPTIC MODULATOR
ACOUSTO-OPTIC DELAY LINE

Figure 5-7. Electronics used to drive acousto-optic devices block diagram.

Returning to Figure 5-6, the diffracted and undiffracted beams are recombined (for the purpose of heterodyne detection to increase dynamic range) using beam splitter 2. The function $F_2(t)$ is impressed on the carrier frequency of the delay line. For these experiments the beam was not expanded to fill the delay line. The diffracted and undiffracted orders from the A.O. delay line are interfered at the phase conjugator. The resulting fringe patterns (shown in Figure 5-8) were made by replacing the phase conjugator with a microscope objective and focusing the magnified image on a film plane with F_1 and F_2 constant. To obtain the magnification of the fringe pattern, F_1 was set equal to zero, with F_2 equal to a constant; a resolution chart was placed in front of the microscope objective. Keeping the objective in place, the chart was then moved until its image was in focus at the film plane. By measuring the spacing on film between known bar patterns of the resolution chart, the exact magnification of the system could be determined. The measured values of fringe spacing, D, agreed well with the theoretical values predicted by $D = \lambda/(2 \sin\theta/2)$, where θ is the angle between the pump and probe beams.

In Figure 5-6, the phase conjugate signal retraces the probe path and is reflected by beam splitter 3 into a photomultiplier. The resultant signal is recorded by a chart recorder. Typical data is shown in Figures 5-9A and 5-9B. In Figure 5-9A the function $F_1(t)$ is a sawtooth function of .01 Hz. $F_2(t)$ is a square wave of 0.9 Hz. Notice that the resultant signal waveform is qualitatively similar to the product of F_1 and F_2, modified by the time response of the phase conjugator, $BaTiO_3$. In Figure 5-9B, $F_1(t)$ is a 0.05 Hz square wave and $F_2(t)$ is a 0.5 Hz square wave. This data clearly shows the multiplication of $f_1(t)$ and $f_2(t)$.

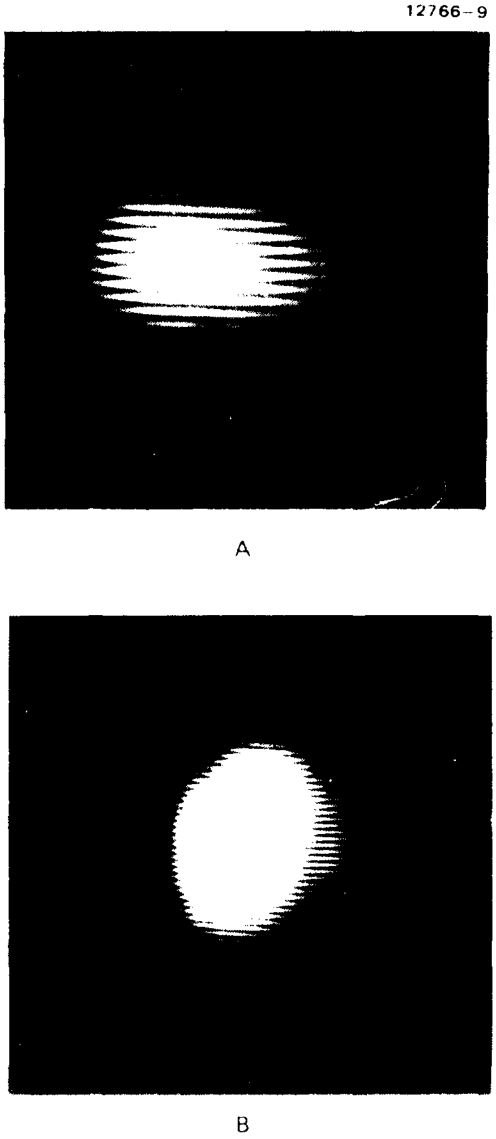

Figure 5-8.
Fringe pattern created by pump beam and probe beam at position of conjugator.

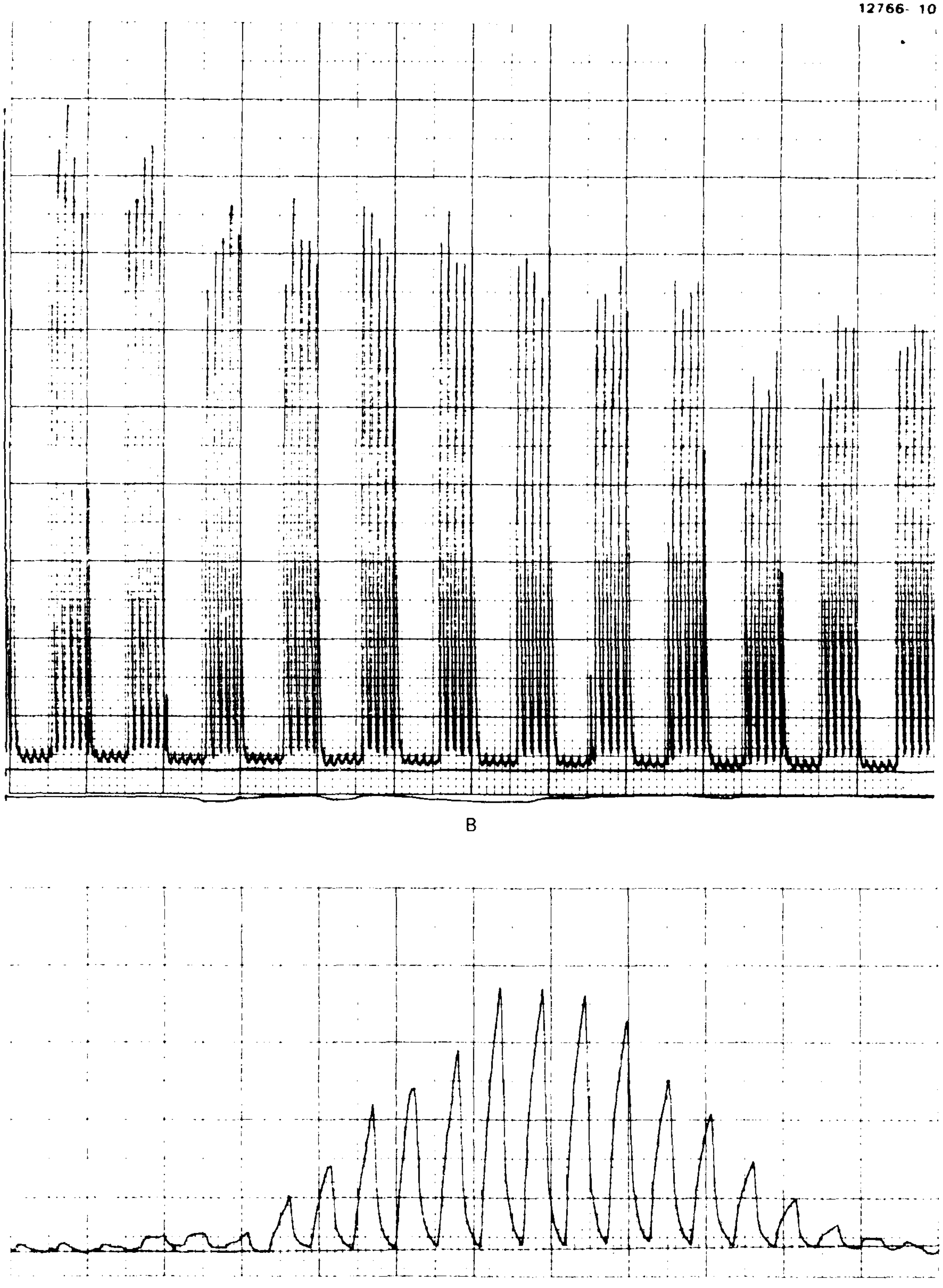

Figure 5-9. Data for optical multiplication of the function, $F_1(t)$ and $F_2(t)$. A. $F_1(t)$ = 0.01 Hz sawtooth, $F_2(t)$ = 0.9 Hz square wave. B. $F_1(t)$ = 0.5 Hz square wve, $F_2(t)$ = 0.05 Hz square wave.

Observation of this data indicates a slowly varying peak amplitude modulation due to instabilities in the optical mounts. Because $BaTiO_3$ has a long time response (~400 msec), the degenerate four-wave mixing process is exactly analogous to making a conventional hologram. The write beam and reference beam interfere in the phase conjugate material, forming a grating which diffracts a portion of the read beam. This diffracted energy is the four-wave mixing signal. In holography it is necessary for the relative path length differences between the write and reference beams to be constant during the exposure. If there are variations on the order of a half wavelength the hologram loses contrast and is washed out. Therefore, it is important in holography or DFWM using photorefractive crystals for the optical system to be mechanically and thermally stable for extended periods of time (minutes). We have undergone major modifications to our optics mounting system to meet these requirements. A Michelson interferometer was used to quantify the degree of stability for various mounting schemes. A detector at the output of the interferometer monitors an area much less than one fringe spacing. The output is then a direct measure of fringe motion which is proportional to the stability of the optical system. Data is shown in Figure 5-10 which charts the detector output versus time for three different mounting techniques. There are typically ten or more mounts in an experimental layout. Therefore, any noise contributed by a single mount can be amplified because of long optical paths and the contribution from additional mounts. The stability problem was initially so severe that the phase conjugate signal generated by cw pumps and probe was modulated by one hundred per cent. This modulation was because the motion caused the grating to be continually erased and rewritten. The new mounting technique of mechanically rigid, massive post holders on a magnetic base has significantly reduced the problem. The table is presently suspended by frictionless air pistons to minimize vibration.

12766-11

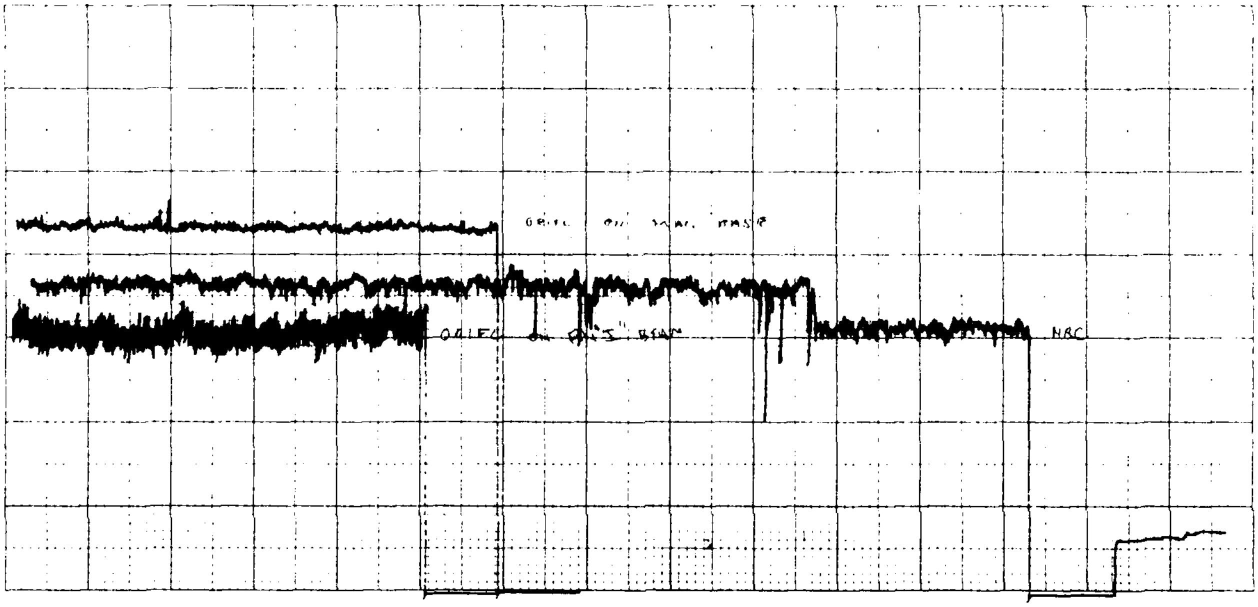

Figure 5-10. Stability of various mounting techniques.

A schematic of an experiment for performing the correlation of the functions $F_1(t)$ and $F_2(t)$ using acousto-optic devices and phase conjugation is shown in Figure 5-11. The function, F_1 (t), is impressed on the carrier frequency of the acousto-optic modulator. When $F_1(t)$ is null, only the undiffracted order is present, as shown in dashed lines. When $F_1(t)$ is non-zero, a diffracted order exists and is proportional to the magnitude of F_1. A beam expanding telescope using cylindrical optics is used to expand the beam to "fill" the acousto-optic delay line. The function, $F_2(t)$ is impressed onto the carrier frequency of the delay line. The output from the delay line is given by the product of the input, $F_1(t)$, times $F_2(t-x/v)$, where x is the position measured perpendicular to the beam propagation direction and v is the acoustic velocity.

A lens is used to demagnify and image the end of the A.O. delay line into the phase conjugator. Although the operation of this system is not completely understood at this time, it appears that the conjugator ($BaTiO_3$) performs as a large array of coherent detectors integrating the complete spatial pattern imposed on the A.O. delay line. Furthermore, because of the long time response of $BaTiO_3$ it also integrates the incoming probe signal in time. The phase conjugate signal which is generated retraces the probe path to beam splitter 3, where a portion is deflected into a photomultiplier, giving a signal proportional to the correlation of $F_1(t)$ and $F_2(t)$.

The main difference between this scheme and the multiplication experiment is that the acousto optic modulators are only in the probe path, whereas before, they were in both the forward pump and probe paths. This new configuration has the advantage that the probe beam is only modulated proportional $F_1(t) \cdot F_2(t-\frac{x}{v})$ in intensity, eliminating any cross terms (See Figure 5-5)

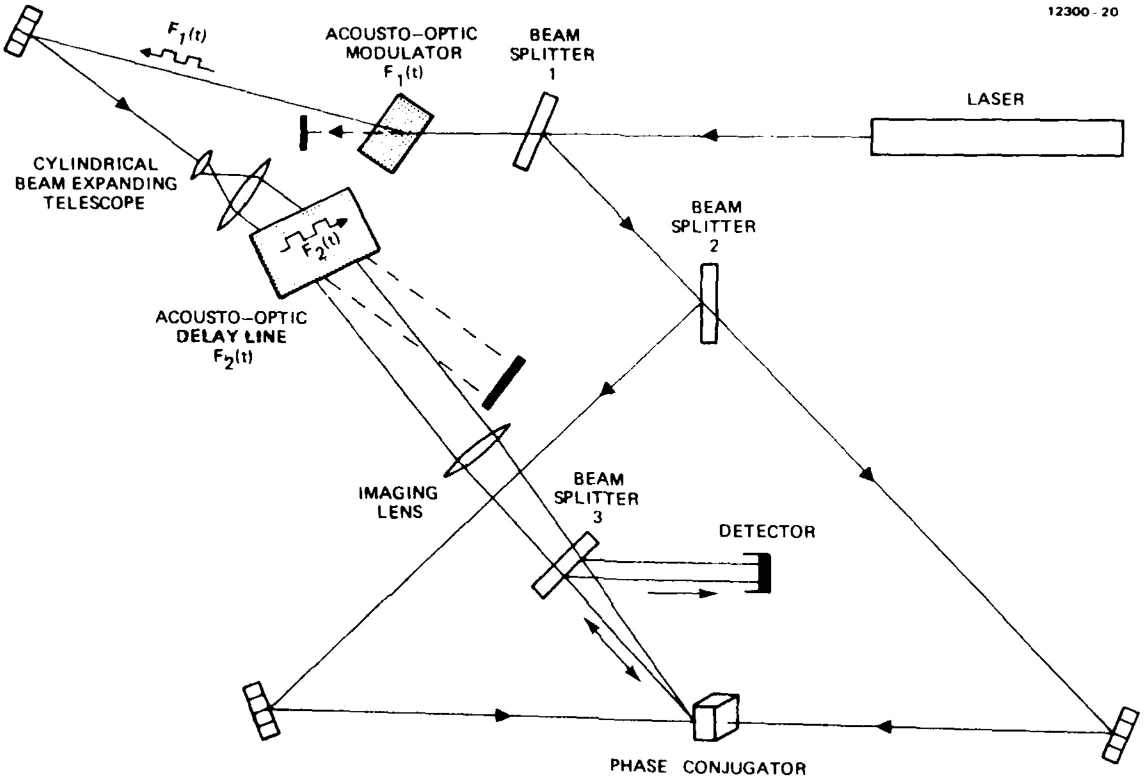
12300-20
$F_1(t)$
ACOUSTO-OPTIC MODULATOR $F_1(t)$
BEAM SPLITTER 1
LASER
CYLINDRICAL BEAM EXPANDING TELESCOPE
$F_2(t)$
BEAM SPLITTER 2
ACOUSTO-OPTIC DELAY LINE $F_2(t)$
IMAGING LENS
BEAM SPLITTER 3
DETECTOR
PHASE CONJUGATOR

Figure 5-11. Real time correlation experiment schematic.

For these experiments, a single longitudinal mode argon ion laser (5145Å) was used. A beam compacting telescope and pinhole were used to reduce the beam size inside the acousto-optic modulator and to spatially filter the beam. The function, $F_1(t)$, is impressed on the carrier frequency (40 MHz) of the acousto-optic modulator. A beam expanding telescope using cylindrical optics is used to expand the beam to "fill" the acousto-optic delay line. The function, $F_2(t)$, is impressed onto the carrier frequency, F_c(40 MHz), of the delay line. Both the A.O. modulator and A.O. delay line carrier frequency are adjusted to be in phase. The output from the A.O. delay line is the product of $F_1(t)$ and $F_2(t-x/v)$. In this experiment a cylindrical beam compaction telescope was used to reduce the probe size smaller than the pump beams in the interaction region of the crystal. Typical data from these experiments is shown for auto-correlation in Figure 5-12. The top trace in Figure 5-12A is the waveform applied to the A.O. modulator, while the lower trace in 5-12A is the waveform applied to the optical delay line. Only the envelope ($f \approx 70$ hz) of the 40 Mhz carrier frequency is visible. Figure 5-12B is the corresponding degenerate four-wave mixing signal. This data does not appear to be consistent with a correlation, although due to time limitations a complete interpretation has not been made.

It is important to recognize that these are the first experimental results of this type and an additional amount of analysis and experimentation are required before a complete understanding can be achieved.

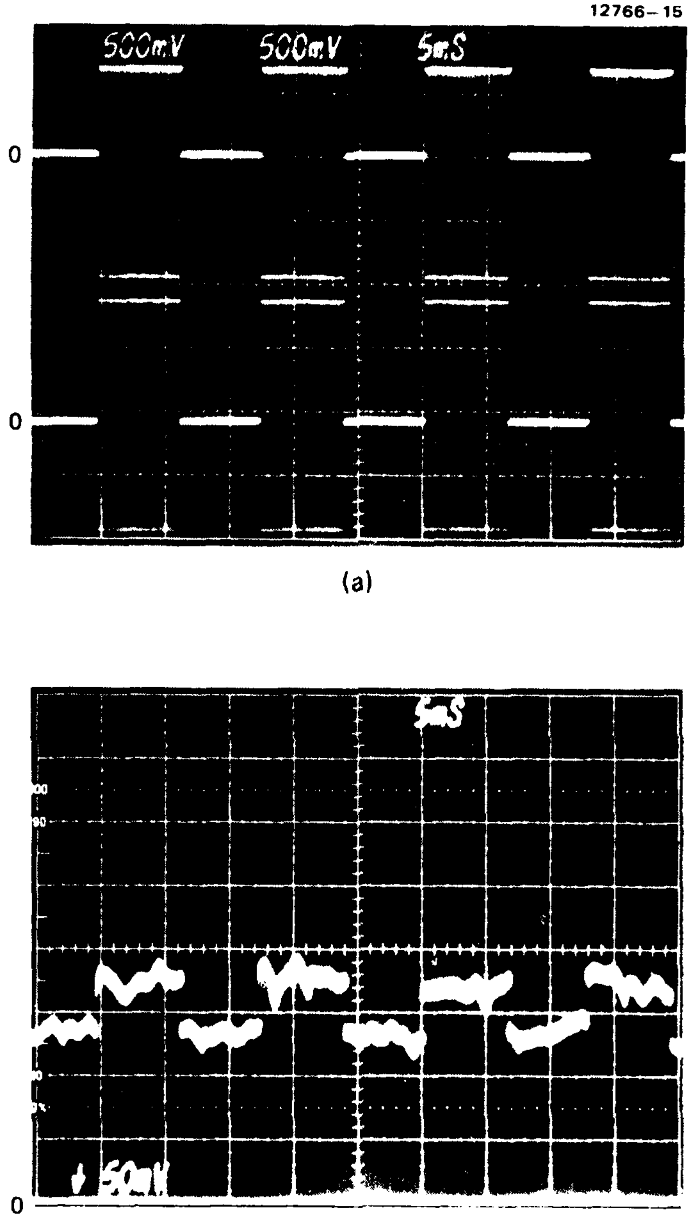

(a)

(b)

Figure 5-12. Real time auto correlation data.
(a) $F_1(t)$ waveform applied to acousto-optic modulator lower trace, $F_2(t)$ waveform applied to acousto-optic delay time upper trace.
(b) Resultant phase conjugator signal.

SECTION 6

CONCLUSIONS AND RECOMMENDATIONS

We have demonstrated that phase conjugate optics is a viable approach for information processing and image transmission applications. The particular phase conjugation interaction which we have found useful is degenerate four-wave mixing. Among the materials and mechanisms available for DFWM, photorefractive materials appear most promising. These materials have high efficiency and spatial resolution at cw power levels. The response time in some cases is slow, but our analysis indicates that improved control of dopant valence state and concentration should lead to a significant increase in speed.

We have demonstrated that four-wave mixing can be used to transmit images in multimode fibers. In our experiments, the phase-conjugate image was re-transmitted through the same fiber, yielding a spatial resolution of 15 lines/mm over a 1.75 M length. The goals of any future effort in this area would be to use improved collection optics to increase the spatial resolution, and to use a separate identical fiber allowing for forward transmission of the image.

We have utilized the ability of phase conjugation to perform the multiplication of two or three input signals and have demonstrated optical correlation between various two-dimensional characters. In addition, we have investigated the real-time correlation of two electrical signals by first converting the signals to spatially modulated optical waves which interact via DFWM in $BaTiO_3$. This unique experimental technique allows parallel processing using two input signals at rates which are not limited by the response time of the photorefractive crystal. It is recommended that further experiments be conducted in this area to increase the understanding of this promising new technology.

ACKNOWLEDGEMENTS

We would like to acknowledge valuable discussions with A. Yariv, J. Lam, R. Hellwarth, G. Valley, M. Sparks, W. Micelli, and G. Burdge.

REFERENCES

1. J. Feinberg, D. Heiman, A.R. Tanguay, Jr., and R.W. Hellwarth, J. Appl. Phys. 51, 1297 (1980).
2. N.V. Kukhtarev, V.B. Markov, S.G. Odulov, M.S. Soskin and V.L. Vinetskii, Ferroelectrics 22, 949 (1979).
3. N.V. Kukhtarev, Sov. Tech. Phys. Lett. 2, 438 (1976).
4. M. Peltier and F. Micheron, J. Appl. Phys. 48, 3683 (1977).
5. B. Fischer, M. Cronin-Golomb, J.O. White and A. Yariv, Opt. Lett. 6, 519 (1981).
6. M. Cronin-Golomb, J.O. White, B. Fischer and A. Yariv, Opt. Lett. 7, 313 (1982).
7. N.V. Kukhtarev and S. G. Odulov, Proc. SPIE Conf. on Optics and Photonics Applied to Communication and Processing, 213, 2 (1979).
8. J. Feinberg, J. Opt. Soc. Am. 72. 46 (1982).
9. N.V. Kukhtarev, V.B. Markov, S.G. Odulov, M.S. Saskin and V.L. Vinetskii, Ferroelectrics 22, 949 (1979).
10. J.P. Hermann and J. Ducuing, J. Appl. Phys. 45, 5100 (1974).
11. G. Dunning and R. Lind, Conference on Lasers and Electro-Optics, April (1982).
12. A. Yariv, Appl. Phys. Lett. 28, 2 p. 88 (1976).
13. J. White and A. Yariv, Appl. Phys. Lett. 37, p. 5, (1980)
14. M.G. Moharam, T.K. Gaylord, R. Magnusson and L. Young, J. Appl. Phys. 50, 5642 (1979).
15. M.P. Petrov and A.V. Khomenko, Sov. Phys. Solid State, 23, 789 (1981).
16. P. Pellat-Finet, G. Lebreton, Proc. SPIE, 400, 151 (1983).
17. J.P. Huignard and F. Micheron, App. Phys. Lett. 29, 591 (1976).
18. Y. Shi, D. Psaltis, A. Marrakchi, and A.R. Tanguay, Jr., Appl. Optics 22, 3665 (1983).

APPENDIX A

SECTION 1

INTRODUCTION

The purpose of this study of photorefractive materials is to develop a theory of photorefractivity, with emphasis on simple physical explanations of the results, in order to interpret experimental results, suggest experiments to be performed, identify materials parameters that should be measured, select and rate types of materials and specific material, and seek improved performance. Photorefractivity, which is the change in the refractive index of a material with irradiance, is analogous to photoconductivity, which is the change in the conductivity of a material with irradiance. A related effect, the photovoltaic effect, is the generation of a voltage by irradiance.

This interim report was prepared in order to make the mathematical details of the treatment of photorefractivity available at the earliest possible time and to solicit comments on the analysis. The details of the mathematical treatment of a simple photorefractivity model that we believe contains the essential fractures required to explain photorefractivity in $LiNbO_3$, $KNbO_3$, $BaTiO_3$, and BSO ($Bi_{12}SiO_{20}$) are presented.
The results of the present report will be applied to these materials, and others of current interest in a subsequent report. The emphasis to date has been on lithium niobate ($LiNbO_3$) because there is more information available on this material than on other materials, some of which may be better candidates for the intended applications. This information is useful in establishing the validity of the theory, which will be done to the extent possible before applying the theory as discussed above.

In a subsequent report, the speed and sensitivity of the various materials will be estimated, tables of values of material parameters will be compiled, materials will be compared, and methods of improving the performance will be discussed along with the effects of changing various system parameters. An important feature of the subsequent report will be a table establishing the operating regime for various materials under diverse operating conditions. Table 1 lists the various limits of laser-pulse duration, electron-transport distance, and electron-transport mechanism. Finally, the present results will be related to previous results in the literature.

As an example of improving performance, the most important method for increasing the speed of lithium niobate is to reduce (the opposite of oxidizing) the sample, which increases the ratio of the densities of "filled" (N_{e0}, for Fe^{2+}) to "empty" (N_{+0}, for Fe^{3+}) levels. This ratio N_{e0}/N_{+0}, not the individual values of N_{e0}, determines the writing- and erasing-speed (for fairly wide ranges of values of N_{e0} and N_{+0}), as seen in the expression for the dielectric-relaxation frequency in Equation 3.7.

The dielectric-relaxation frequency determines the write- and erase-times. (Rewriting a new grating during erasure is known to affect the erase time.) There are several characteristic times in the photorefractive effect including the following: the recombination time of electrons and empty optical-donor levels, the chartacteristic time for the irradiance to generate free carriers, the dielectric relaxation frequency, the trapping time, and the thermal freeing time. The time constant that controls the writing and erasing times is the dielectric relaxation frequency for all cases, namely, diffusion-, applied-field-, and photo-voltaic effect-controlled. It is important to use the correct carrier density, which is the carrier density generated by the write-or erase-beams, in the dielectric relaxation frequency. It is assumed for now that the explaration of the difference between write- and erase-times and between erase times for different c-axis directions is that the writing of a "secondary grating" by the erase- and diffracted-beams is correct. This effect will be investigated in a latter report.

Table 1. Operating Conditions and Material Parameters

Laser-Pulse Duration, t	Short-Time $t \ll \tau_{di}$		Steady-State $t \gg \tau_{di}$
Electron-Transport Distance, Λ	Short-Transport $\Lambda k_g \ll 1$		Long-Transport $\Lambda k_g \gg 1$
Electron-Transport Mechanism	Diffusion	Applied Field	Photovoltaic Effect

The dielectric frequency given by Equation 3.7, the result for the space charge electric field E that gives rise to the grating, and the relation for the grating efficiency for a given E determine the performance of the photorefractive material. This grating electric field is not to be confused with the electric field of the optical beams. The response time, which is the read-or write-time in the absence of writing a secondary grating during erasure is independent of the grating wave vector k_g and diffusion distance Λ. By contrast, the electric field E depends on Λ and k_g in general.

The photorefractive effect is as follows: Illuminating a material with light generates free carriers, which are assumed to be conduction electrons for simplicity in the present treatement. Holes can contribute to the photorefractive effect in general, but are often negligible. The conduction electrons are assumed to come from such impurity levels in the electronic band gap as Fe^{2+} levels in $LiNbO_3$, but could, in general, come from direct exitation of electrons across the gap, by one- or two-photon absorption, for example. These impurity levels will be called optical-donor levels. The electrons drift, if they experience an electric field or diffuse to a new location in the crystal where they recombine with empty optical-donor levels. The space-charge electric field generated between the electrons in their new positions and the empty, positively charged optical-donor levels which remain in their original positions causes the refractive index to change by the electro-optic effect.

In addition to drift in an externally applied dc field and diffusion, the photovoltaic effect can contribute to the photoinduced electric field E. The components of E resulting from diffusion, E_d, drift in the net electric field ($E + E_{app}$, where E_{app} is an externally applied field assumed to be spatially constant), E_{dr}, and the photovoltaic field, E_p,

$$E = E_d + E_{dr} + E_p$$

are discussed below. A typical value of E is 10^4 V/cm. The resulting change in the refractive index, which is called the grating index, is

$$n_g = \frac{1}{2}\ n_r^{\ 3}\ rE, \qquad \underline{(1.1)}$$

where n_r is the refractive index and r is the appropriate linear electro-optic coefficient, having a typical value of 10^{-8} cm/V, which gives
$n_g \cong 0.5\ (2.3)^3\ 10^{-8}\ 10^4 = 6 \times 10^{-4}$

In such optical processing as four-wave mixing used for phase conjugation, the irradiance changes from one position to another in the crystal. For example, the beat patterns of two overlapping beams causes a periodic irradiance. To be concrete, we assume a sinusoidal irradiance distribution for writing a grating

$$I = \langle I \rangle\ (1 + M \cos k_g z) \qquad (1.2)$$

where < > denotes the spatial average

$$\langle I \rangle = \lim_{\ell \to \infty} \int_0^{\ell} dz I \qquad (1.3)$$

and

$$k_g = 4\pi\ n_r \sin\theta/\lambda, \qquad (1.4)$$

with 2θ the full angle in the material between the direction of propagation of the two beams, λ is the wavelength of the light in vacuum, and λ/n_r is the wavelength of the light in the material.

The electric field and the resulting index of refraction n_g have a spatial frequency component at the grating wavelength k_g. This index grating can diffract an incoming light beam with efficiency[1] (for a thick grating)

AD-A141 960   PHASE CONJUGATE OPTICS(U) HUGHES RESEARCH LABS MALIBU   2/3
CA G J DUNNING ET AL. FEB 84 RADC-TR-84-18
F19628-80-C-0185

UNCLASSIFIED   F/G 20/6   NL

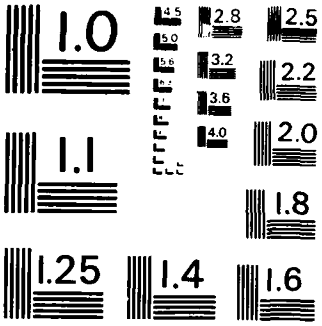
1.0
4.5
5.0
5.6
2.8
3.2
3.6
4.0
2.5
2.2
2.0
1.1
1.8
1.25
1.4
1.6

MICROCOPY RESOLUTION TEST CHART
NATIONAL BUREAU OF STANDARDS-1963-A

$$\eta = e^{-\alpha d/\cos\theta} \sin^2 \frac{\pi n_r n_g d}{2\lambda \cos\theta}, \qquad \underline{(1.5)}$$

where α is the optical absorption coefficient, d is the thickness of the sample, 2θ is the full angle between the two writing beams, n_r is the index of refraction of the material, n_g is the change in the index resulting from the photorefractive effect, and λ is the vacuum wavelength of the writing beams.

There is general agreement in the literature that this description of the photorefractive effect is correct. However, there is disagreement as to such details of the model as which electron transport mechanisms — drift, diffusion, or asymmetric photogeneration of electrons (photovoltaic effect) — is operative in a given material and why the grating efficiency increases or decreases with increasing pulse duration t_p for a given energy density It_p, rather than remaining constant as predicted by early theories.

The model is discussed in Section 2. In order to make the first analysis as simple as possible, the first case considered (see Section 3) is that of an applied field only. Diffusion, the photovoltaic effect, depletion, and saturation are neglected. The case of diffusion only and of photovoltaic only are consider in Sections 4 and 5 respectively in order to determine the defects of these two transport processes acting individually. Depletion and saturation are considered in Section 6. The steady-state grating electric field with an applied electric field, diffusion, and the photoelectric field included is derived in Section 7. The results of Kukhtarev and coworkers[2] and of Amodei[3] are related to the present work and discrepancies between the three sets of results are resolved in Section 8. Simple pedantic models of the photovoltaic effect and of dielectric relaxation are given in Sections 9 and 10. A summary of the mathematical results are given in Section 11. The Appendix contains a list of symbols and typical values of parameters for lithium niobate.

Electrostatic units (esu) are used in the equations. Numerical results are given in both electrostatic units and rationalized mks units. Conversion factors are listed in the Appendix for the convenience of the reader.

Important results are denoted by underscored equation numbers and used in the summary (Section 11).

SECTION 2

MODEL OF PHOTOREFRACTIVITY

The analysis of even the simplest model of photorefractivity is complicated when carried out without approximations because the coupled material's equations and Maxwell's equations are nonlinear, coupled, partial differential equations. In order to develop the physical understanding required for materials-improvement programs and operation-improvement programs, a simple model is discussed first, then the effects of the assumptions made in the simple model are discussed.

The simplest model of photorefractivity is as follows: The material is an insulator with N_D optical levels per cubic centimeter in the electronic bandgap. See Figure 1. The levels are sufficiently deep that they are not thermally excited into the conduction band. The levels are called optical-donor levels because electrons from these levels are photoexcited into the conduction band. The density of the optical-donor levels that are filled with electrons is N_e and the density that are unfilled is N_+. For example, N_e could be the Fe^{2+} density in lithim niobate, N_+ and Fe^{3+} density, and $N_D = N_e + N_+$ the total iron density including both Fe^{2+} and Fe^{3+}. In general, there are many filled levels N_e and many empty levels N_+. The ratio N_e/N_+ can be varied by oxidizing or reducing the sample or by doping with compensating impurities. In order to make the crystal have charge neutrality. There must be negative impurities or imperfections present to compensate for the positive charges of the iron. The density of these levels that compensate for the extra positive charge of the Fe^{3+} is equal to the value N_{+0} of N_+ before the irradiance is turned on. Subscript zeros denote the values of parameters at $t = 0$, i.e., the time at which the irrandiance is turned on.

Holes are neglected for simplicity. Electrons are generated from the filled optical-donor levels to the conduction band by the irradience and recombine with empty optical-donor levels. Trapping is neglected in this first model. We used the common photoconductivity terminology that electrons in traps can be thermally re-excited into the conduction band. Thus, the capture of electrons by the empty optical-donor levels is called recombination, rather than trapping. This recombination into the optical-donor levels is not to be confused with recombination of holes and electrons across the gap.

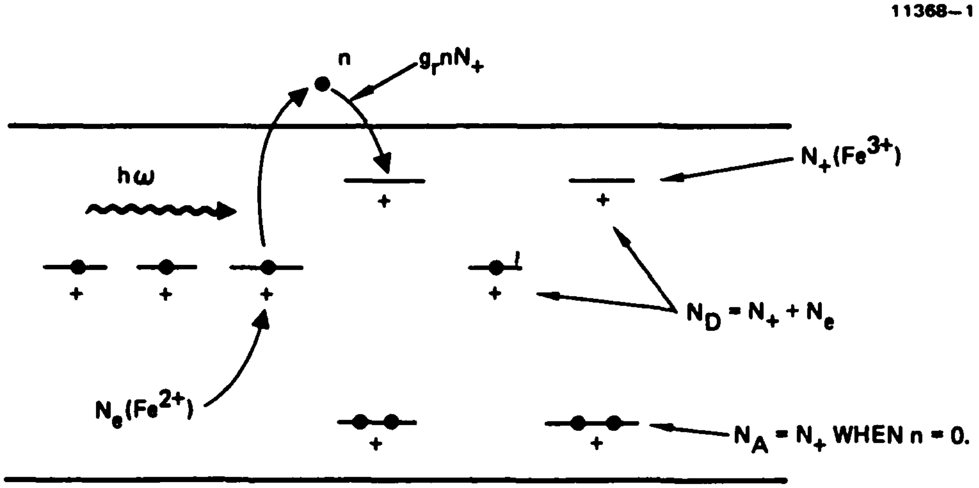
11368-1
n
$g_r n N_+$
$N_+(Fe^{3+})$
hω
$N_D = N_+ + N_e$
$N_e(Fe^{2+})$
$N_A = N_+$ WHEN n = 0.

Figure 1. Schematic illustration of the photorefractivity model shown the various electronic levels in the bandgap.

Saturation and depletion of the optical-donor levels are neglected when possible. However, they must be included in the analysis of the steady state because the correct steady state is not attained in general when saturation and depletion are neglected.

The simple model is believed to be sufficient to explain the performance of iron-doped lithium niobate, and it may be sufficient for the other materials of current interest. Extensions of the model and the applicability to other materials will be considered in subsequent studies and reports.

The number of electrons per cubic centimeter generated by the light is equal to the number of photons per cubic centimeter absorbed, which is equal to the absorbed energy per cubic centimeter, αI, (where α is the optical absorption coefficient) divided by the photon energy ħω:

$$(\partial n/\partial t)_I = (\partial N_+/\partial E)_I = \alpha I/\hbar\omega \quad .$$

It was assumed that one free electron is generated for every absorbed photon. This generation rate can be written in several convenient forms as follows:

$$\alpha I/\hbar\omega = \sigma_D N_e/\hbar\omega = \gamma_I N_e = \langle\gamma_I\rangle\, N_e(1 + M\cos k_g z) \quad , \qquad (2.1)$$

where Equation 1.2 was used for I and

$$\alpha = \sigma_D N_e \quad , \qquad (2.2)$$

$$\gamma_I = \sigma_D I/\hbar\omega \quad , \qquad \langle\gamma_I\rangle = \sigma_D \langle I\rangle/\hbar\omega \qquad (2.3)$$

where σ_D is the optical absorption cross section of the optical donor levels.

The change in the electron concentration resulting from movement of the electrons away from the generation region (and from the motion of the electrons in general) is described by the charge continuity equation:

$$\partial\rho/\partial t = \nabla \cdot \underset{\sim}{J} = -dJ/dz \tag{2.4}$$

where the charge density is

$$\rho = e(N_{+} - N_{+0} - n) = e(N_{+\Delta} - n) \tag{2.5}$$

where $e = |e|$, the absolute magnitude of the electron charge; $N_{+\Delta} \equiv N_{+} - N_{+0}$; and J is the electrical current (-e times the net rate at which electrons cross a unit area of surface). Substituting Equation 2.5 into Equation 2.4 gives the first central equation — Equation 2.8 below. The recombination rate is

$$(\partial n/\partial t)_{recomb} = -v_{th} s N_{+} n$$

where the recombination frequency is

$$\gamma_r = v_{th} s N_{+0} \quad , \tag{2.6}$$

where s is the cross section for the capture of an electron by an empty optical donor level (having density N_{+}), and v_{th} is the average thermal velocity of the electrons, which has the value:

$$v_{th} \cong 10^{7} \text{ cm/sec} \tag{2.7}$$

at room temperature. Combining these contributions gives the basic equations:

$$\partial n/\partial t = \partial N_{+}/\partial t + e^{-1} dJ/dz \tag{2.8}$$

$$\partial N_{+}/\partial t = -\partial N_{e}/\partial t = \gamma_{I} N_{e} - \gamma_{r} n N_{+}/N_{+0} \tag{2.9}$$

$$J = -e\mu n E + eD\partial n/\partial z + pN_{e} I\hat{c} \tag{2.10}$$

$$\partial E/\partial z = 4\pi\hat{\varepsilon}^{-1}\rho \tag{2.11}$$

$$\rho = e(N_{+} - N_{+0} - n) = e(N_{+\Delta} - n) \tag{2.12}$$

$$E = E_{app} + E_{sc} \tag{2.13}$$

where D is the diffusion coefficient, ρ is the photovoltaic coefficient, c is the unit vector along the photovoltaic direction, and $e = |e|$. The contributions to the current in Equation 2.10 are as follows: $-e\mu nE \equiv -eV_{drift}n$ is the usual electrical-conductivity current $J = \sigma E$; $eD\partial n/\partial z$ is the diffusion current; and $pN_eI\hat{c}$ is the photovoltaic current, as discussed in Section 9.

These system Equations 2.8 through 2.13 are nonlinear because they contain products N_+n and nE (where E is a function of n and N_+). Thus, their solution is nontrivial, and the complexity of the general results would obscure simple interpretation. The following limiting cases will therefore be considered:

(a) $k_g\Lambda \ll 1$ and $k_g\Lambda \gg 1$

(b) drift, diffusion, and photovoltaic-effect-dominated

(c) short-time limit and steady state,

where Λ is the electron-transport distance, as discussed below.

For all cases, a first approximation which will be relaxed below for special cases, the equations are linearized by neglecting depletion and saturation. Depletion is the reduction in the absorption coefficient α resulting from depletion of the electrons in the optical-donor levels, and saturation is the reduction in the recombination rate γ_r resulting from filling of the recombination levels (which are the empty optical-donor levels N_+ in the present model) with electrons. Depletion is negligible when $N_e \cong N_{e0}$, and saturation is negligible when $N_+ \cong N_{+0}$. To be more specific, define the changes $N_{+\Delta}$ and $N_{e\Delta}$ as

$$N_{+\Delta} \equiv N_+ - N_{+0} \tag{2.14}$$

and

$$N_{e\Delta} \equiv N_e - N_{e0} \quad . \tag{2.15}$$

Since $\partial N_e/\partial t = -\partial N_+/\partial t$ according to Equation 2.9

$$N_{+\Delta} = -N_{e\Delta} \quad , \tag{2.16}$$

Thus, the approximations of negligible depletion and saturation are, respectively,

$$|N_{+\Delta}| << N_{+0} \quad , \tag{2.17}$$

$$|N_{e\Delta}| = |N_{+\Delta}| << N_{e0} \quad . \tag{2.18}$$

For negligible saturation, the optical absorption coefficient $\alpha = \sigma_D N_e$ is constant. Thus,

$$\alpha = \sigma_D N_{e0} \quad , \qquad \text{for negligible depletion.} \tag{2.19}$$

For negligible saturation, the recombination frequency $v_{th} s N_+$ is constant. thus

$$\gamma_r = v_{th} s N_{+0} \quad , \qquad \text{for negligible saturation.} \tag{2-20}$$

SECTION 3

APPLIED-FIELD DOMINATED

In this section, diffusion, the photovoltaic effect, depletion, and saturation are neglected. The electron-drift distance is

$$\Lambda_E = \mu\tau_r E \quad ,$$

where $\tau_r \equiv 1/\gamma_r$ is the recombination time and μE is the drift velocity. The two limits of short drift distance, $k_g\Lambda_{dr} << 1$ and long drift distance $k_g\Lambda_E >> 1$, will be considered.

The steady-state solution of Equation 2.9 with $N_e \cong N_{e0}$ and $N_+ \cong N_{+0}$ is

$$n = (\gamma_I/\gamma_r)N_{e0} = \langle n\rangle\ (1 + M \cos k_g z) \qquad \underline{(3.1)}$$

where

$$\langle n\rangle = (\langle\gamma_I\rangle/\gamma_r)N_{e0} \quad . \qquad \underline{(3.2)}$$

typical value

$$\tau_r = 1/v_{th}sN_{+0} = 0.2\ \text{ns}/c_+(\text{ppm}) = 20\ \text{psec} \qquad (3.3)$$

for $v_{th} = 10^7$ cm/sec (at room temperature), electron-ion cross section for a changed recombination center $s = 10^{-14}$ cm^2, and recombination center density $N_{+0} = 5 \times 10^{17}$ cm^{-3} for a lightly doped sample with concentration $c_+ = N_{+0}/N_{\text{atomic sites}} = 10$ ppm. For heavily doped samples, τ_r is even shorter than the value of 20 psec in Equation 3.3. Thus, for pulse durations and doping concentrations of current interest, $\tau_r << t$ is satisfied throughout most of the pulse duration. Furthermore, n is given by the steady-state value in Equation 3.1, except at very short times which will be neglected here. Physically, for negligible electron drift distance, the electrons are trapped where they are generated. Thus, setting J = 0 in Equation 2.10 as a zeroth-order approximation and solving for n gives an exponential rise to the value in Equation 3.1 with rise time τ_r.

Having calculated n under the zeroth-order approximation, J = 0, this value of n and the nonzero value of $J = -e\mu nE$ in the next-order approximation cause N_+ to continue to change after n has reached its steady state. For short times(i.e., before the space charge field E_{sc} builds up to substantially change the electric field in Equation 2.9 from its original value $E_0 = E_{app}$), Equation 2.10 gives:

$$J \cong J_0 = -e\ \mu m^2\ E_{app} \quad .$$

Substituting this J into Equation 2.4 and integrating over time, with $\rho = \rho_0 = 0$ at t = 0, gives

$$\rho = -e\mu\langle n\rangle E_{app} k_g M\ t \sin k_g z \quad . \qquad (3.4)$$

The space-charge electric field resulting from the charge distribution in Equation 3.4, obtained by integrating Poissons equation

$$\nabla \cdot \underset{\sim}{D} \equiv \varepsilon \partial E/\partial z = 4\ \pi\rho \qquad (3.5)$$

is

$$E_{sc} = \gamma_{di}\ t\ E_{app}\ M \cos k_g z \qquad \underline{(3.6)}$$

where the dielectric relaxation frequency is

$$\gamma_{di} = 4\ \pi\sigma/\varepsilon = 4\ \pi e\mu\langle n\rangle/\varepsilon = 4\ \pi e\mu\sigma_D\langle I\rangle N_{e0}/\varepsilon\hbar\omega v_{th} s N_{+0} \quad . \qquad \underline{(3.7)}$$

One of the important results of the present study is that the response time (the read- and write-time in the absende of writing of a secondary grating) is the dielectric relaxation time $\tau_d = 1/\gamma_{di}$. Consideration of the expression for γ_{di} in Equation 3.7 can lead to estimates of the response time and to suggestions on how to increase the speed, as discussed briefly in Section 1. This electric field is in spatial phase ($E \sim \cos k_g z$) with the irradiance, in agreement with the results obtained below by physical arguments.

It is instructive to rederive this electric-field distribution in Equation 3.5 by physical argument in order to gain intuition. Once the steady state value of n is attained, electrons that are generated at z by the irradiance are trapped at $z + \Lambda_E$ on the average. The trapped-change density $e_{N+\Delta}$ (see Equation 2.12) can therefore be written as the sum of two terms, a positive term from the N_+ at z where an electron is generated and a negative term of equal absolute magnitude but displaced by distance Λ_E, corresponding to the recombination of the electron at $z + \Lambda_E$. In other words, the current causes a buildup of the displaced trapped electrons and a corresponding build up of the positive charges left behind (see Figure 2). Integrating the generation equation $(\partial N_{+}/\partial t)_{gen} = (\partial N_{+\Delta}/\partial t)_{gen} = \gamma_I N_{e0}$ for short times gives

$$(eN_{+\Delta})_{gen} = e\langle\gamma_I\rangle N_{e0} t(1 + M \cos k_g z) \quad . \tag{3.8}$$

The corresponding negative, displaced, recombination term is

$$(eN_{+\Delta})_{rcmb} = -e\langle\gamma_I\rangle N_{e0} t\left[1 + M \cos k_g(z - \Lambda_{dr})\right] \quad . \tag{3.9}$$

Adding these two terms and using the Taylor expansion $\cos k_g(z - \Lambda_E) \equiv \cos k_g z + \Lambda_E k_g \sin k_g z$ gives

$$eN_{+\Delta} = -e\langle\gamma_I\rangle\, k_g \Lambda_E N_{e0} tM \cos k_g z \quad . \tag{3.10}$$

With $\rho \equiv eN_{+\Delta}$ and $\langle n\rangle = (\langle\gamma_I\rangle/\gamma_r)N_{e0}$, Equation 3.10 gives Equation 3.4. The rest of the derivation of the space-charge field resulting in Equation 3.6 is the same as above. The charge resulting from n and the corresponding $N_{+\Delta}$ is easily shown to be given by the ρ in Equation 3.4 times τ_r/t, which is negligible for $t \gg \tau_r$.

As the time increases, the space charge field E_{sc} continues to increase according to Equation 3.6 until it is no longer negligible. Then the approximation $E \equiv E_{app}$ is no longer valid, and Equation 3.5 is no longer valid. The electric field for intermediate times is more difficult to calculate, but the steady-state value is again easy to calculate. In the steady-state, $\partial n/\partial t = 0$ and $\partial N_{+}/\partial t = 0$; thus, Equation 2.8 gives $\partial J/\partial z = 0$, or

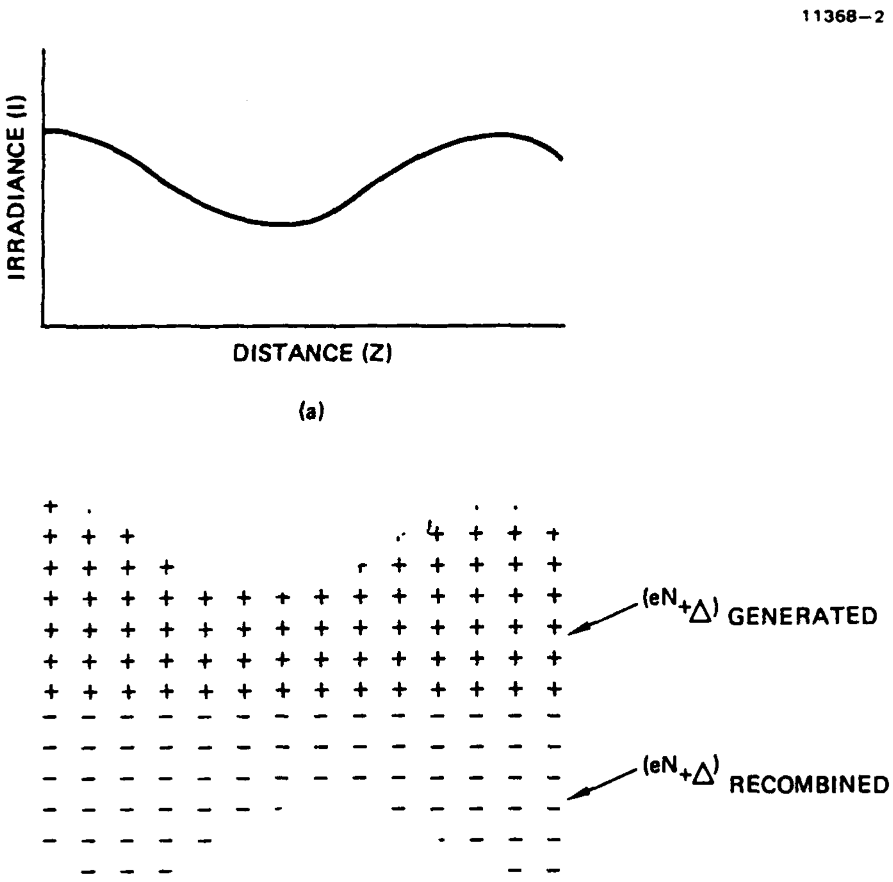
11368–2
IRRADIANCE (I)
DISTANCE (Z)
(a)
$(eN_{+}\Delta)$ GENERATED
$(eN_{+}\Delta)$ RECOMBINED

(b) COMPONENTS OF ρ

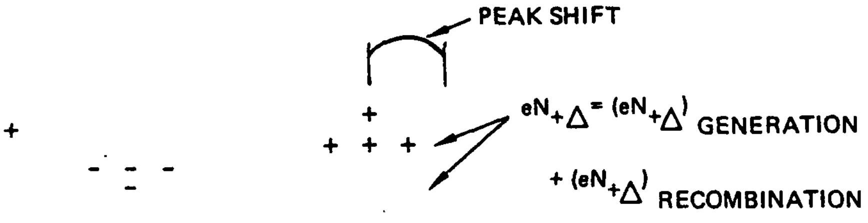
PEAK SHIFT
$eN_{+}\Delta = (eN_{+}\Delta)$ GENERATION
$+ (eN_{+}\Delta)$ RECOMBINATION

(c) TOTAL ρ

Figure 2. Schematic illustration of the positive and negative charge distributions for the case of short diffusion distance ($\Lambda k_g >> 1$) showing the total charge distribution ρ that is spatially phase shifted with respect to the irradiance.

$$J = \text{constant} \equiv J_0 \quad .$$

For the present case of drift only, setting $D = \rho = 0$ in Equation 2.10 gives

$$J = -e\mu nE \quad . \tag{3.11}$$

From Equations 3.10, 3.2, and $J = J_0$,

$$E = -\frac{J_0}{e\mu n} = -\frac{J_0/e\mu \langle n \rangle}{1 + M \cos k_g z} \quad . \tag{3.12}$$

The divergence in E for $M = 1$ at $\cos k_g z = -1$ is unphysical. It arises from the assumption that the transport (drift) length is zero. For nonzero transport length, M is replaced by a number less than unity, as suggested by Amodei[2] and shown by Kukhtarev and coworkers.[3] The field E is not sinusoidal except in the limit of $M << 1$ (where the expansion $(1 + M \cos k_g z)^{-1} \cong 1 + M \cos k_g z$ is valid).

An important feature of the field E (which gives rise to the grating) is obvious when E is expressed in terms of J_0, as in Equation 3.12, although it has not been discussed previously to my knowledge. For open circuit conditions, the steady-state field E vanishes because $J_0 = 0$ (no current for an open circuit). In order to write a steady-state grating (i.e., have $E \neq 0$) in the steady-state with drift alone, there must be an external circuit through which a current can flow. Otherwise, the faces of the crystal are charged by the nonzero current before the steady-state is reached, and the current approaches zero as the time approaches infinity and the charges on the faces approach the value required to make $E_g = -E_{app}$ (i.e., $E = 0$). At intermediate times, the grating is nonzero.

A rough approximation to the full time dependence for this case (of $k_g \Lambda_{dr} << 1$, E_{app} dominated, negligible depletion and saturation, and $J = 0$) is obtained as follows: The charging of the faces of the crystal gives, from Appendix A:

$$E = E_{app} e^{-\gamma_{di} t} \quad , \tag{3.13}$$

where the dielectric relaxation frequency is given by Equation 3.7. Formally replacing $E = E_{app}$ in Equation 3.6 by E in Equation 3.13 and including the spatially constant space-charge field gives

$$E \cong e^{-\gamma_{di} t} (E_{app} + \gamma_{di} t \, E_{app} M \cos k_g z) \quad . \tag{3.14}$$

The maximum of the cos $k_g z$ term occurs at

$$t = \tau_{di} \equiv 1/\gamma_{di} \tag{3.15}$$

and has the value (writing exp (-1) to avoid confusion with the electron charge):

$$E_{mx} = \exp(-1) \, E_{app} M \cos k_g z \quad . \tag{3.16}$$

Since the dielectric relaxation time is the time at which the steady-state is approached, as an approximation to the full time dependence, we multiply the short-time electric field $E_{short-t}$ by $\exp(-\gamma_{di}t)$ and add the result to $f^2 \equiv [1 - \exp(-\gamma_{di}t)]^2$ times the steady-state value E_{ss}

$$E \cong E_{short-t} e^{-\gamma_{di}t} + E_{ss}(1 - e^{-\gamma_{di}t})^2 \quad . \qquad \underline{(3.17)}$$

The square of f was used rather than f to insure that $E \cong E_{short-t}$ at short times. This approximation in Equation 3.17 does not correspond to an exact solution of the systems equation. It is simply an intuitive approximation to the full time dependence. It does give the correct short-time field and steady-state field, and it does develop with time constant $\tau_{di} = 1/\gamma_{di}$. The value of E at intermediate times may not be highly accurate.

With $E_{short-t}$ given by Equation 3.6 and E_{ss} given by Equation 3.12, substituting in Equation 3.17 gives

$$\begin{aligned} E \cong\ & \gamma_{di}t\, e^{-\gamma_{di}t} E_{app} M \cos k_g z \\ & + \left[-(J_0/e\mu\langle n\rangle)/(1 + M \cos k_g z)\right] (1 - e^{-\gamma_{di}t})^2 \quad . \qquad \underline{(3.18)} \end{aligned}$$

Next consider the case of $k_g\Lambda_{dr0} >> 1$, where $\Lambda_{dr0} = \mu\tau_r E_{app}$. Since the electrons then drift a distance long with respect to the grating distance k_g^{-1}, the electron density is approximately constant spatially for $t > \tau_r$. Since the free-electron generation rate $(\partial n/\partial t)_{gen} = \gamma_I N_e$ and recombination rate $(\partial n/\partial t)_{rcmb} = \gamma_r n$ are the same as for the case of $k_g\Lambda_{dr} << 1$, the value of this constant n is just the average value of n from Equation 3.1

$$n \cong \langle n\rangle = (\langle\gamma_I\rangle/\gamma_r)N_{e0} \quad . \tag{3.19}$$

The recombination then occurs evenly over all z (rather than at a short distance from the generation region as was the case for $k_g\Lambda_{dr} << 1$). Figure 2 (for $k_g\Lambda_{dr} << 1$) is then replaced by Figure 3 for the case of $k_g\Lambda_{dr0} >> 1$), and the second term in Equation 3.9 is replaced by zero, corresponding to spreading the charge $eN_{+\Delta c} \cos k_g(z - \Lambda_{dr})$ evenly throughout the crystal. The resulting value of $eN_{+\Delta} = (eN_{+\Delta})_{gen} + (eN_{+\Delta})_{rcmb}$ from Equation 3.8 and the modified Equation 3.9 is

$$eN_{+0} = e\langle\gamma_I\rangle\, N_{e0}Mt \cos k_g z \quad . \tag{3.20}$$

With $\rho \cong eN_{+0}$ and Equation 3.5, this gives

$$E_{sc} = 4\pi e\langle\gamma_I\rangle\, N_{e0}(k_g\varepsilon)tM \sin k_g z \tag{3.21}$$

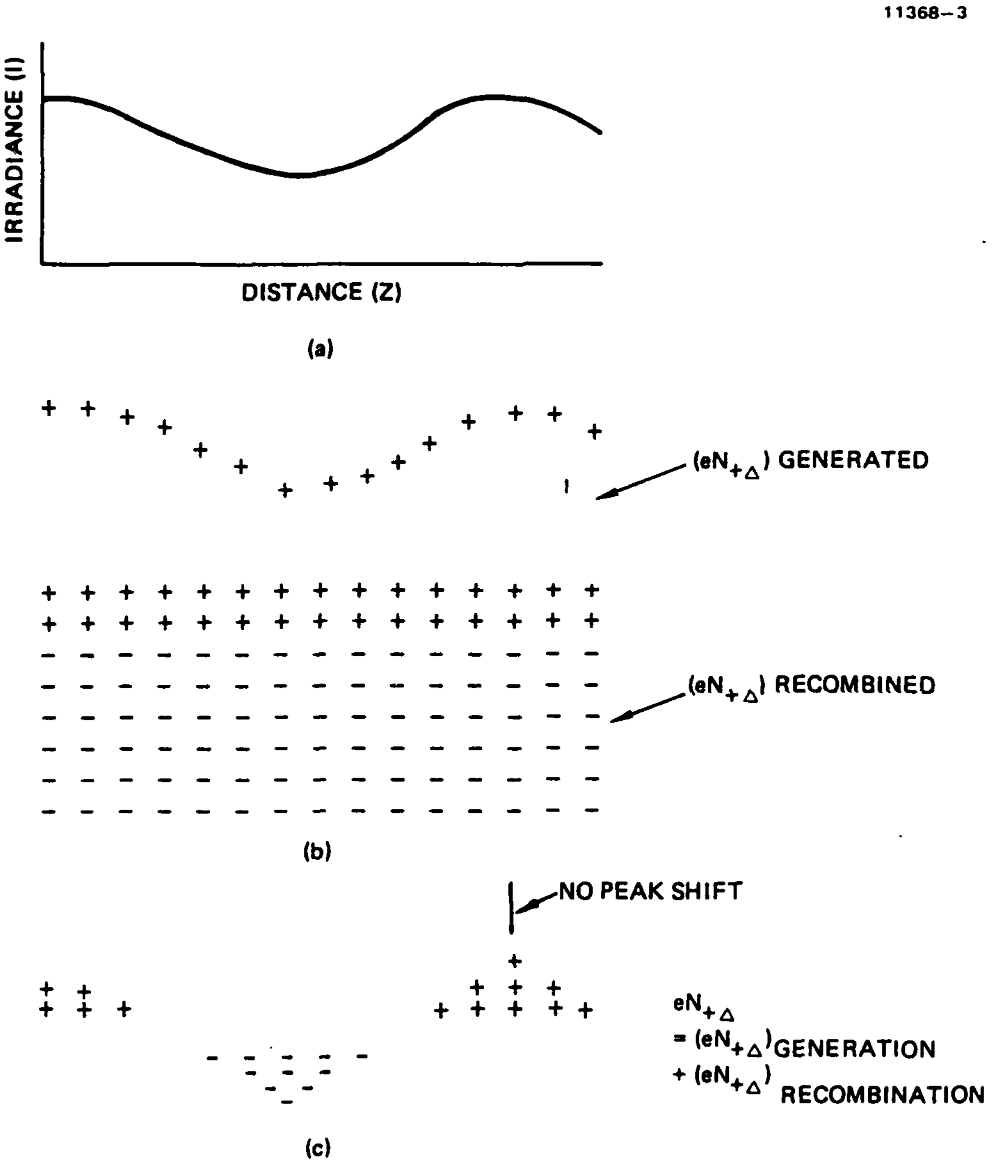
11368-3
IRRADIANCE (I)
DISTANCE (Z)
(a)
(eN+Δ) GENERATED
(eN+Δ) RECOMBINED
(b)
NO PEAK SHIFT
eN+Δ
= (eN+Δ)GENERATION
+ (eN+Δ) RECOMBINATION
(c)

Figure 3. Schematic illustration of the positive and negative charge distributions for the case of long diffusion distance ($\Lambda k_g \gg 1$) showing the total charge distribution ρ that is spatially in phase with the irradiance.

which is written as

$$E_{sc} = \gamma_{di} t E_{\Lambda} M \sin k_g z \qquad \text{(3.22)}$$

where

$$E_{\Lambda} \equiv \gamma_r/\mu k_g \qquad \text{(3.23)}$$

is the field at which the drift velocity μE_{Λ} is equal to k_g^{-1}/τ_r.

The steady-state value of E for arbitrary J_0 is, from Equation 3.11 and $J = J_0$,

$$E = -J_0/e\mu n \quad . \qquad \text{(3.25)}$$

The corresponding steady-state value of the drift distance is

$$\Lambda_{Ess} = \mu E \tau_r = J_0/e\gamma_r n \quad . \qquad \text{(3.26)}$$

For $k_g \Lambda_{drss} \gg 1$, n is approximately constant as discussed above. Then Equation 3.25 gives E = constant; thus, there is no grating (which requires a z dependence of E) in this order of approximation. Keeping higher order terms in n gives a nonzero grating.

For $k_g \Lambda_{drss} \ll 1$, n is given by Equation 3.1 and there is a nonzero grating, which is given by Equation 3.26. Thus, Equation 3.25 gives the steady-state field

$$E = -\frac{J_0/e\mu\langle n\rangle}{1 + a\ M \cos k_g z} , \qquad \underline{(3.27)}$$

where

$$a = 1 \qquad \text{for } J_0 k_g / e\gamma_r \ll 1$$

$$a = 0 \qquad \text{for } J_0 k_g / e\gamma_r \gg 1 .$$

Equations 3.17, 3.22, and 3.27 give

$$E \cong \gamma_{di} t e^{-\gamma_{di} t} E_\Lambda M \sin k_g z$$
$$- \left[(J_0/e\mu\langle n\rangle)/(1 + a\ M \cos k_g z)\right]\left(1 - e^{-\gamma_{di} t}\right)^2 . \qquad \underline{(3.28)}$$

SECTION 4

DIFFUSION DOMINATED

As in the previous case of drift only, the charge density for the case of $k_g \Lambda_d << 1$ (where Λ_d is the diffusion distance discussed below) for diffusion only can be obtained from physical arguments similar to those used above in the discussion of Figure 3.1. For diffusion, half of the electrons diffuse to the left and half diffuse to the right, in contrast to the drift case above in which all electron drift to the right in Figure 2. Thus, Equation 3.9 is replaced by

$$(eN_{+\Delta})_{rcmb} = -e\langle\gamma_I\rangle N_{e0} t \Big[1 + \frac{1}{2} M \cos k_g (z - \Lambda_d) + \frac{1}{2} M \cos k_g (z + \Lambda_d)\Big] \quad . \qquad (4.1)$$

Using the Taylor expansion

$$\cos k_g(z \pm \Lambda_d) \cong \cos k_g z \pm k_g \Lambda_d \sin k_g z - \frac{1}{2} k_g^2 \Lambda_d^2 \cos k_g z$$

and adding Equations 4.1 and 3.8 gives

$$eN_{+\Delta} = \frac{1}{2} e\langle\gamma_I\rangle N_{e0} k_g^2 \Lambda_d^2 M t \cos k_g z \quad . \qquad (4.2)$$

With

$$\Lambda_d^{\,2} = D\tau_r \tag{4.3}$$

where D is the diffusion coefficient. Using n given by Equations 3.1 and 3.2, Equation 4.2 and $\rho \cong eN_{+\Delta}$ give

$$\rho \cong \frac{1}{2}\, eDk_g^{\,2}\langle n\rangle Mt \cos k_g z \quad . \tag{4.4}$$

The corresponding electric field is, from Equation 3.5

$$E = E_{sc} = \frac{1}{2}\, \gamma_{di} t\, E_d' M \sin k_g z \quad , \tag{4.5}$$

where

$$E \equiv Dk_g/\mu \tag{4.6}$$

is the electric field for which the drift velocity μE_d is equal to the grating distance k_g^{-1} divided by the diffusion time $(Dk_g^{\,2})^{-1}$.

The steady-state value of E for the present case of $k_g \Lambda_d \ll 1$ and diffusion only is also easy to obtain. For diffusion only, the current, which must be spatially constant in the steady state, is zero, $J = J_0 = 0$, because there is no applied field and no surface charges. Setting $J = 0$ and $p = 0$ in Equation 2.10 gives

$$\mu n E = D \partial n / \partial z \quad . \qquad (4.7)$$

Since $J = 0$, n is given by Equations 3.1 and 3.2. With Equation 4.7 this gives

$$E = \frac{E_d M \sin k_g z}{1 + M \cos k_g z} \qquad \underline{(4.8)}$$

For $M << 1$, $E \cong E_d M \sin k_g z$ is in spatial quadrature with the irradiance. When M is not small, E is not sinusoidal, just as it was not for the case of drift. By symmetry, the Fourier component in spatial phase is zero.

The electron transport stops when the drift in the space-charge field increases to the value at which this drift cancels the transport from diffusion. Thus, the characteristic time for the steady state to be approached is just the characteristic time for charge buildup, which is the dielectric-relaxation time $\tau_{di} = 1/\gamma_{di}$, where γ_{di} is defined in Equation 3.7. This time constant can be verified as follows: For convenience, set $\sin k_g z = 1$ and $\cos k_g z = 0$ in Equations 4.5 and 4.8. Equating the short-time solution in Equation 4.5 to the steady-state value in Equation 4.8 and solving for t gives one definition of the characteristic time (that would equal the exponential time constant if the E field increased exponentially). This gives $t = 2\tau_{di}$, which is approximately equal to the dielectric-relaxation time as expected.

From Equations 3.17, 4.5, and 4.8,

$$E \cong \gamma_{di} t \, e^{-\gamma_{di} t} \frac{1}{2} E_d M \sin k_g z$$

$$+ \left[E_d M \sin k_g z/(1 + M \cos k_g z)\right] \left(1 - e^{-\gamma_{di} t}\right)^2 \quad . \qquad \underline{(4.9)}$$

Next consider the case of $k_g\Lambda_d >> 1$. In this long-diffusion-distance limit for short times, the electron density is constant and is given by Equation 3.17, just as for the case of $k_g\Lambda_{dr} >> 1$ considered in Section 3. The electric field at short times is therefore given by Equation 3.20.

$$E = E_{sc} = \gamma_{di} t \, E_{rg} M \sin k_g z \quad , \qquad \underline{(4.10)}$$

where

$$E_{rg} = \gamma_r/\mu k_g$$

as in Equation 3.21.

The steady-state value of E from Equation 4.7 with $n \equiv$ const is $E = 0$. A nonzero value of E in the steady-state results from the next order correction to n. An example of the calculation of the steady-state value of E is given in Section 8 in the discussion of the results of Kukhtarev and coworkers.

From Equations 3.17 and 4.10

$$E \cong \gamma_{di} t \, e^{-\gamma_{di} t} E_{rg} M \sin k_g z + E_{Dss} \left(1 - e^{-\gamma_{di} t}\right)^2 \quad . \qquad \underline{(4.11)}$$

As an example of E_{Dss}, from Section 8 for the case of $N_{+0} << N_{e0}$, from Equation 8.10

$$E_{Dss} = - (4\pi e N_{+0}/\epsilon k_g) M \sin k_g z \quad . \qquad (4.12)$$

SECTION 5

PHOTOVOLTAIC-EFFECT DOMINATED

The photovoltaic effect is discussed in Section 9. It is easy to show that the results in Section 3 (for applied field only) are valid for the photoelectric effect if E_{app} is replaced by the steady-state photovoltaic field:

$$E_p = \Lambda_p \gamma_r/\mu = pN_e\langle I\rangle/e\mu\langle n\rangle \tag{5.1}$$

from Equation 9.8. This prescription of replacing E_{app} by E_p can be understood as follows: The central feature of the Glass[5] explanation of the photovoltaic effect is that the electrons generated by the irradiance are emitted preferentially in a direction given by a unit vector $\hat{c}$. The electrons are displaced through an effective distance Λ_p in the $\hat{c}$ direction, as discussed in Section 9. Thus, Equation 3.9 is valid if Λ_{dr} is replaced by Λ_p. The prescription of replacing E_{app} by E_p in the expression $\Lambda_{dr} = \mu E_{app}/\gamma_r$ is equivalent to replacing Λ_{dr} by Λ_p, as seen by making the replacement (5.1) in the Λ_{dr} expression. Replacing E_{app} by E_p in Equations 3.4 and 3.5 and integrating Equation 3.5 for short times gives, for $\Lambda_p k_g \ll 1$,

$$E \cong \gamma_{di} t\, E_p M \cos k_g z. \tag{5.2}$$

This result can also be obtained from the continuity equation $\partial p/\partial t = \partial J/\partial z$, with $I = -e\mu nE + pN_eI \cong pN_eI$ for short times. Notice that $k_g\Lambda_p \ll 1$ is always satisfied for cases of interest (because $\Lambda_p \cong 0.1$ nm and $k_g \approx 1/500$ nm).

As the time increases further, the space charge builds up until $J = J_0 =$ constant, which is the condition for the steady state as discussed above. Setting $J = J_0$ in Equation 2.10 (with $D = 0$), solving for the steady state field, and using

$$pN_{eo}\langle I\rangle/e\mu\langle n\rangle = \Lambda_p\gamma_r/\mu = E_p$$

gives

$$E = \left[E_p(1 + M\cos k_g z) - J_0/e\mu\langle n\rangle\right]/(1 + M\cos k_g z). \qquad (5.3)$$

The first term E_p is independent of z. Thus, there is no steady-state grating for open circuit conditions ($J_0 = 0$), just as for an applied field. However, there is a nonzero correction to this result when diffusion and/or an applied field are added. The $\langle n\rangle$ in the numerator in Equation 5.3, which comes from $n \cong \langle n\rangle(1 + M\cos k_g z)$ is a zeroth order approximation. Kukhtarev and coworkers obtained the following first order correction for the case of $k_g\Lambda \ll 1$:

$$n \cong \langle n\rangle\left[1 + M(1 - \xi)\cos k_g z\right] \qquad (5.4)$$

where

$$\xi \equiv \xi_T + \xi_E = (E_d + E_{app})/E_g \qquad (5.5)$$

with

$$E = 4\pi e N_{+0}/\epsilon k_g \ . \qquad (5.6)$$

Expanding in powers of ξ gives

$$\frac{1 + M \cos k_g z}{1 + M\,(1 - \xi) \cos k_g z} \cong 1 + \frac{\xi\, M \cos k_g z}{1 + M \cos k_g z} \ .$$

Thus, the z-dependent terms in Equation 5.3 for the case of $k_g\Lambda << 1$ are

$$E \cong (E_p\, \xi\, M \cos k_g z - J_0/e\mu\langle n\rangle)/(1 + M \cos k_g z). \qquad \underline{(5.7)}$$

[My preliminary results give a different correction to n from the value in Equation 5.4 by Kukhtarev and coworkers. The discrepancy, which is unimportant in the present cases, in which the photovoltaic effect is negligible, will be resolved in a later note.]

Combining Equations 3.17, 5.2, and 5.7 gives, for $\Lambda_p k_g << 1$,

$$\begin{aligned} E \cong\ & \gamma_{di} t\, e^{-\gamma_{di} t} E_p\, M \cos k_g z \\ & + \frac{E_p\, \xi\, M \cos k_g z - J_0/e\mu\langle n\rangle}{(1 + M \cos k_g z)} \left(1 - e^{-\gamma_{di} t\ 2}\right) , \text{ for } k_g\Lambda >> 1 \end{aligned} \qquad \underline{(5.8)}$$

For E_{app} and D included and $K_g\Lambda >> 1$, n is approximately constant. Then, replacing $1 + M \cos k_g z$ by 1 in the denominator in Equation 5.3 gives, for $k_g\Lambda >> 1$

$$E \cong E_p \left(1 + M \cos k_g z\right) - J/e\mu\langle n\rangle \qquad \underline{(5.9)}$$

Equations 3.17, 5.2, and 5.9 give for this case of $k_g\Lambda >> 1$,

$$E \cong \gamma_{di} t e^{-\gamma_{di} t} E_p M \cos k_g z + E_p M\left(\cos k_g z\right) \left(1 - e^{-\gamma_{di} t}\right)^2 \quad . \qquad \underline{(5.10)}$$

As an interesting side point, for an applied field the voltage at small times is E_{app}, and the voltage decays to zero as the space-charge field builds up as time approaches infinity. The space-charge field builds up to cancel the applied-field, given a net zero field. For the photovoltaic case, the electric field is small at small times and approaches E_p as the space-charge field builds up as time approaches infinfity. (The field E_p is the space-charge field generated by the photovoltaic effect). The space-charge field builds up and cancels the photovoltaic current, giving a nonzero field.

SECTION 6

DEPLETION AND SATURATION

The conditions for no depletion of the electrons in the N_e levels (which determine the optical absorption coefficient $\beta = \sigma_D N_e$) and no saturation of the available recombination levels N_+ (which determine the effective recombination frequency $v_{th} s N_+$) are given in Equations 2.17 and 2.18, respectively. The first condition required for no depletion and no saturation is that the steady-state value $(\langle\gamma_{I0}\rangle/\gamma_r)N_{e0}$ of the amplitude of n, from Equations 3.1 and 3.2, must be sufficiently small for Equations 2.17 and 2.18 to be valid. By conservation of electrons, the number of electrons N_{e0} available to be photoexcited at t = 0 must always be equal to the total number of electrons

$$N_{e0} = \langle N_e\rangle + \langle n\rangle \tag{6.1}$$

where ⟨ ⟩ is spatial average, as defined in Equation 1.3.

Taking the spatial averages of Equations 2.17 and 2.18 gives

$$|\langle N_{+\Delta}\rangle| \ll N_{+0} \text{ , for negligible saturation} \tag{6.2}$$

and

$$|\langle N_{e\Delta}\rangle| = |\langle N_{+\Delta}\rangle| \ll N_{e0}, \text{ for negligible depletion.} \tag{6.3}$$

From Equation 6.1 and $\langle N_e\rangle - N_{e0} = \langle N_e - N_{e0}\rangle = \langle N_{e\Delta}\rangle$,

$$\langle n\rangle = \langle N_{e\Delta}\rangle \quad . \tag{6.4}$$

Thus, Equations 3.2 and 6.4 give

$$\langle N_{e\Delta}\rangle = (\langle\gamma_I\rangle/\gamma_r)N_{e0} \quad , \tag{6.5}$$

which requires

$$\langle\gamma_I\rangle \ll \gamma_r \ , \quad \text{for negligible depletion} \tag{6.6}$$

as seen by comparing Equations 6.3 and 6.5.

The corresponding condition for negligible saturation is obtained by writing Equation 6.5 as

$$\langle N_{e\Delta}\rangle = (\langle\gamma_I\rangle/\gamma_r)(N_{e0}/N_{+0})N_{+0} \quad . \tag{6.7}$$

Comparison of Equations 6.7 and 6.2, with $|N_{+\Delta}| = |N_{e\Delta}|$ from Equation 2.16, gives

$$\langle\gamma_I\rangle \ll (N_{e0}/N_{+0})\gamma_r \ , \quad \text{for negligible saturation.} \tag{6.8}$$

The value of $\langle I\rangle$ corresponding to Equation 6.6 is $\langle I\rangle \ll I_{sat}$, where

$$\begin{aligned} I_{sat} &= \gamma_r\hbar\omega/\sigma \\ &= 2 \times 10^2 \ s^{-1} \ (4.0 \times 10^{-19} J)/5 \times 10^{-18} \ cm^2 \\ &= 1.6 \times 10^{11} \ W/cm^2 \quad . \end{aligned} \tag{6.9}$$

This very large typical value of $I_{sat} \cong 10^{11}$ W/cm^2, compared with typical cw values of 10 W/cm^2 and rather large pulsed values of 10^8 W/cm^2 (1 J/cm^2 and 10 msec) shows that saturation and depletion are not likely to be problems in fairly heavily doped samples even under short-pulse-duration operation. It is possible that N_{e0}/N_{+0} in Equation 6.8 could be small, thus lowering the saturation threshold. However, in most current high-speed, real-time applications it is desirable to make N_{+0} small and N_{e0} large, so that saturation is negligible (Equation 6.8), if depletion is negligible (Equation 6.6).

In addition to these restrictions (Equations 6.6 and 6.8) on the maximum irradiance I, there are restrictions imposed on the values of N's in order that the values of $\rho \equiv eN_{+\Delta}$ at longer times ($t >> \tau_r$) can be obtained. For example, the maximum value of E in Equation 3.16 for the case of $J_0 = 0$ and applied field only is, to within a numerical factor of order 1, E_{app} M, and the corresponding value of $|N_{+\Delta}|$ from Equation 3.10 with $t = \gamma_{di}{}^{-1}$ and $\Lambda_{dr} = \mu\tau_r E \equiv \mu\tau_r E_{app} M$ is

$$|N_{+\Delta}| = N_{sat} \equiv \epsilon k_g E_{app} M^2/4\pi e \quad . \qquad \underline{(6.10)}$$

With Equations 6.2 and 6.3, this gives

$$N_{sat} << N_{+0}, N_{e0} \qquad (6.11)$$

where N_{sat} is defined in Equation 6.10.

According to Equations 6.11 and 6.10, both N_{+0} and N_{e0} must the greater than

$$N_{sat} \cong \frac{6(3 \times 10^5 \text{ cm}^{-1})(10^4 \text{V/cm})(1/300)(\text{SV/V})}{4\pi \; 4. \times 10^{-10} \; (\text{ergcm})^{1/2}} = 10^{16} \text{ cm}^{-3} \qquad (6.12)$$

for E_{app} = 10 kV/cm, $\varepsilon = (2.3)^2$, $\sin\theta = 0.5$, $\lambda = 500$ nm, and $M \cong 1$. This is a rather small value of N_{sat} — corresponding to ~ $10^{16}/5 \times 10^{22} = 2 \times 10^{-7}$ 0.2 part per million of Fe^{2+} and Fe^{3+}. Large dopings are commonly used. Thus, the usual doping are sufficiently large to avoid the long-time saturation and depletion. However, for small values of M, the factor M^2 in Equation 6.10 can make N_{sat} small.

In the general case, N_{sat} must satisfy Equation 6.10, with

$$N_{sat} = \varepsilon k_g E_{gmx} M/4\pi e \quad , \qquad \underline{(6.13)}$$

where E_{gmx} is the maximum value of the z dependent electric field that gives the grating amplitude.

SECTION 7

STEADY-STATE RESULTS

The steady state has been considered for individual processes in the previous sections. Since the value of $k_g\Lambda$ for all processes affects the individual processes, it is convenient to consider the steady state with all processes included. The key equations for determining the steady state field E are

$$E = (eD\partial n/\partial t + pN_e I - J_0)/e\mu n \tag{7.1a}$$

$$E = (eD\partial n/\partial z + pN_e \langle I \rangle M \cos k_g z + e\mu \langle n \rangle \langle E \rangle)/e\mu n \tag{7.1b}$$

$$E = (eD\partial n/\partial t + pN_e I)/e\mu n \, , \qquad \text{open circuit} \tag{7.1c}$$

$$E = (eD\partial n/\partial z + pN_e \langle I \rangle M \cos k_g z)/e\mu n \, , \qquad \text{short circuit} \tag{7.1d}$$

$$E = (eD\partial n/\partial t + pN_e \langle I \rangle M \cos k_g z + e\mu \langle n \rangle E_{app})/e\mu n, \text{ for } \langle E \rangle = E_{app} \tag{7.1e}$$

$$\partial E/\partial z = 4\pi e \varepsilon^{-1}(N_{+0} - n) \tag{7.2}$$

$$N_+ = (\gamma_I/\gamma_r)(N_e N_{+0}/n) \tag{7.3}$$

and

$$\langle N_{+\Delta} - n \rangle = 0 \quad . \tag{7.4}$$

Equation 7.1 is obtained from the steady-state condition $J = J_0 =$ constant $\neq f\,(z,t)$. The average field $\langle E \rangle$ from Equation 7.1a is

$$\langle E \rangle = (pN_e \langle I \rangle - J_0)/e\mu \langle n \rangle \quad . \tag{7.5}$$

Solving Equation 7.5 for J_0 and substituting the result into Equation 7.1a gives Equation 7.1b. For an open circuit, setting $J_0 = 0$ in Equation 7.1a gives Equation 7.1c. For a short circuit $\langle E \rangle = 0$, Equation 7.1b reduces to Equation 7.1d. For a voltage $V_{app} = \ell E_{app}$ applied with ohmic contacts, $\langle E \rangle = E_{app}k$, and Equation 7.1b reduces to Equation 7.1e.

Equation 7.2 is Equation 2.11 with a ρ given by Equation 2.12. Equation 7.3 is obtained from Equation 2.9 with $\partial N_+/\partial t = 0$.

Equation 7.4 is the quasi charge-neutrality condition, which arises as follows: In general, charge neutrality means that the charge density ρ is zero. Then, integrating Poisson's equation $\nabla \cdot \varepsilon E = 4\pi\rho$ gives E = constant for the current case in which $\varepsilon \cong$ constant. (It is easy to show that the spatial dependence of $\varepsilon = n_g^2$ corresponding to the spatial dependence of grating index n_g is negligible in the cases considered here). Quasi-charge neutrality in the context of index gratings means that the constant term $\langle\rho\rangle$ in $\rho = \langle\rho\rangle + \rho\Delta$ must equal zero in order to avoid the unphysical term $E \sim \langle\rho\rangle z$ in the electric field. Thus, Equation 2.12 and $\langle\rho\rangle = 0$ give Equation 7.4.

The case of short steady-state electron transport distance is simple. [The condition for this short transport distance will be considered later. Kukhtarev's condition $\xi \ll 1$ and $\xi_E \ll 1$ are sufficient if $\langle n\rangle < N_{+0}$, but are not necessary in general. Physically I would expect $k_g\Lambda_{ss} \ll 1$ with $\Lambda_{ss} = \mu E_{ss}\tau_r + (D\tau_r)^{1/2}$.] The electron concentration from Equation 3.1 and 3.2 is $n = \langle n\rangle(1 - M \cos k_g z)$. Substitution into Equation 7.1a gives

$$E_\eta = (E_p \, \xi \, M \cos k_g z + E_d \, M \sin k_g t - J_0/e\mu\langle n\rangle)/(1 + M \cos k_g z) \qquad (7.6)$$

where

$$E_p \equiv \Lambda_p \gamma_r/\mu = pN_e\langle I\rangle/e\mu\langle n\rangle \ , \quad E_d = Dk_g/\mu \ . \qquad (7.7)$$

The term $E_p\xi M \cos k_g z/(1 + M \cos k_g z)$ arises from the deviation of n from $\langle n\rangle$ $(1 + M \cos k_g z)$, as discussed in the derivation of Equation 5.7. [The consistency of E_η in Equation 7.6 with Equations 7.2 to 7.4 will be demonstrated below. This consistency establishes the conditions required for $n = \langle n\rangle$ $(1 + M \cos k_g z)$ to be valid].

The case of long steady-state electron-transport distance requires some care. For example, formally setting $n = \langle n\rangle$ in Equation 7.1 would give

$$E = E_p \, (1 + M \cos k_g z) \ , \qquad \text{for } n = \langle n\rangle \ . \qquad (7.8)$$

This result is incorrect because the deviation in n from ⟨n⟩ gives terms in Equation 7.1 that are much greater than E_p in general, as will now be shown. Setting

$$n = \langle n \rangle + n_\delta \quad , \qquad N_e = \langle N_e \rangle + N_{e\delta}$$

in Equation 7.3 and using $N_{+\Delta} = N_+ - N_{+0}$ gives

$$N_{+\Delta} - n = \left(\frac{N_{+0}}{1 + n_\delta/\langle n \rangle}\right)\left(\frac{\langle \gamma_I \rangle \langle N_e \rangle}{\gamma_r \langle n \rangle}\right)(1 + M \cos k_g z)(1 + N_{e\delta}/\langle N_e \rangle) - N_{+0} - \langle n \rangle - n_\delta \quad . \tag{7.9}$$

with $n_\delta << \langle n \rangle$, which will be verified below, and

$$N_{e\delta} = r\langle N_e \rangle M \cos k_g z \quad . \tag{7.10}$$

and

$$(1 + M \cos k_g z)(1 + r M \cos k_g z) = 1 + \frac{1}{2} r M^2 + (1 + r) M \cos k_g z + \frac{1}{2} r M^2 \cos 2k_g z \quad , \tag{7.11}$$

Equation 7.9 becomes

$$N_{+\Delta} - n = \langle N_{+\Delta} - n \rangle + (N_{+\Delta} - n)_\delta \tag{7.12}$$

where

$$\langle N_{+\Delta} - n \rangle = N_{+0}(g/\eta - 1 - \eta) \tag{7.13a}$$

and

$$(N_{+\Delta} - n)_{\delta} = N_{+0} \frac{\langle\gamma_I\rangle\langle N_e\rangle}{\gamma_r\langle n\rangle} \left[(1 + r)M\cos k_g z + \frac{1}{2} r M^2 \cos k_g z\right] \quad (7.13b)$$

with

$$g \equiv (\langle\gamma_I\rangle/\gamma_r)(\langle N_e\rangle/N_{+0}\left(1 + \frac{1}{2} r M^2\right) \quad . \quad (7.14)$$

The factor r in Equation 7.10 is a measure of depletion. For $r \ll 1$, $N_e \cong \langle N_e\rangle \cong N_{e0}$. Since $N_{\Delta e} = -N_{\Delta +}$ from Equation 2.16, assuming that $N_{e\Delta} \cong N_{e\delta}$ and $\langle N_e\rangle \cong N_{e0}$ in Equation 7.10 gives

$$|r| \cong N_{+0}/N_{e0} \quad . \quad (7.15)$$

Setting $\langle N_{+\Delta} - n\rangle$ equal to zero, to obtain quasi charge neutrality, gives

$$\eta = (1/4 + g)^{1/2} - 1/2 \quad (7.16a)$$
$$\cong g^{1/2} \qquad \text{for } g \gg 1 \quad (7.16b)$$
$$\cong g \qquad \text{for } g \ll 1 \quad . \quad (7.16c)$$

These results can be written as:

$$\langle n\rangle \cong \left[\langle\gamma_I\rangle\langle N_e\rangle N_{+0}\left(1 + \frac{1}{2} r M^2\right)/\gamma_r\right]^{1/2} \gg N_{+0}$$

$$\text{for } \langle\gamma_I\rangle \gg N_{+0}\gamma_r/\langle N_e\rangle \quad (7.17a)$$

$$\langle n\rangle \cong (\langle\gamma_I\rangle/\gamma_r)\langle N_e\rangle\left(1 = \frac{1}{2}\, r\, M^2\right) << N_{+0},\ \text{for } \langle\gamma_I\rangle << N_{+0}\gamma_r/\langle N_e\rangle \quad (7.17b)$$

We consider only the low-irradiance limit $g << 1$. Equation 7.14 and $g << 1$ give

$$\langle\gamma_I\rangle << N_{+0}\gamma_r/\langle N_e\rangle\ \left(1 + \frac{1}{2}\, r\, M^2\right) \quad , \qquad (7.18)$$

in which

$$\langle n\rangle = \left(\langle\gamma_I\rangle/\gamma_r\right)\langle N_e\rangle\ \left(1 + \frac{1}{2}\, r\, M^2\right) \quad , \qquad (7.19)$$

which agrees with Equation 3.2 in the limit of negligible depletion, $\langle N_e\rangle \cong N_{e0}$, and $r << 1$. Equations 7.14 and 7.19 give

$$(N_{+\Delta} - n)_z \cong N_{+0}\,\frac{(1 + r)\, M}{1 + \frac{1}{2}\, r\, M^2}\cos k_g z + N_{+0}\,\frac{\frac{1}{2}\, r\, M^2}{1 + \frac{1}{2}\, r\, M^2}\cos k_g z \quad . \ (7.20)$$

Substituting Equation 7.20 into Equation 7.2 and integrating gives

$$E = E_q\left[\frac{(1 + r)\, M}{1 + \frac{1}{2}\, rM^2}\sin k_g z + \frac{rM^2/4}{1 + \frac{1}{2}\, r\, M^2}\sin 2k_g z\right] \qquad \underline{(7.21)}$$

where

$$E_q = 4\pi e N_{+0}/\epsilon k_g \quad . \qquad (7.22)$$

For negligible depletion the inequality $r \ll 1$ is valid, i.e., $N_{+0} \ll N_{e0}$ from Equation 7.15. With $N_{e\Delta} = -N_{+\Delta}$ from Equation 2.16 and $N_{+\Delta} = N_{+0}\, M \cos k_g z$ from Equation 7.20 with $n_z \ll N_{+\Delta z}$, the term $N_e \delta/\langle E_e \rangle$ in Equation 7.9 is negligible for either $N_{+0} \ll N_{e0}$ or small modulation. In this case of $r \ll 1$, Equation 7.21 gives

$$E = E_q M \sin k_g z, \qquad \text{for } g,\ r \ll 1 \quad . \qquad \underline{(7.23)}$$

and Equation 7.14 and $N_+ = N_{+0} + N_{+\Delta}$ give

$$N_+ = N_{+0}\,(1 + M \cos k_g z), \qquad \text{for } g,\ r \ll 1 \quad , \qquad (7.24)$$

where $g \ll 1$ is the small-irradiance limit of Equation 7.17b and $r \ll 1$ is the negligible-depletion limit. Thus, for $M \ll 1$ not satisfied, depletion is not negligible ($N_{+\Delta}/N_{+0} = M \cos k_g z$ is not much less than unity).

The result in Equation 7.8 obtained formally (and incorrectly) by using $n = \langle n \rangle$ in Equation 7.1 is negligible with respect to the correct result in Equation 7.23, i.e.,

$$E_p/E_q = k_g \Lambda_p \epsilon \gamma_r / 4\pi e \mu N_{+0} = 3.7 \times 10^{-5} \ll 1 \quad . \qquad (7.25)$$

From Equation 5.5, we have $\xi_T = E_d/E_q$. Thus, $E_q \ll E_d$ for $\xi_T \gg 1$. With Equation 7.25 this gives

$$E_p \ll E_q \ll E_d \qquad \text{for long transport distance} \quad . \qquad (7.26)$$

The following check on the consistency of Equations 7.23 and 7.1 is not essential to the understanding of the control results. The small deviations in n from the large term $\langle n \rangle$ are retained and shown to be small and to account for the result in Equation 7.23. The field E in Equation 7.23 comes from the first term

in Equation 7.1. The small deviation in n from $\langle n\rangle$ must be retained in Equation 7.1 in order to obtain Equation 7.23. First consider the short-circuit case of Equation 7.1c. The second term in Equation 7.1c is negligible as shown in Equation 7.26. Setting $n = \langle n\rangle (1 + n_c M \cos k_g z)$ in Equation 7.1c and equating the resulting E to the E in Equation 7.23 gives, with
$Dk_g/\mu = E_d$,

$$E_d n_c M \sin k_g z = E_q M \sin k_g z \quad .$$

Solving for n_c gives

$$n_c = E_q/E_d = 4\pi e N'_{+0}\mu/\varepsilon D k_g^2 \equiv 1/\xi_T \ll 1 \qquad (7.27)$$

where ξ_T is Debye-length parameter of Kukhtarev and coworkers.

For the open-circuit case of Equation 7.1c defining $n = \langle n\rangle(1 + n_{cs})$, where $n_{cs} = n_c M \cos k_g z + n_s M \sin k_g z$, and using $(1 + n_{cs})^{-1} \cong 1 - n_{cs}$ for $n_{sc} \ll 1$ and setting the resulting E equal to the E in Equation 7.23 gives

$$E_d n_c M \sin k_g z - E_d n_s M \cos k_g z + E_p M \cos k_g z - E_p n_c M \cos k_g z$$
$$- E_p n_s M \sin k_g z = E_q M \sin k_g z \quad .$$

Setting the sum of the coefficients of the cos k_z terms equal to zero gives

$$n_s = E_p/E_d = \Lambda_p k_g/\Lambda_d^2 k_g^2 \ll 1 \qquad (7.28)$$

where $\Lambda_p k_g << 1$ is always satisfied and $\Lambda_d^2 k_g^2 >> 1$ is satisfied in the long transport limit. Setting the sum of the coefficients of the sin $k_g z$ terms equal to zero gives

$$n_c = \frac{E_q + E_p n_s}{E_d} << 1$$

where $E_q/E_d << 1$ from Equation 7.27, $n_s << 1$ from Equation 7.28, and $E_p/E_d << 1$ from Equation 7.28.

SECTION 8

RESULTS OF KUKHTAREV AND COWORKERS AND OF AMODEI

Several results of Kukhtarev and coworkers[3] and of Amodei[2] are discussed in order to show the relation between the present results and the results of these previous important papers and moreover to resolve inconsistencies among the three sets of results.

Kukhtarev and coworkers consider only the steady state. We set their thermal generation factor β equal to zero because the levels of interest here are too deep for thermal generation of free carriers to be important. We also neglect the small correction to M for the case of $k_g\Lambda << 1$ even though it should be simple to obtain this correction from the present model. The relations between Kukhtarev's notation and ours are as follows:

$$\begin{array}{lll} f \rightarrow \gamma_I & N_D^+ \rightarrow N_+ & N_A \rightarrow N_{+0} \\ \gamma_R \rightarrow \gamma_r/N_{+0} & \mathrm{Cos}\ (2k_x x + \phi) \rightarrow \cos k_g z & \mu T/|e| \rightarrow D \\ T \rightarrow k_B T & \xi_T \rightarrow E_d/E_q & \xi_E \rightarrow (E_{app} + E_p)/E_q \end{array}$$

Their condition

$$\gamma_I << \gamma_r n/N_{+0} \tag{8.1}$$

is valid only in samples having many more filled levels than empty levels, that is,

$$N_{+0} << N_{e0} \tag{8.2}$$

This can be seen as follows. Setting $\partial N_+/\partial t = 0$ and $N_e = N_p + N_{+0}$ in Equation 2.9 and solving for N_+ gives

$$N_+ = \frac{\gamma_I N_p}{\gamma_I + \gamma_r n/N_{+0}} \tag{8.3a}$$

$$\cong (\gamma_I/\gamma_r) N_D N_{+0}/n \tag{8.3b}$$

where the approximate equality in Equation 8.2b is valid when the Kukhtarev- and coworkers unequality in equation 8.1 is valid. Again setting $\partial N_+/\partial t = 0$ in Equation 2.9, but retaining N_e, and using Equations 2.14 to 2.16 gives

$$n = \left(n_{unsat}\right)\left(\frac{1 - N_{+\Delta}/N_{e0}}{1 + N_{+\Delta}/N_{+0}}\right) , \tag{8.4}$$

where

$$n_{unsat} = (\gamma_I/\gamma_r) N_{e0} = (\langle\gamma_I\rangle/\gamma_r) N_{e0} \; (1 + M \cos k_g z) \; . \tag{8.5}$$

Equation 8.3b can be rewritten as

$$n = n_{unsat} (N_D/N_{e0}) \frac{1}{1 + N_{+\Delta}/N_{+0}} \; . \tag{8.6}$$

The exact result in Equation 8.4 reduces to the approximate result in Equation 8.6 if $N_D \cong N_{e0}$. Then $N_{+0} << N_{e0}$, the factor $N_{+\Delta}/N_{e0}$ is negligible in the negligible-saturation limit, and the factor $N_D/N_{e0} \cong 1$ in Equation 8.5.

Equation 9 of Kukhtarev and coworkers with $m = M$ is in agreement with Equations 3.12, 4.8, and 5.3. Thus, our results and theirs agree for the short-transport distance limit of $k_g\Lambda << 1$. Their Equation 9 is valid even when their approximation $N_{+0} << N_D$ is not satisfied.

Next consider the limit $k_g\Lambda >> 1$. From Equation 8.6 with the Kukhtarev and coworkers approximation $N_D/N_{e0} \cong 1$, in order to have $n \cong \langle n \rangle$ we must have

$$N_{+\Delta} = N_{+0} M \cos k_g z \tag{8.7}$$

so that the factor $(1 + N_{+\Delta}/N_{+0})^{-1}$ in Equation 8.6 cancels the factor $(1 + M \cos k_g z)$ in n_{unsat} (see Equation 8.5). Notice that in this case of $N_{+0} << N_D$, the steady state is not reached until N_{+0} is "fully saturated" for $M \cong 1$, that is,

$$N_+ = N_{+0} (1 + M \cos k_g z) . \tag{8.8}$$

The charge density from Equation 2.5 is

$$\rho = e(N_{+\Delta} - n). \tag{8.9}$$

With $n << N_{+\Delta}$, substituting Equations 8.9 and 8.8 into Equation 2.11 and integrating gives

$$E = \langle E \rangle - E_q M \sin k_g z \tag{8.10}$$

where $\langle E \rangle$ is the obvious constant of integration and

$$E_q = 4\pi e N_{+0}/\epsilon k_g \quad , \tag{8.11}$$

is in agreement with Equation 7 of Kukhtarev and coworkers.

Finally, notice that Equation 8.10, which is Equation 7 of Kukhtarev and coworkers, is incorrect for the case of an applied field only and an open circuit because Equation 2.10 with $J = D = p = 0$ gives $E = 0$ for $n \neq 0$. The diffusion term in Equation 2.10 and the small deviation n_D in n from $\langle n \rangle$ are needed to establish the field in Equation 8.10 even through D does not appear in the result (because the $1/D$ in n_D cancels the explicit factor D in Equation 8.13).

Amodei[2] obtained the diffusion-dominated result

$$E \cong \frac{E_d M \sin k_g z}{1 + M \cos k_g z,} , \tag{8.12}$$

even in the limit of $\Lambda_{dif} k_g \gg 1$. This result disagrees with the present result in Equations 7.21 or 7.23 and with the result in Equation 8.10 from Kukhtarev and coworkers. The reason for the disagreement is that Amodei assumes that N_{e0} (his N) and N_{+0} (in his $\tau = 1/\gamma_r$) are constant. Then

$$n = \langle n \rangle (1 + M \cos k_g z) \tag{8.13}$$

rather than $n = \langle n \rangle$, as obtained here by Kukhtarev and coworkers

This result in Equation 8.12 is not correct in general because the changes in the values of N_+ and N_e cannot be neglected in the steady state in general. For example, N_{+0} was fully saturated in the case above, according to Equation 8.8. Equation 8.13 is physically implausable for this case of $k_g \Lambda \gg 1$ because the transport distance is greater than the distance k_g over which $\langle I \rangle M \cos k_g z$ changes substantially and the electrons cannot remain in the region in which they are generated if they diffuse or drift such a long distance before recombining.

The result in Equation 8.12 is also inconsistent with the value of E obtained from Poissons equations. For N_{+0} = constant, $N_{+0} = 0$, and Equation 2.5 gives

$$\rho = -en = -e\langle n\rangle(1 + M \cos k_g z) \ . \tag{8.14}$$

Substituting the z-dependence term into Equation 2.11 and integrating gives

$$E = -(4\pi e\langle n\rangle M/\varepsilon k_g)\sin k_g z \ ,$$

which does not agree with Equation 8.12. Finally, the constant term in ρ in Equation 8.14 does not vanish, as required by quasi-damage neutrality.

SECTION 9

PHOTOVOLTAIC EFFECT

In photovoltaic materials, a space-charge field is believed to be generated by asymmetric photoemission of conduction electrons.[1] In such ferroelectric materials as $LiNbO_3$ and $BaTiO_3$, ions can have potentials that are asymmetric along some direction. For example, the titanium ion in $BaTiO_3$ is displaced from the center of the lattice cell in the ferro-electric state. Thus, the photogenerated electrons are emitted preferentially in one direction, which gives rise to the photovoltaic field E_p as follows: By definition of the momentum transport time τ_k, the initial momentum is lost in time τ_k on the average. The displacement of the photogenerated electrons during the time τ_k has a typical value $\ell_p = \nu\tau_k = (10^7 \text{ cm/s})(10^{-14} \text{ s}) = 1 \text{ nm} (= 10 \text{ Å})$. All of the electrons are not photoemitted along the same direction, but there is a greater probability of emission along the photovoltaic direction. Thus, an effective distance Λ_p is defined as

$$\Lambda_p = p_+\ell_{p+} - p_-\ell_{p-} \equiv (p_+ - p_-)\ \ell_p \equiv p_{+-}\ \ell_p \qquad (9.1)$$

where p_+ and p_- are the probabilities of emission in the + and - directions, respectively.

A typical value of

$$\Lambda_p = 0.08 \text{ nm } (= 0.8 \text{ Å}) \qquad (9.2)$$

is consistent with typical observed photovoltages, as shown below. Equations 3.1 and 9.2 give $P_{+-} = \Lambda_p/\ell_p = 0.08 \text{ nm}/1 \text{ nm} = 0.08$ as the relative probability for emission in the positive photovoltaic direction. The short distance of 0.08 nm, which is less than an atomic spacing, is not the actual transport distance, which would be unrealistically short. Rather, it is the weighted distance, as in Equation 9.1.

In the literature,[3] it is common practice to model the photovoltaic effect by including the term

$$\underset{\sim}{J}_p = p_k I\hat{c} \qquad (9.3)$$

in the current, where p_k is a constant and $\hat{c}$ is a unit vector in the opposite direction from the preferred electron emission direction. The following derivation shows that Equation 9.3 is consistent with Glass' preferential emission model if the constant p_k is replaced by $p\ Nd_e$, where p is a constant and N_de is the trapped electron density:

$$J_p = p\ N_e I\hat{c} \quad . \qquad (9.4)$$

Equation 9.4, but not Equation 9.3, is equivalent to Glass' expression $J = \kappa\alpha I$ because the absorption coefficient α is proportion to N_e. Equations 9.3 and 9.4 are equivalent in the limit of no depletion ($N_e = N_{e0}$ = constant).

Equation 9.4 is obtained by considering the generation rate of electron by the field

$$(\partial n/\partial t)_I = (\sigma_D/\hbar\omega)I(z - \Lambda_p)N_e(z - \Lambda_p) \quad . \qquad (9.5)$$

The electrons generated from optical-donor levels at $z - \Lambda_p$ appear at the displaced position z. To Taylor expand in N_e gives

$$(\partial n/\partial t)_I = \sigma_D I(z)N_e(z)\hbar\omega - \partial(\Lambda_p\sigma_D I(z)N_e(z)/\hbar\omega)/\partial z \quad ,$$

which is of the usual form

$$\partial n/\partial t = \sigma_D I N_e/\hbar\omega - e^{-1}\partial J/\partial z$$

if we set

$$\underset{\sim}{J} = \underset{\sim}{J}_p = pN_e I\hat{c} \quad , \qquad (9.6)$$

where $\hat{c} = -\hat{z}$ and

$$p = e\Lambda_p \sigma_D/\hbar\omega \quad . \qquad (9.7$$

We shall use J_p in Equation 9.6, rather than the previous expression in Equation 9.3.

The photovoltaic field that develops in the steady state under open-circuit conditions (that is, $J = \langle n \rangle e\mu E + pN_e\langle I \rangle = 0$) is:

$$E_p = pN_e\langle I \rangle/\langle n \rangle e\mu = \Lambda_p \gamma_r/\mu \quad . \qquad (9.8)$$

The time constant for E_p to approach the steady state value in Equation 9.8 is the dielectric relaxation frequency γ_{di}, defined in Equation 3.7, as usual.

A small photovoltage

$$E_{psm} = 4\pi E\langle n \rangle \Lambda_p/\varepsilon = (\gamma_{di}/\gamma_r)E_p \qquad (9.9)$$

is developed in the short-time τ_r, as seen in the following model. Figure 4 schematically illustrates the charge distributions resulting from the displacement of the electrons, denoted by −, in the positive z direction by a distance Λ_p. The resulting net charge density in Figure 4 is approximated by δ-functions.

$$\rho = e\langle n \rangle \Lambda_p[\delta(z) - \delta(z - \ell)]$$

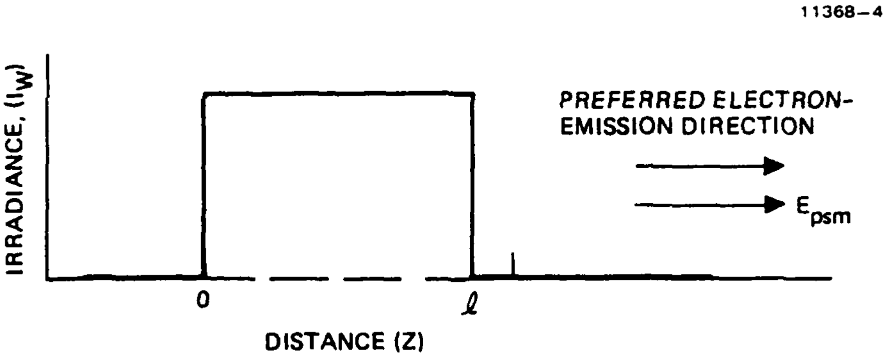

(a) IRRADIANCE DISTRIBUTION

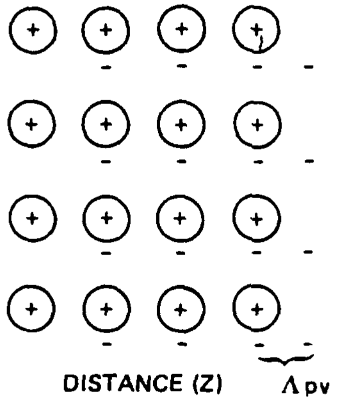

(b) RESULTING CHARGE ARRANGEMENT

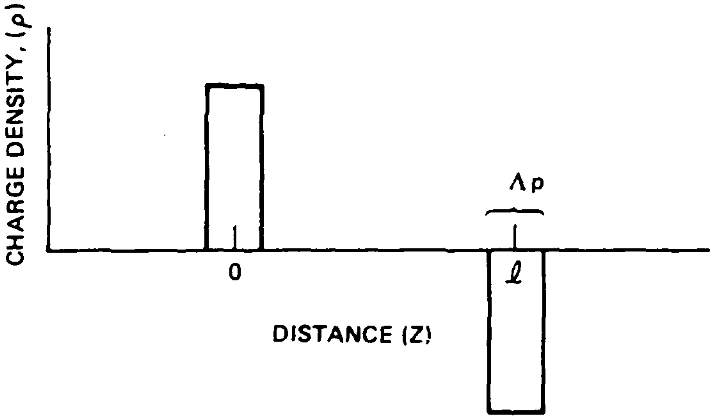

(c) RESULTING CHARGE DENSITY, ρ

Figure 4. Model for the photoelectric effort showing the idealized charge distribution resulting from net electron emission in the positive z direction.

where the electron concentration $\langle n \rangle$ develops in a characteristic time τ_r. Integrating Poisson's equation, $\epsilon dE/dz = 4\pi\rho$ gives,

$$\begin{aligned} E &= E_{psm} && \text{for } 0 < z < \ell \\ &= 0 && \text{for all other values of } z \end{aligned}$$

where E_{psm} is given by Equation 9.9. Since E_p developes in time τ_{di} and E_{psm} develops in time τ_r, it is reasonable that $E_{psm} = (\tau_r/\tau_{di})E_p = (\gamma_{di}/\gamma_r)E$, as in Equation 9.9.

SECTION 10

MODEL OF DIELECTRIC RELAXATION

The following model illustrates the significance of the dielectric relaxation frequency.

$$\gamma_r \equiv 1/\tau_r = 4\pi\sigma/\varepsilon = 4\pi e\langle n\rangle/\varepsilon \quad , \tag{10.1}$$

which is the time required to change or discharge a sample. Consider a dielectric sample in an externally applied electric field E_{app}, with open circuit conditions, as illustrated in Figure 5. At time $t = 0$, the sample is uncharged. The electric field E_{app} causes a current

$$J_0 = e\mu\langle n\rangle E_{app}$$

at time $t = 0$. The divergence of the current at the end-faces of the sample causes the end-faces to charge up, according to the continuity equation

$$\partial\rho/\partial t = -\partial J/\partial dz \tag{10.2}$$

where ρ is the charge density. For

$$J(z,t) = -e\mu\langle n\rangle E(t)r(z) \tag{10.3}$$

where

$$\begin{aligned} r(z) &= 1 \qquad \text{for } 0 < z < \ell \\ &= 0 \qquad \text{for all other values of } z \quad , \end{aligned} \tag{10.4}$$

Equation 10.2 gives

$$\partial\rho/\partial t = -e\mu\langle n\rangle E(t)\Delta(z) \quad , \tag{10.5}$$

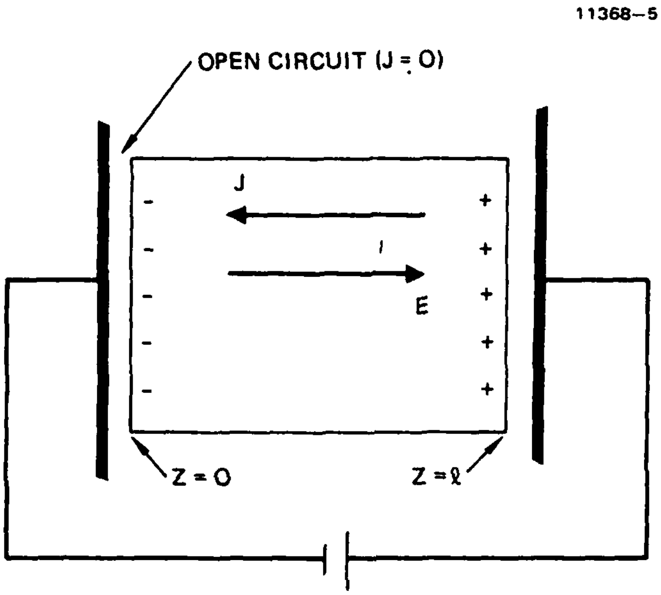
11368–5
OPEN CIRCUIT (J = 0)
J
E
-
+
Z = 0
Z = ℓ

Figure 5. Crystal with an applied field with open-circuit conditions at the faces of the crystal showing the current density J, electric field E, and charged faces of the crystal.

where

$$\Delta(z) = \delta(z) - \delta(z - \ell) \ . \qquad (10.6)$$

Here $\delta(z)$ is the Dirac δ-function, and $dr(z)/dz = \Delta(z)$.

From Poisson's equation,

$$\begin{aligned} \rho &= \varepsilon(4\pi)^{-1}\partial E/\partial t = \varepsilon(d4\pi)^{-1}\partial[E(t)r(z)]/\partial z \\ &= \varepsilon d(4\pi)^{-1}E(t)\Delta(z) \ . \end{aligned} \qquad (10.7)$$

Taking the time derivative of ρ with respect to time in Equation 10.7 and substituting the result into Equation 10.5 gives

$$\partial E(t)/\partial t = -(4\pi \ e\mu\langle n\rangle/\varepsilon)E(t) \ . \qquad (10.8)$$

For $E(t) = E_{app}$ at $t = 0$, the solution to Equation 10.8 is

$$E(t) = E_{app}e^{-\gamma_{di}t} \ , \qquad (10.9)$$

where γ_{di} is the dielectric relaxation frequency defined in Equation 10.1.

The model illustrates that the time constant for the development of the final charge density ($\rho = \rho_0\Delta(z)$), which corresponds to the charged end faces of the sample) is the dielectric-relaxation time. the electric field and current decay to zero as the end faces of the sample charge up.

Using the same model, but with $E_{app} = 0$ and $\rho = \rho_0\Delta(z)$ at time $t = 0$, it is easy to show that an initial charge decays with time-constant $1/\gamma_{di}$:

$$E = E_0 \ \varepsilon^{-\gamma_{di}t} \ . \qquad (10.10)$$

The current and electric field decay to zero as the end-face charge decays to zero.

SECTION 11

SUMMARY OF RESULTS

A list of symbols and typical values of parameters is given in the Appendix. Key results for the grating electric field E_g, which is the z-dependent part of $E = E_{app} + E_{sc}$ (which excludes the electric field of the laser irradiance), are listed below.

The corresponding value of the grating index is given by Equation 1.1 and repeated here

$$n_g = \frac{1}{2} n_r^3 rE \quad , \tag{1.1}$$

and the corresponding grating efficiency is given by an expression such as Equation 1.5 and repeated here, i.e.,

$$\eta = e^{-\alpha d/\cos\,\theta} \sin^2 \frac{\pi n_r n_g d}{2\lambda \cos\,\theta} \; . \tag{1.5}$$

The notation for the various cases of E below is as follows:

E_{app}: applied field dominated

D: diffusion dominated

p: photovoltaic-effect dominated

t: short-time solution ($\tau_r \quad t \quad \tau_{di}$)

ss: steady-state

Λ_{lng}: $k_g \Lambda >> 1$

Λ_{sht}: $k_g \Lambda << 1$

ngbl: negligible depletion and saturation.

Combining the results of Sections 3 through 7 gives the following key results:

From Equations 3.18, 4.9, 5.7 and 7.7, for $k_g\Lambda \ll 1$

$$E \cong \gamma_{di} t e^{-\gamma_{di} t} \left[(E_{app} + E_p) M \cos k_g z + \frac{1}{2} E_d M \sin k_g z \right] \;\; .$$

$$\times \left(\frac{E_p \, \xi \, M \cos k_g z - J_0/e\mu\langle n\rangle + E_d M \sin k_g z}{1 + M \cos k_g z} \right) \tag{11.1}$$

$$\times \left(1 - e^{-\gamma_{di} t} \right)^2 \quad , \text{ for } \Lambda_{short}, \text{ negligible}$$

where

$J_0/e\mu\langle n\rangle = 0$ for open circuit (11.2a)

$= E_p$ for short circuit (11.2b)

$= E_p - E_{app}$ for E_{app} with ohmic contents (11.2c)

From Equations 3.28, 4.11, 5.9, and 7.20, for $k_g\Lambda \gg 1$,

$$E = \gamma_{di} t e^{-\gamma_{di} t} (E_\Lambda + E_p) M \sin k_g z$$

$$+ E_q \left[\frac{(1 + r) M}{1 + \frac{1}{2} r M^2} \sin k_g z + \frac{r M^2/4}{1 + \frac{1}{2} r M^2} \sin 2k_g z \right] \tag{11.3}$$

$$\times \left(1 - e^{-\gamma_{di} t} \right)^2 \; .$$

The results for the phase shifts between the grating electric field and the grating irradance $\langle I \rangle M \cos k_g z$ are summarized for the various combination of long- and short- electron-diffusion distances and drift (in applied or photovoltaic field) and diffusion-limited transport in Table 2.

Table 2. Spatial Phase Shift Between the Grating (i.e., Photofractive Electrtic Field E) and Irradiance I.

	$k_g\Lambda \ll 1$		$k_g\Lambda \gg 1$	
	Drift	Diffusion	Drift	Diffusion
Phase	π	$-\pi/2$	$\pi/2$	$\pi/2$

REFERENCES

1. A.M. Glass, "The Photorefractive Effect," Optical Engineering, 17, 470-479 (1978).

2. Juan J. Amodei, "Analysis of Transport Processes During Holographic Recording in Insulators," RCA Review, 32, 185-198 (1971).

3. N.V. Kukhtarev, V.B. Markov, S.G. Odulov, M.S. Soskin and V.L. Vinetskii, "Holographic Storage in Electro-optic Crystals," Ferroelectrics, 22, 949-960, (1979).

4. Albert Rose, Concepts in Photoconductivity and Allied Problems, Interscience Tracts on Physics and Astronomy (Interscience Publishers, New York, 1963).

APPENDIX B

SELECTION OF PHOTOREFRACTIVE MATERIALS FOR DEGENERATE FOUR WAVE MIXING*

M.B. Klein, G.C. Valley
Hughes Research Laboratories
Malibu, CA 90265

and

M.S. Sparks
Scientific Research Center
Beverly Hills, CA.

*Supported in part by U.S. Air Force Contract No. F19628-80-C-0185

I Introduction

Some of the most attractive materials for practical applications of degenerate four wave mixing (DFWM) are photorefractive crystals such as lithium niobate ($LiNbO_3$), potassium niobate ($KNbO_3$), barium titanate ($BaTiO_3$), strontium barium niobate (SBN), bismuth silicon oxide (BSO) and many others. These crystals have large nonlinearities so that low power cw operation with small interaction volumes is possible. They are solids and operate at room temperature. Large diffraction efficiencies and phase conjugate reflectances have been achieved across the visible spectrum. Finally under some conditions, the refractive index interference pattern in these crystals is shifted 90° from the intensity pattern. This shifted grating, which at present is unique to photorefractive materials, allows construction of novel devices using four-wave mixing [1-3].

In order to analyze the performance of photorefractive materials for DFWM applications, it is first necessary to understand the formation of a space charge grating due to the interference of two waves within the medium. In the analysis presented here, we assume that the amplitudes of the two waves are known in a given volume element. The irradiance due to this interference of those waves is given by

$$I = I_0 \ (1 + m \cos k_g z \ ), \qquad (1)$$

where m is the modulation depth, k_g is the grating wave vector, and z is the direction normal to the grating planes. If the two input waves are co-polarized and have intensities I_1 and I_2, then

$$m = \frac{2\sqrt{I_1 I_2}}{I_1 + I_2} \qquad (2)$$

Grating formation in photorefractive materials can be characterized in terms of three parameters - the steady-state diffraction efficiency, the write or erase time, and the write or erase sensitivity. In the following section we review results for these performance parameters derived from the theory of photorefractive materials developed by Kukhtarev et al. [6-11]. In section 3 these results are applied to several photorefractive materials in order to predict differences in four wave mixing behaviour. In Section 4 we discuss materials improvement for optimal performance.

II Basic Equations

We start with the basic equations used by Kukhtarev, Vinetskii and coworkers [6-11]:

$$\frac{\partial n}{\partial t} - \frac{\partial N_D^+}{\partial t} = -\frac{1}{e}\frac{\partial j}{\partial z} \qquad \text{(continuity)} \qquad (3)$$

$$\frac{\partial N_D^+}{\partial t} = sI(N_D - N_D^+) - \gamma_R n N_D^+ \qquad \text{(rate equation)} \qquad (4)$$

$$j = e\mu n E - k_B T \mu \frac{\partial n}{\partial z} \qquad \text{(current equation)} \qquad (5)$$

$$\frac{\partial E}{\partial z} = \frac{4\pi e}{\varepsilon}(n + N_A - N_D^+) \qquad \text{(Poisson's law)} \qquad (6)$$

where n is the electron number density,

N_D is the total number density of dopants (Fe for example, ionized and neutral; N_D is a constant),

N_D^+ is the number density of ionized donors (Fe^{3+} for example),

N_A is the number density of negative charges that compensate for the charge of N_D^+ under dark conditions (N_A is a constant of the crystal),

$N_D-N_D^+$ is the number of neutral (filled) donors,

j is the current density,

s is the photoionization cross section,

I is the irradiance of the optical wave,

γ_R is the two-body recombination rate coefficient,

μ is the mobility,

E is the total electric field,

k_B is Boltzmann's constant,

T is the temperature,

e is the charge on the electron,

ε is the static dielectric constant.

One important parameter which has a strong influence on the performance of photorefractive materials is the reduction ratio, defined as

$$R = \frac{N_D-N_A}{N_A} = \frac{N_D}{N_A} - 1.$$

This parameter is just the ratio of filled empty donor states.

Equations (3) - (6) may be easily modified to include dark conductivity and the photovoltaic effect [8]. The equations do not consider secondary trapping levels or photorefractive centers [12, 13] or holes [14], all of which may be important under some conditions. These equations appear to give similar results to the recently developed hopping model [4].

The set of nonlinear equations can be solved by using two approximations: linearization in the grating modulation depth and the quasi-steady approximation in the zeroth-order electron number density [6]. With these approximations one can solve for the grating space charge electric field in the write and erase cases.

The grating space charge field during writing is given by

$$\delta E = mE_{sc}\,[-\cos(k_g z + \psi) + e^{-t/\tau_e}\cos(k_g z+\omega_e t+\psi)] \qquad (7)$$

where

$$\tau_e = \tau_{di}\,\frac{\left(1 + \frac{\tau_+}{\tau_{di}} + \frac{\tau_+}{\tau_D}\right)^2 + \left(\frac{\tau_+}{\tau_E}\right)^2}{\left(1 + \frac{\tau_+}{\tau_D}\,\frac{\tau_{di}}{\tau_1}\right)\left(1 + \frac{\tau_+}{\tau_{di}} + \frac{\tau_+}{\tau_D}\right) + \left(\frac{\tau_+}{\tau_E}\right)^2\frac{\tau_{di}}{\tau_1}} \qquad (8)$$

$$\omega_e = \frac{1}{\tau_{di}}\,\frac{\left(\frac{\tau_+}{\tau_E}\,\frac{\tau_{di}}{\tau_1}\right)\left(1 + \frac{\tau_+}{\tau_{di}}\right) - \frac{\tau_+}{\tau_E}}{\left(1 + \frac{\tau_+}{\tau_{di}} + \frac{\tau_+}{\tau_D}\right)^2 + \left(\frac{\tau_+}{\tau_E}\right)^2} \qquad (9)$$

$$E_{sc} = \frac{[E_o{}^2 + E_D{}^2(1 + E_D/E_q + E_o{}^2/E_D E_q)^2]^{1/2}}{(1 + E_D/E_q)^2 + (E_o/E_q)^2} \tag{10}$$

$$\psi = \arctan\{(E_D/E_o)[1 + E_D/E_q + E_o{}^2/(E_D E_q)]\} \tag{11}$$

$$E_D = \frac{k_g k_B T}{e}, \quad \text{(diffusion-limited space charge field)} \tag{12}$$

E_o = applied field (normal to grating planes)

$$E_q = \frac{4\pi e N_A}{\epsilon k_g}. \quad \text{(space charge field for complete separation of available charge)} \tag{13}$$

and the time scales are defined by

$$\tau_{di} \equiv \frac{\epsilon}{4\pi\sigma}, \quad \text{(dielectric relaxation time)} \tag{14}$$

$$\tau_E \equiv \frac{1}{k_g \mu E_o}, \quad \text{(drift time)} \tag{15}$$

$$\tau_D \equiv \frac{e}{\mu k_B T k_g^2}, \quad \text{(diffusion time)} \tag{16}$$

$$\tau_+ \equiv (sI_o + 2\gamma_R n_o + \gamma_R N_A)^{-1}, \quad \text{(modified recombination time)} \tag{17}$$

$$\tau_1 \equiv (sI_o + \gamma_R n_o)^{-1} , \tag{18}$$

where σ is the conductivity, and is given by

$$\sigma = n_o e\mu \tag{19}$$

In eqs. (17) - (19) n_o is the spatially-averaged electron density. Under normal cw conditions these approximations hold:

$$\tau_+ << \tau_{di} \tag{20}$$

$$\tau_+ \simeq (\gamma_R N_A)^{-1} \tag{21}$$

$$n_o \simeq \frac{sI(N_D - N_A)}{\gamma_R N_A} \tag{22}$$

Under uniform illumination, the space charge field during erasure is given by

$$\delta E = E_g \sin (k_g z + \omega_e t)\, e^{-t/\tau_e} , \tag{23}$$

where E_g is the initial grating amplitude and ω_e and τ_e are defined above.

There are several interesting features of the expression for the response time τ_e given by eq. (8). First it is obvious that the erase time is a complicated function of grating period, applied field strength, temperature, etc., in addition to being proportional to the dielectric relaxation time τ_{di}. In the classical case of a charged dielectric sample, (e.g. a capacitor) the response time is just τ_{di}, which can be considered as the intrinsic RC time constant of the material. The added terms in eq. (8) are due to the periodicity of the charge pattern in the crystal; note that when $k_g \to 0$, eq (8) reduces to $\tau_e = \tau_{di}$. Even when a grating is present, there are important limits for which the correction terms are small, and $\tau_e \simeq \tau_{di}$. These cases will be discussed later.

III PERFORMANCE PARAMETERS

A. Response Time

The complete expression for the response time τ_e is given in eq. (8). As indicated earlier, there are important limits when $\tau_e \simeq \tau_{di}$, so we will first consider the dependence of τ_{di} on important material parameters. By combining eqs. (14), (19) and (22), we obtain

$$\tau_{di} = \frac{\varepsilon\gamma_R}{4\pi e\mu s I_o}\ \frac{N_A}{N_D-N_A}$$

$$=\left(\frac{\varepsilon\gamma_R}{4\pi e\mu s}\right)\frac{1}{I_o}\ \frac{1}{R} \qquad (24)$$

The quantity in parentheses in eq. (24) can be considered as a material figure of merit, having units of energy/unit area. Once a material is chosen, the only experimental control over this quantity is through its variation with temperature (through μ and γ_R) and with wavelength (through s). However, the quantity R can be varied over many orders of magnitude by reduction or oxidation of a given sample. It is clear from eq. (24) that increasing R through chemical reduction can significantly reduce τ_{di}. Values of R as high as 10 are not hard to achieve in many cases, and in some materials (e.g. BSO) values of R on the order of 10^3 are typical [13]. Note also the I_o^{-1} dependence in eq. (24), indicating the direct relation between speed and irradiance.

Returning to eq. (8), we now wish to consider how the simple relationship $\tau_e \simeq \tau_{di}$ is modified by the presence of a volume space charge grating in the sample. By examination of the time constants entering into eq. (8), we find that $\tau_e \simeq \tau_{di}$ is still a valid approximation when $\tau_+ \ll \tau_D, \tau_E$. This condition is approximated when either of the following conditions hold: (1) the crystal is oxidized (τ_+ is minimized), or (2) the applied electric field is small (large τ_E), and diffusion is slow (large τ_D) due to low temperature or large grating period. This is shown more clearly in figures 1-3, which are log-log plots of τ_e (normalized to τ_{di} for R = 1) as a function of the reduction ratio R, for several values of applied electric field. The relationship $\tau_e = \tau_{di}$ corresponds to a straight line with slope -1. We see first that this relationship is most closely approached for $E \approx 0$, especially when $R \lesssim 100$. When E is zero, there is an increase in τ_e, especially in highly reduced crystals, and for small valves of the grating period Λ_g. As pointed out by Kukhtarev [6], there are also certain conditions (low mobility, high temperature) where an increase in E can lead to a decrease in τ_e. However, these conditions are not generally attained in typical experiments.

B. Sensitivity

Several definitions of sensitivity have appeared in the literature. The two most common are: (1) the energy density required to write a grating with 1 percent diffraction efficiency, and (2) the incremental change in refractive index per unit of absorbed energy. In both cases, the magnitude and direction of the space charge field must be known in order to calculate the induced refractive index change. However, there are certain experimental situations, (e.g. domination of diffusion) where the space change field is nearly invariant from material to material; thus, no new information is provided by including E_{sc} in the definition. In other situations, the space charge field may be different from material to material, but accurate knowledge of its value may not be important.

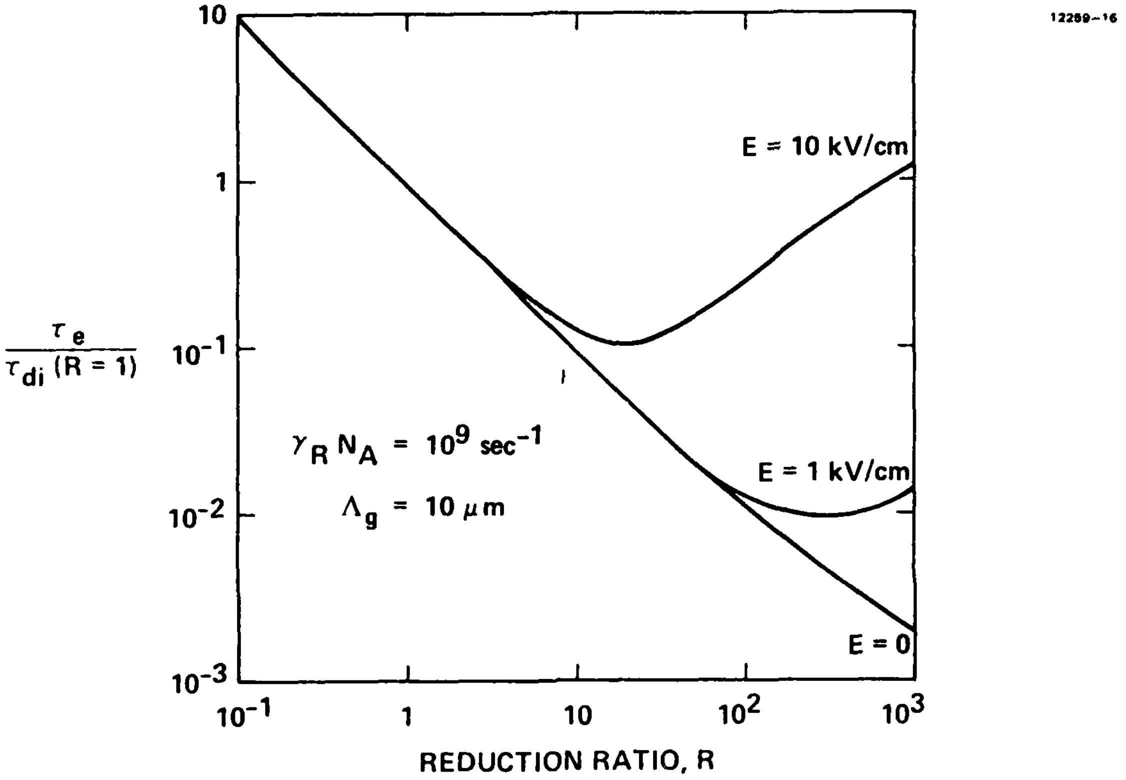

Figure 1. Normalized erase time versus reduction ratio for indicated recombination rate and grating spacing.

In this work we would like to propose a different definition for the write/erase sensitivity. Since we know τ_e is proportional to τ_{di}, and τ_{di} varies as I^{-1}, we define the write sensitivity S_W to be the energy density required to write a grating to $(1-e^{-1})$ of its final value of space charge field. Similarly, the erase sensitivity Se is the energy density required to erase a grating to e^{-1} of the initial space charge field. Since in this mode the write time is equal to the erase time, we can write:

$$S = S_W = S_e = I_o \tau_e \tag{25}$$

Note that the sensitivity (in J/cm^2) is numerically equal to the response time when $I_o = 1$ w/cm^2. In the limit where $\tau_e \approx \tau_{di}$, the sensitivity S is given by

$$S = \left(\frac{\varepsilon \gamma_R}{4\pi e \mu s}\right) \frac{1}{R} . \tag{26}$$

Our definition results in a very simple expression for S, which includes the same material figure of merit (given in parentheses) which appears in the expression for τ_{di}. Of course since no information on the induced space charge field or refractive index change is contained in eq. (26), some care has to be taken when optimizing the sensitivity. For example a low value of ε is favored for improved sensitivity, but materials with low values of ε have small values of electro-optic coefficient, and may thus be inefficient. Of course this is accounted for in the other definitions of sensitivity, but other information is lost.

C. Efficiency

The diffraction efficiency for Bragg scattering from a volume phase grating is given by

$$\eta = e^{-\frac{\alpha L}{\cos\theta}} \sin^2 \left(\frac{\pi \Delta n L}{\lambda \cos\theta}\right), \tag{27}$$

where α is the absorption coefficient, L is the interaction length, θ is the bragg angle, and Δn is the amplitude of the spatially varying refractive index. In materials with $\alpha L \ll 1$ and with $\Delta n \ll \lambda / L$, we obtain

$$\eta \simeq \left(\frac{\pi \Delta n L}{\lambda \cos\theta}\right)^2. \tag{28}$$

In a ferroelectric with the grating wave vector along the c-axis, we can write

$$\Delta n = 1/2\; n^3 r\, E_{sc}, \tag{29}$$

where the electro-optic coefficient r is equal to r_{13} or r_{33}, depending on the polarization direction of the readout beam. In a cubic crystal or in a ferroelectric with a different grating orientation, the component of r may be different and other terms may be required [4, 13]. For the simple case considered here, we have

$$\eta \simeq \left(\frac{\pi n^3 L}{2\lambda\cos\theta}\right)^2 r^2 E_{sc}^2 \quad . \tag{30}$$

In experiments in which no applied field is used and the bulk photovoltaic effect is absent (e.g. in a cubic crystal) or is suppressed (no external current path supplied), then only diffusion can contribute to the space charge field. If we further assume that $E_d \ll E_q$ as is typical in all but highly reduced materials, then

$$E_{sc} = E_D = \frac{k_B T}{e} k_g, \tag{31}$$

i.e. E_{sc} is invariant from material to material. Similarly, if $E_q \gg E_o \gg E_D$, then $E_{sc} \simeq E_D$, and again the space charge field is invariant. In these limits, the efficiency for a given material is determined entirely by the electro-optic coefficient, except for the smaller variation due to the n^6 term. Clearly, the most favored materials for achieving high efficiency are those with large values of electro-optic coefficient.

IV APPLICATION TO DFWM IN SPECIFIC MATERIALS

The concepts of response time, sensitivity and efficiency are all defined with respect to the writing or erasure of a grating in a small volume element where the intensity is known. The modification of those parameters for DFWM applications is not straightforward, and requires the solution of coupled wave equations which can not be considered in the steady state if the time dependence is desired. In the typical four-wave mixing geometry, the solutions show that the nonlinear reflectivity and response times are strongly influenced by beam coupling. An example of such an analysis in the steady state is the work of Fischer, et al [15].

In this study, we will continue to use concepts derived for grating formation and decay, because the simple expressions we have obtained are expected to be qualitatively accurate, and they provide useful insight into the relative performance of different materials.

In Table I we have listed measured values of grating response time and sensitivity, as well as DFWM reflectivity for a number of materials. Since the response time is given for $I_0 = 1$ w/cm^2, it is numerically equal to the sensitivity. The values in the table are chosen to be representative of commonly available materials; clearly a large range in values can be obtained, depending on orientation, reduction, etc. The values marked with an asterisk were measured at Hughes Research Laboratories. We have also listed the dominant electro-optic coefficient for each material, because of its relevance to the efficiency or DFWM reflectivity.

The most sensitive (and fastest) materials in Table I are those which are most highly reduced (e.g. BSO, BGO). Furthermore the largest values of DFWM reflectivity are observed in those materials with the largest electro-optic coefficients. This is because in most DFWM experiments (with the exception of BSO, BGO), no applied field was used, and diffusion was the dominant transport mechanism.

The important conclusion which can be drawn from the results presented here is that the most favorable materials are those with the

Table Comparison of photorefractive materials

MATERIAL	WRITING ENERGY (J/cm^2)	RESPONSE TIME AT 1 w/cm^2 (sec)	DOMINANT ELECTRO-OPTIC COEFFICIENT (10^{-12} m/v)	DFWM REFLECTIVITY
$LiNbO_3$	0.01	--	$r_{33} = 30$	10^{-2}*
$LiNbO_3$:Fe	0.2	--	$r_{33} = 30$	--
$BaTiO_3$	0.5	0.5	$r_{51} = 1640$	20*
$KNbO_3$	--	0.5	$r_{33} = 50$	--
$KNbO_3$:Fe	--	0.1	$r_{42} = 380$	10^{-1}
SBN	--	(0.5)	$r_{33} = 100\text{-}800$	(-1)
BSO,BGO	0.03	0.03*	$r_{41} = 5$	10^{-3}*

*Measured at HRL

largest electro-optic coefficient, and which can be reduced to values of $R \gtrsim 100$. For example, the reduction state in typical commercially available $BaTiO_3$ is not known, but values of R much greater than unity are not likely, because this material is grown in an oxygen atmosphere. Thus, if the reduction ratio could be increased into the range 10^2 - 10^3, significant improvements in the response time and sensitivity could be obtained, with little or no loss in efficiency.

References

[1] J. Feinberg and R.W. Hellwarth, Opt. Lett. 6, 519 (1980).

[2] J.O. White, M. Cronin-Golomb, B. Fischer, and A. Yariv, Appl. Phys. Lett. 40, 450 (1982).

[3] M. Cronin-Golomb, B. Fischer, J. Nilsen, J.O. White, and A. Yariv, submitted to..........................(1982).

[4] J. Feinberg, D. Heiman, A.R. Tanguay, Jr., and R.W. Hellwarth, J. Appl. Phys. 51, 1297 (1980).

[5] P.N. Gunter, Opt. Lett. 7, 10 (1982).

[6] N.V. Kukhtarev, Sov. Tech. Phys. Lett. 2 438 (1976).

[7] V.L. Vinetskii and N.V. Kukhtarev, Sov. Phys. Solid State 16 2414 (1975).

[8] N.V. Kukhtarev, V.B. Markov, S.G. Odulov, M.S. Soskin and V.L. Vinetskii, Ferroelectrics 22 949 (1979).

[9] V.L. Vinetskii and N.V. Kukhtarev, Sov. J. Quantum Electron. 8 231 (1978).

[10] N. Kukhtarev, V. Markov, and S. Odulov, Opt. Comm. 23 338 (1977).

[11] N. Kukhtarev and S. Odulov, Opt. Comm. 32, 183 (1980).

[12] C.-T. Chen, D.M. Kim and D. von der Linde, IEEE J. Quantum Electron. QE-16, 126 (1980).

[13] M. Peltier and F. Micheron, J. Appl. Phys. 48 3683 (1977).

[14] R. Orlowski and E. Krätzig, Solid State Comm., 27 1351 (1978).

[15] B. Fischer, M. Cronin-Golomb, J.O. White and A. Yariv, Opt. Lett. 6 519 (1981).

APPENDIX C

Optimal Properties of Photorefractive Materials for Optical Data Processing

George C. Valley
Marvin B. Klein

Hughes Research Laboratories
3011 Malibu Canyon Road
Malibu, CA 90265

ABSTRACT

The charge transport model of photorefractivity is used to evaluate four figures of merit that can be used to characterize the performance of photorefractive materials. The figures of merit are the steady-state index change, the response time, the energy per area to write a one percent diffraction efficiency grating, and the photorefractive sensitivity, or index change per absorbed energy per unit volume. These indices are evaluated as a function of grating period and applied external electric field for $Bi_{12}SiO_{20}$, a fast material with a relativelly small electro-optic coefficient and $BaTiO_3$, a slower material with a much larger electro-optic coefficient. Methods for optimizing the materials are discussed.

A. INTRODUCTION

Photorefractive materials such as lithium niobate ($LiNbO_3$), potassium niobate ($KNbO_3$), barium titanate ($BaTiO_3$), strontium barium niolate (SBN) and bismuth silicon oxide ($Bi_{12}SiO_{20}$) are attractive new candidates for real-time optical data processing, (ODP); in the past few years, many ODP operations have been demonstrated in these materials. Reversible holographic storage in $LiNbO_3$ was the first ODP operation demonstrated.[1-3] More recently, edge enhancement [4,5] and correlation-convolution operations [6,7] have been demonstrated. Photorefractive materials have also been used for phase conjugation via degenerate four-wave mixing.[8-12] Finally, under some conditions photorefractive materials can be used as optical image amplifiers.[13-16]

The promise of photorefractive materials for ODP is substantial. A large number of parallel operations can be processed in a single crystal. Photorefractive materials can store optical holograms for time scales of hours to years, depending on the dark conductivity. Gains up to a factor of 15 have been observed in $LiNbO_3$,[13] and gains are likely to be higher in $BaTiO_3$ and SBN. Operation on nanosecond time scales has been demonstrated [17-19] with Q-switched pulses from doubled YAG lasers. Finally, the requirements on write and erase energy density in some photorefractive materials (e.g., BSO[4]) are comparable to the best photographic plates (50 to 100 $\mu J/cm^2$).

There are two major factors that limit widespread application of photorefractive materials at present. First, some of the most promising materials (e.g., $BaTiO_3$, SBN and $KNbO_3$) are not widely available in large samples with high optical quality. Second, the crystals that are available are not optimal in all respects. For instance, in order to demonstrate high speed, low write energy, long memory or large gain, it is necessary to use several different types of materials. The purpose of this paper is to compare photorefractive materials for several different applications and to determine optimal properties for ODP. To do this, we first give a brief description of the charge transport model of grating formation and erasure. Then we define four separate figures of merit for ODP operations and evaluate them using the charge transport model. Finally, we compare two photorefractive materials (BSO and $BaTiO_3$) that each have certain optimal properties and suggest methods for improving the materials. For a discussion of additional figures of merit, other materials and applications, the reader is referred to the recent comprehensive review by Gunter.[26]

B. CHARGE TRANSPORT MODELS

Two separate models for describing charge transport in photorefractive materials have been formulated. The hopping model[15] assumes that carrier transport occurs via hopping from a filled donor site to a neighboring empty trap. The band transport model [13,14] assumes that electrons (or holes) are optically excited from filled donor (or acceptor) sites to the conduction (or valence) band where they migrate to dark regions in the crystal by drift or diffusion before recombining into an empty trap (see Figure 1). In both models the transported charges result in an ionic space charge grating which is, in general, out of phase with the incident irradiance (see Figure 2). The space charge grating is balanced by a periodic space charge electric field in accordance with Poisson's equation. This space charge field modulates the refractive index through the electro-optic effect. The band transport model has been developed to a greater degree and is in wider use in the literature; this is the model which we will use for our analysis. A detailed comparison of the band-transport and hopping model is beyond the scope of this paper.

A mathematical description of the grating formation process is given by the equations developed most fully by Kukhtarev [13,19,20] and co-workers (see also earlier work by Amodei[21] and others[22]):

$$\frac{\partial n}{\partial t} - \frac{\partial N_D^+}{\partial t} = \frac{1}{e}\frac{\partial j}{\partial z} \qquad \text{(continuity)} \qquad (1)$$

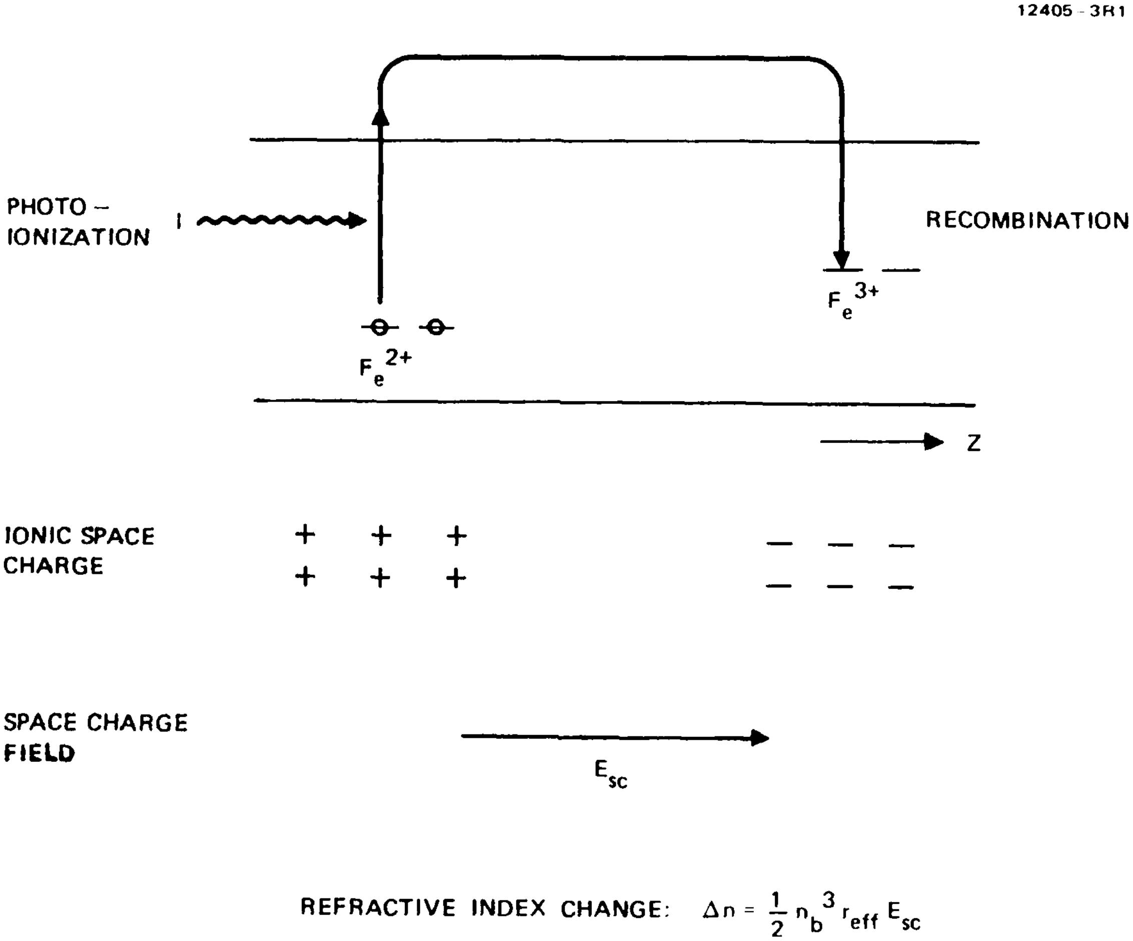
12405-3R1
PHOTO – IONIZATION
I
RECOMBINATION
F_e^{3+}
F_e^{2+}
Z
IONIC SPACE CHARGE
SPACE CHARGE FIELD
E_{sc}
REFRACTIVE INDEX CHANGE: $\Delta n = \frac{1}{2} n_b^3 r_{eff} E_{sc}$

Figure 1. Schematic of the charge transport model of photorefractivity. Photo ionization excites an electron from Fe^{2+} which drifts or diffuses to a new location and is trapped at Fe^{3+}. This leads to an ionic space charge and an internal electric field that modulates the index of refraction.

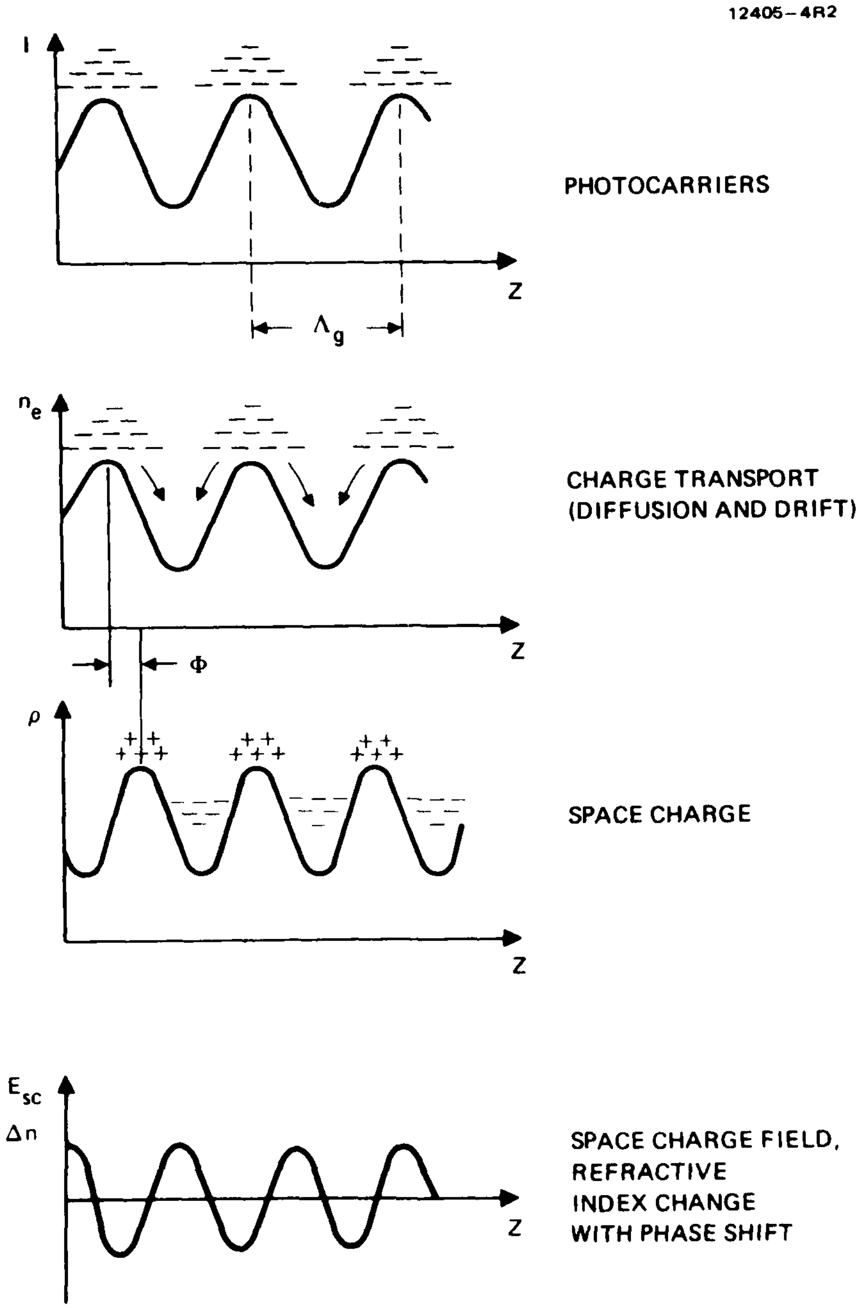
12405–4R2
I
Z
Λ_g
PHOTOCARRIERS
n_e
Z
Φ
CHARGE TRANSPORT
(DIFFUSION AND DRIFT)
ρ
Z
SPACE CHARGE
E_{sc}
Δn
Z
SPACE CHARGE FIELD,
REFRACTIVE
INDEX CHANGE
WITH PHASE SHIFT

Figure 2. Gratings in a photorefractive material. Note that the space charge pattern is displaced from the photocarrier pattern. Also, the space charge field is 90° out of phase with the space charge.

$$\frac{\partial N_D^+}{\partial t} = sI(N_D-N_D^+) - \gamma_R n N_D^+ \quad \text{(rate equation)} \qquad (2)$$

$$j = e\mu n E - k_B T \mu \frac{\partial n}{\partial z} \quad \text{(current equation)} \qquad (3)$$

$$\frac{\partial E}{\partial z} = \frac{4\pi e}{\varepsilon} (n+N_A-N_D^+) \;, \quad \text{(Poisson's law)} \qquad (4)$$

where n is the electron number density,

N_D is the total number density of dopants (Fe for example, ionized and neutral: N_D is a constant),

N_D^+ is the number density of ionized donors (Fe^{3+} for example),

N_A is the number density of negative charges that compensate for the charge of N^+ under dark conditions (N_A is a constant of the crystal),

N_D-N^+ is the number of neutral (filled) donors,

j is the current density,

s is the photoionization cross-section,

I is the irradiance of the optical wave,

γ_R is the two-body recombination rate coefficient,

μ is the mobility,

E is the total electric field,

k_B is Boltzmann's constant,

T is the temperature,

e is the charge on the electron, and

ε is the static dielectric constant.

One important parameter which has a strong influence on the performance of photorefractive materials is the reduction ratio, defined as

$$R = \frac{N_D-N_A}{N_A} = \frac{N_D}{N_A} - 1 \quad .$$

This parameter is the ratio of filled to empty donor states under dark conditions.

The optical irradiance, I, in Equation (2) is assumed to be of the form

$$I = I_0 \, (1 + m \cos k_g z) \qquad (5)$$

where m is the modulation index, k_g is the grating wavenumber and I_0 is the average irradiance. For two copolarized input waves of irradiances I_1 and I_2,

$$m = \frac{2 \, (I_1 \, I_2)^{1/2}}{I_1 + I_2} \quad . \qquad (6)$$

For erasure with a uniform beam, m = 0.

Equations (1) through (6) must be supplemented by Maxwell's equations for the optical field in the crystal and an electro-optic relation between the space charge field and the change in the crystal refractive index, Δn. Thus,

$$\Delta n = 1/2 \; n_b^3 \, r_{eff} \, E \quad , \qquad (7)$$

where n_b is the background refractive index and r_{eff} is the effective electro-optic coefficient. Equations (1) through (7) may be modified to include dark conductivity and the bulk photovoltaic effect,[14] but these effects are neglected here. The set of equations also does not consider secondary trapping levels or photorefractive centers.[17, 23, 24]

Equations (1) through (4) can be solved with two approximations: linearization in the grating modulation index and the quasi-steady approximation in the zeroth-order electron number density, n_0.[20] Using these approximations and omitting those terms that are important only for high irradiance (MW/cm^2) nansecond pulses,[25] we obtain the space charge field, δE:

$$\delta E = m E_{sc} \left[-\cos(k_g z + \Psi) + e^{-t/\tau_e} \cos(k_g z + \omega t + \Psi) \right] \quad . \qquad (8)$$

The transient response has an overdamped oscillatory behavior with a response time,

$$\tau_e = \tau_{di} \frac{(1 + \tau_R/\tau_D)^2 + (\tau_R/\tau_E)^2}{[1 + \tau_R \tau_{di}/(\tau_D \tau_I)](1 + \tau_R/\tau_D) + (\tau_R/\tau_E)^2(\tau_{di}/\tau_I)}, \quad (9)$$

and a frequency,

$$\omega = \frac{1}{\tau_{di}} \frac{(\tau_R/\tau_E)(\tau_{di}/\tau_I - 1)}{(1 + \tau_R/\tau_D)^2 + (\tau_R/\tau_E)^2} . \quad (10)$$

In addition, the amplitude, E_{sc}, is given by

$$E_{sc} = E_q \left[\frac{(E_o^2 + E_D^2)}{E_o^2 + (E_D + E_q)^2}\right]^{1/2} , \quad (11)$$

and the phase shift, Ψ, between I and δE is given by

$$\tan \Psi = \frac{E_D}{E_o} \left(1 + \frac{E_D}{E_o} + \frac{E_o^2}{E_D E_q}\right) , \quad (12)$$

with

E_o = applied field (normal to grating planes),

$E_D = \frac{k_B T k_q}{e}$ (diffusion field), and

$E_q = \frac{4\pi e N_A}{\varepsilon k_g}$ (limiting value of the space charge field).

Finally, the time scales are defined by

$\tau_{di} = \frac{\varepsilon}{4\pi e \mu n_o}$ (dielectric relaxation time),

$\tau_E = \frac{1}{k_g \mu E_o}$ (drift time),

$\tau_D = \frac{e}{\mu k_B T k_g^2}$ (diffusion time),

$\tau_R = \frac{1}{\gamma_R N_A}$ (recombination time), and

$\tau_I = \frac{1}{sI_o + \gamma_R n_o}$ (inverse of sum of photoproduction and ion recombination rates),

and the zeroth-order electron number density is given by

$$n_o = \frac{sI(N_D - N_A)}{\gamma_R N_A} \quad . \tag{13}$$

For erasure by uniform illumination the field is given by

$$\delta E = E_g \cos k_g z \, e^{-t/\tau_e} \quad , \tag{14}$$

where E_g is the initial amplitude and τ_e is same response time obtained for writing a grating.

C. FIGURES OF MERIT FOR ODP

1. Steady-State Index Change

The steady-state change in the refractive index (also called maximum refractive index[26]) is defined as the index change reached after illumination for a time long compared to the response time, τ_e. The index is related directly to the space charge field through

$$\Delta n_{ss} = 1/2 \; n_b^3 \; r_{eff} \; E_{sc} \quad . \tag{15}$$

The background index, n_b, is typically 2.5 for most photorefractive materials, so materials dependence is in the product, $r_{eff} \, E_{sc}$. There are three limits for E_{sc}.

a. $E_{sc} \approx E_D$. This occurs when $E_0 = 0$ (no applied field) and $E_D < E_q$. For materials with moderate values of dielectric constant ($LiNbO_3$, $LiTaO_3$, BSO, BGO; $\varepsilon \approx 50$) and typical trap densities Λ_g ($N_A \approx 10^{16}$ cm^{-3}), E_D is smaller than E_q for grating periods greater than about 0.5 μm. In materials with large dielectric constants ($BaTiO_3$, $KNbO_3$, SBN) and similar trap densities, $E_D < E_q$ occurs for $\Lambda_g > 1.5$ to 5 μm. For the case of $E_D < E_q$, the steady state index is proportional to r_{eff} since E_D does not depend on material parameters.

b. $E_0 > E_D$ and $E_0 < E_q$. E_{sc} is proportional to E_0, and the only materials dependence of the steady state index is through r_{eff}, as in case (a).

c. E_0 or $E_D > E_q$. In this case, $E_{sc} \approx E_q$ and the materials dependence of the steady state index is in the product, $r_{eff} N_A/\varepsilon$. For most materials, $r_{eff} \sim \varepsilon$, and thus, the steady state index, depends primarily on the trap number density, N_A. Note that making N_A larger in order to increase the steady state index may not be effective if it changes the dependence from case (c) to case (a) or (b). Also, increasing N_A may not be desirable because this increases the response time, as discussed below.

2. Response Time

The response time is a useful figure of merit for applications in which available energy limits the illumination time, or in which the grating must be written or erased in a set time scale. As shown in Equation (9), the response time is given by the dielectric relaxation time multiplied by a factor that takes into account variations in the conductivity due to the spatially varying electron number density. In order to understand the materials dependence of the response time, consider the dielectric relaxation time, $t_{di} = \varepsilon/\sigma$, where σ is the conductivity given by $\sigma = e\mu n_0$. Using Equation (13) for the electron number density, we obtain

$$\tau_{di} = \left[\frac{\varepsilon\gamma_R}{e\mu s}\right]\left[\frac{N_A}{N_D - N_A}\right]\frac{1}{I_0} \quad . \tag{16}$$

The first factor in brackets is a material figure of merit. It is essentially a constant for a given material, although there is some control over the dielectric constant, ε, through the crystal orientation and control over the photoionization cross-section, s, through choice of operating wavelength. The ratio $N_A/(N_D - N_A)$, the inverse of the reduction ratio, is not a fundamental property of a given photorefractive material and can be varied in non-destructive processing of existing crystals (reduction or oxidation).

3. Energy Per Area to Write a 1% Grating

A third figure of merit, which is widely used, is the energy per unit area required to write a grating of 1% diffraction efficiency in a crystal 1 mm thick. This figure of merit is useful in ODP for applications where a large efficiency is not required. It allows comparison of fast materials with small values of electro-optic coefficient with slow materials having large values of electro-optic coefficient. The figure of merit has the disadvantage that some materials never reach a 1% diffraction efficiency in 1 mm and that the diffraction efficiency depends on the energy per unit area only for times that are short compared to the response time.

The energy per unit area to write a 1% grating is derived as follows. The diffraction efficiency is given by[27]

$$\eta = \exp(-\alpha\ell/\cos\theta)\sin^2\left(\frac{\pi\ell}{\lambda}\frac{\Delta n}{\cos\theta}\right) \quad , \tag{17}$$

where α is the absorption coefficient, ℓ is the length of the crystal, θ is half the Bragg angle and λ is the vacuum wavelength. If we ignore the oscillations at frequency ω (Equation (10)), the index change can be written as

$$\Delta n = 1/2\ n_b^3 r_{eff} E_{sc} m\ [1 - \exp(-t/\tau_e)]\ . \tag{18}$$

For $t \ll \tau_e$,

$$\Delta n = 1/2\ n_b^3 r_{eff} E_{sc} m\ t/\tau_e\ . \tag{19}$$

And since τ_e is proportional to τ_{di}, which is inversely proportional to I_O, one can set $n = 1\%$, $\ell = 0.1$ cm and solve for $I_O t$, which is the energy per area required to write a 1% grating. For cases in which $E_{sc} = E_O$ or $E_{sc} = E_D$, Δn is proportional to r_{eff}/τ_e, so that materials with large electro-optic coefficients and long response times can have similar 1% energies per area to materials with small electro-optic coefficients and short response times.

4. Photorefractive sensitivity

The photorefractive sensitivity is defined as the index change per absorbed energy, $\Delta n/(\alpha I_O t)$.[26] The photorefractive sensitivity is a useful figure of merit because it tells how well a material uses a given amount of optical energy. Alternatively, it allows comparison of materials with different absorption coefficients on an equal basis. Since the response time, τ_e, can be written as the dielectric relaxation time times a function of the grating period and applied field, $f(\Lambda, E_O)$, Equation (18) can be used to write the photorefractive sensitivity as

$$\frac{\Delta n}{\alpha I_O t} = 1/2\ n_b^3 \frac{r_{eff}}{\epsilon} E_{sc}\ me\mu\tau_R\ f(\Lambda, E_O)\ .$$

Since n_b and r_{eff}/ϵ are roughly the same in all photorefractive materials,[26] and since E_{sc} is often independent of material properties (for $E_q > E_D$ or $E_q > E_o$), the photorefractive sensitivity is mainly determined by the mobility, μ, and the recombination time, τ_R. Large mobilities and long recombination time are desirable because these properties allow the electrons to diffuse or drift longer distances before they recombine. The mobility and recombination coefficient are properties of a given crystal that appear difficult to modify; however, the recombination time can be increased by decreasing the number density of traps in the material, which is sometimes possible with existing crystals. Note that decreasing N_A also lowers E_q, which means that this limiting space charge field, $E_{sc} \approx E_q$, will be attained for smaller values of E_D or E_o.

D. Comparison of BSO and $BaTiO_3$

In order to gain a better understanding of the figures of merit introduced above, we have calculated them in detail for two attractive photorefractive materials, BSO and $BaTiO_3$. BSO is known to be a fast and sensitive material, with a relatively small electro-optic coefficient. On the other hand, $BaTiO_3$ has large electro-optic coefficients (especially $r_{41} = r_{52}$) and is highly efficient, but it is known to respond rather slowly. The materials parameters we have chosen for illustrating these figures of merit are discussed in the Section F. We use an optical wavelength of $\lambda = 0.5$ μm, extraordinary polarization [illegible] both write beams, and a 20° angle between c axis and grating wavevector. The last two parameters allow calculation [illegible] effective dielectric constant, ϵ, and the effective [illegible] coefficient. The value of 20° is a rough maximum [illegible] r_{eff}/ϵ, in $BaTiO_3$ and a common operating [illegible]

AD-A141 960 PHASE CONJUGATE OPTICS(U) HUGHES RESEARCH LABS MALIBU 3/3
CA G J DUNNING ET AL. FEB 84 RADC-TR-84-18
F19628-80-C-0185
UNCLASSIFIED F/G 20/6 NL

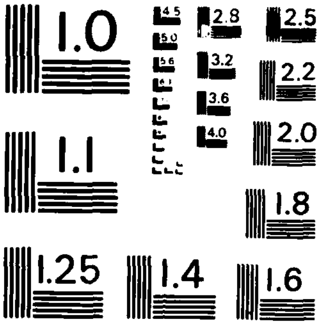
1.0
1.1
1.25
1.4
1.6
1.8
2.0
2.2
2.5
2.8
3.2
3.6
4.0
4.5
5.0
5.6

MICROCOPY RESOLUTION TEST CHART
NATIONAL BUREAU OF STANDARDS-1963-A

The steady state index as a function of grating period for BSO and $BaTiO_3$ is given in Figures 3 and 4 for an applied field of 0 and 10 kV/cm. The maxima in the $E_0 = 0$ curves at 0.5 μm for BSO and at 1.5 μm for $BaTiO_3$ correspond to the change from the $E_{sc} \approx E_q$ limit at small Λ_g to the $E_{sc} \approx E_D$ limit at large Λ_g. For $E_0 = 10$ kV/cm, BSO is approaching the $E_{sc} \approx E_0$ limit near $\Lambda_g = 10$ μm; in $BaTiO_3$, with $E_0 =$ 10 kV/cm the steady state index increases linearly in Λ_g, because $E_0 > E_q$ even at $\Lambda_g = 10$ μm. Note finally that the steady state index in $BaTiO_3$ is 20 to 50 times larger than that in BSO.

Corresponding curves for the response time at an irradiance of 1 W/cm^2 are given in Figures 5 and 6. Note that for BSO the response time decreases with grating period while for $BaTiO_3$ the response time increases with Λ_g. Also in BSO the $E_0 = 0$ response time is shorter than at $E_0 = 10$ kV/cm, while $BaTiO_3$ shows the opposite behavior. BSO is about 1000 times faster than $BaTiO_3$, due to its larger absorption coefficient, smaller recombination coefficient, smaller dielectric constant, and despite its smaller mobility.

Figure 7 shows the energy per unit area to write a 1% diffraction efficiency grating in a 1 mm thick crystal. Since the energy per area is proportional to the response time divided by the steady state index, the requirement for both BSO and $BaTiO_3$ can be plotted on the same scale.

Figure 8 shows the photorefractive sensitivity or index change per energy per volume input to the crystal. Since the absorption coefficient ratio for our illustrative parameters for $BaTiO_3$ and BSO is 1.6/0.3 = 5.3, the curves in Figure 8 are a factor of 5.3 closer than those in Figure 7. For small grating periods the photorefractive sensitivity of $BaTiO_3$ exceeds BSO, while above $\Lambda_g = 1$ μm BSO is more sensitive.

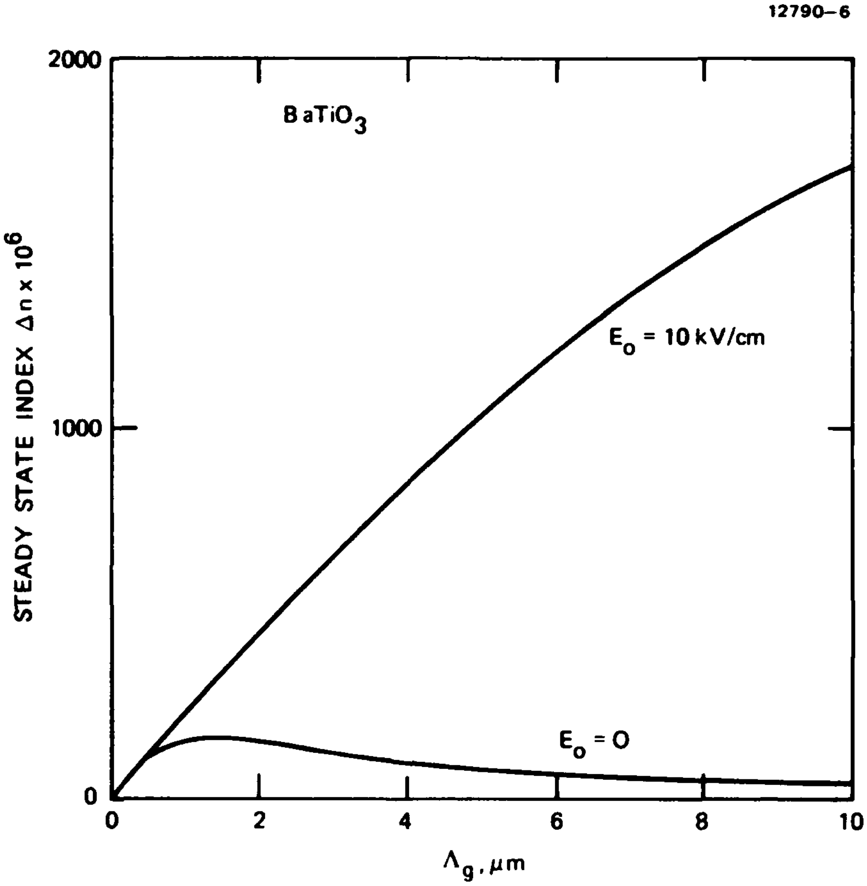

Figure 3. Steady state index change in $BaTiO_3$ as a function of grating period for applied fields, E_O = 0, 10 kV/cm.

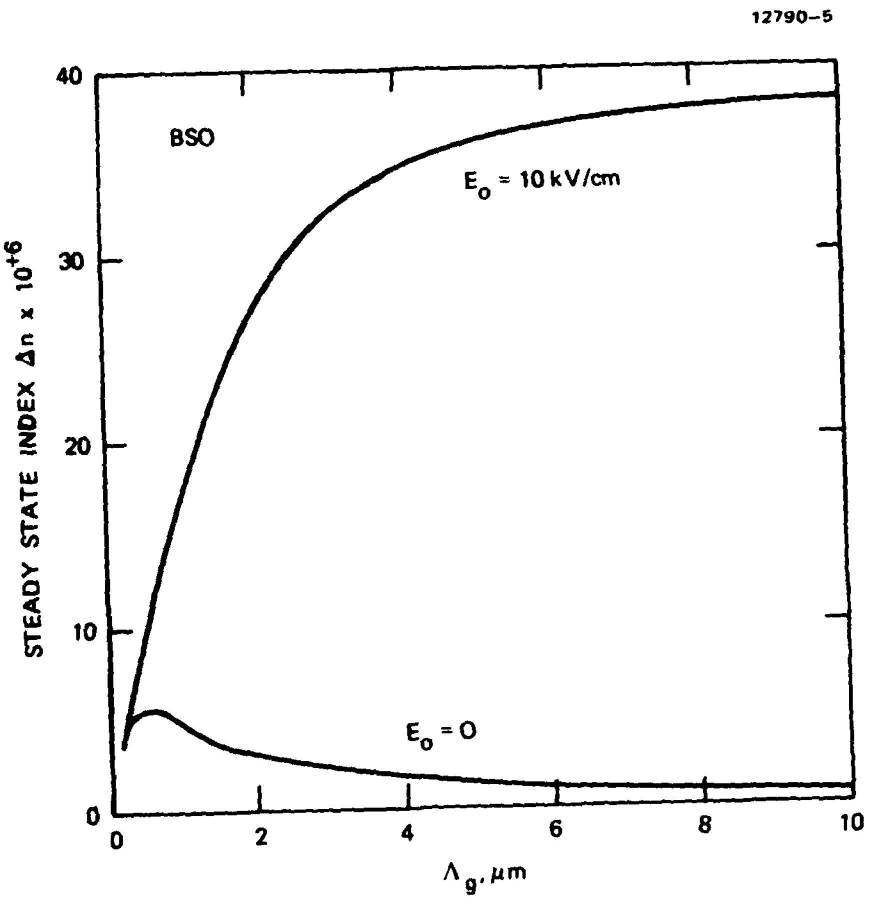

Figure 4. Steady state index change in BSO as a function of grating period for applied fields, E_O = 0, 10 kV/cm.

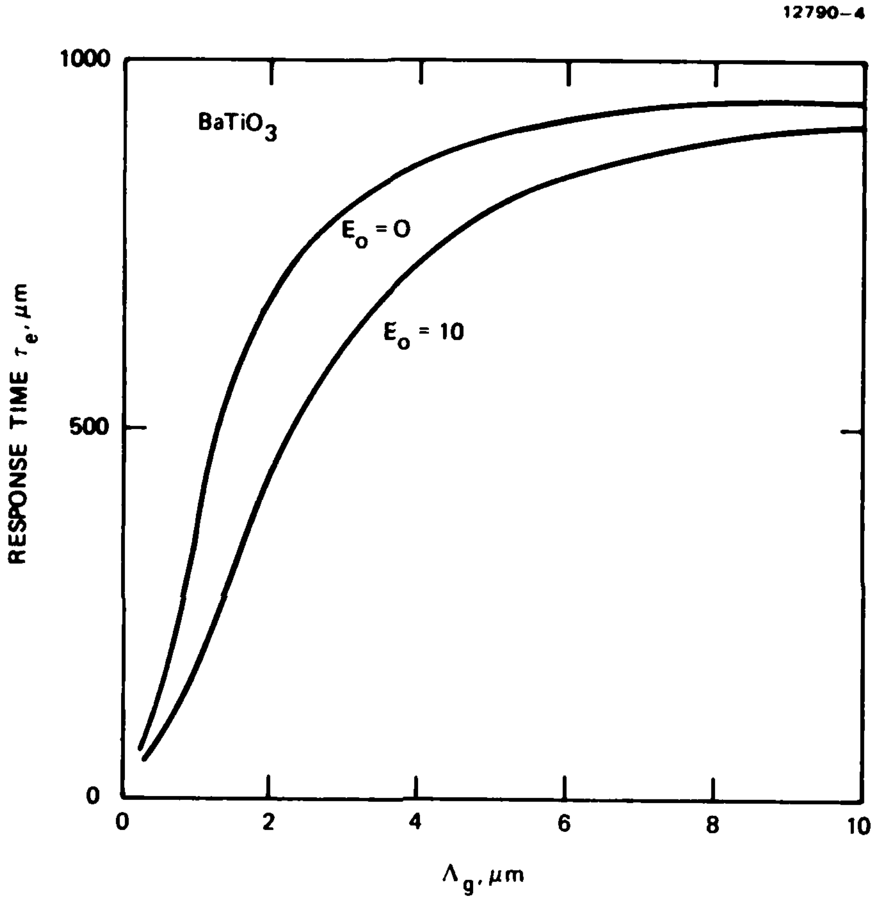

Figure 5. Response time of BaTiO$_3$ as a function of grating period for applied fields, E_O = 0, 10 kV/cm.

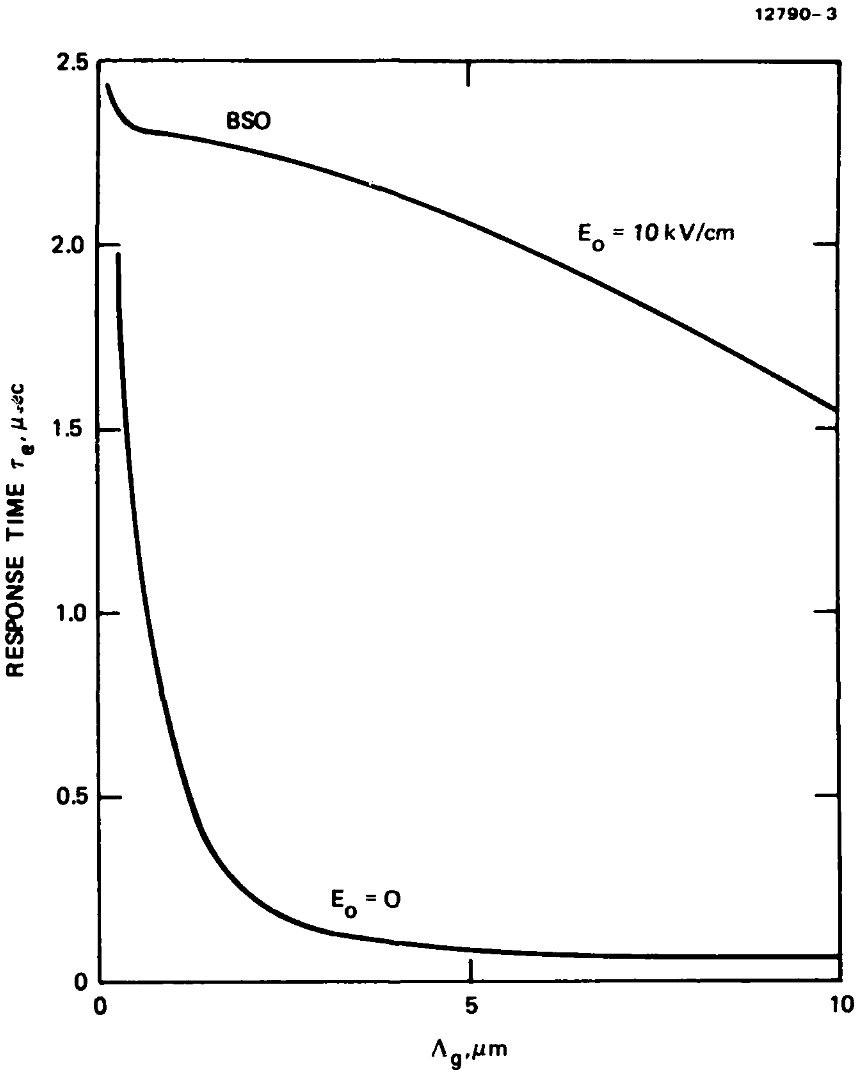

Figure 6. Response time of BSO as a function of grating period for applied fields, E_O = 0, 10 kV/cm.

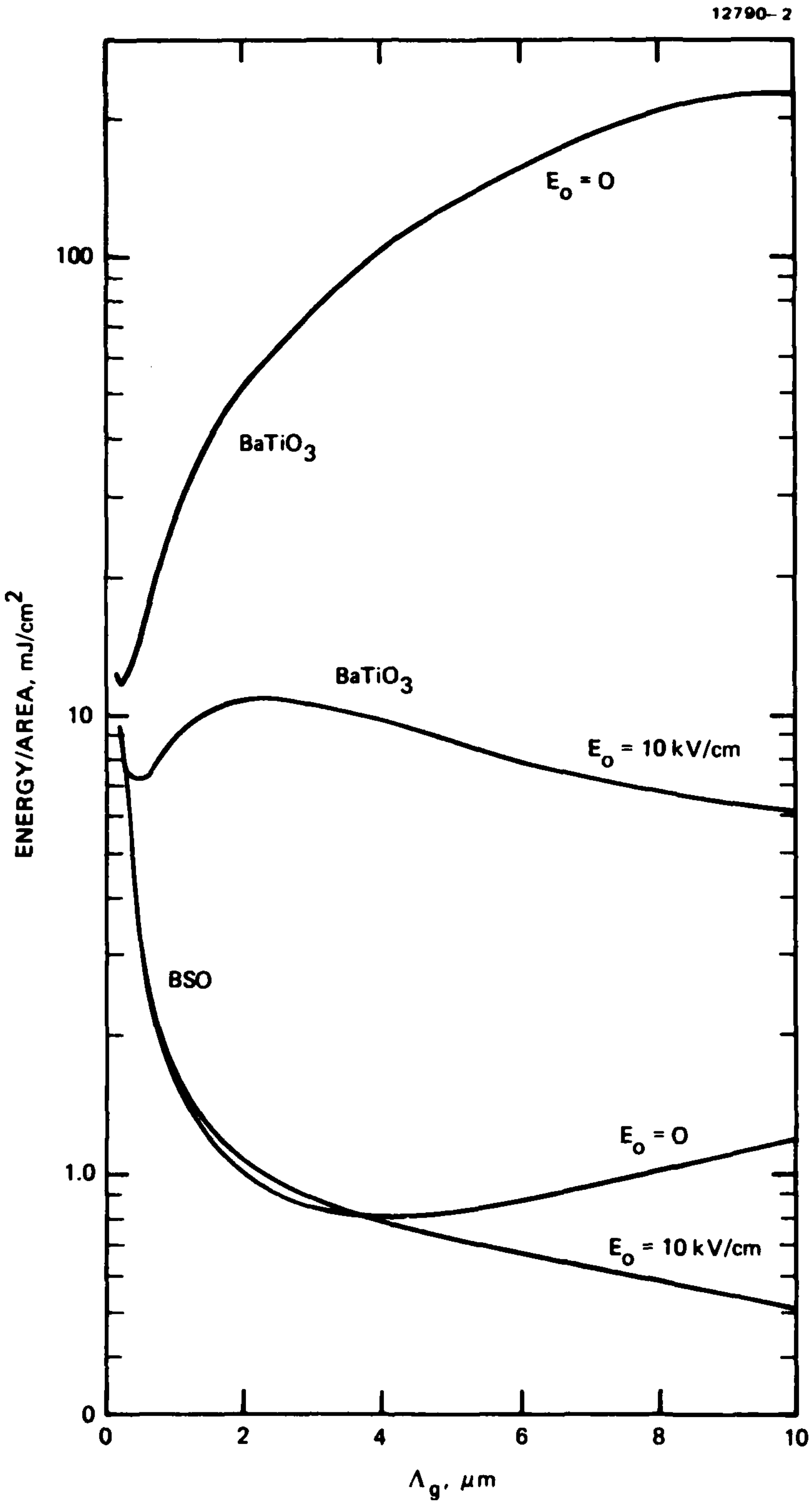

Figure 7. Energy per unit area to write a 1% diffraction efficiency grating in BSO and $BaTiO_3$ as a function of grating period for applied fields, $E_O = 0$, 10 kV/cm.

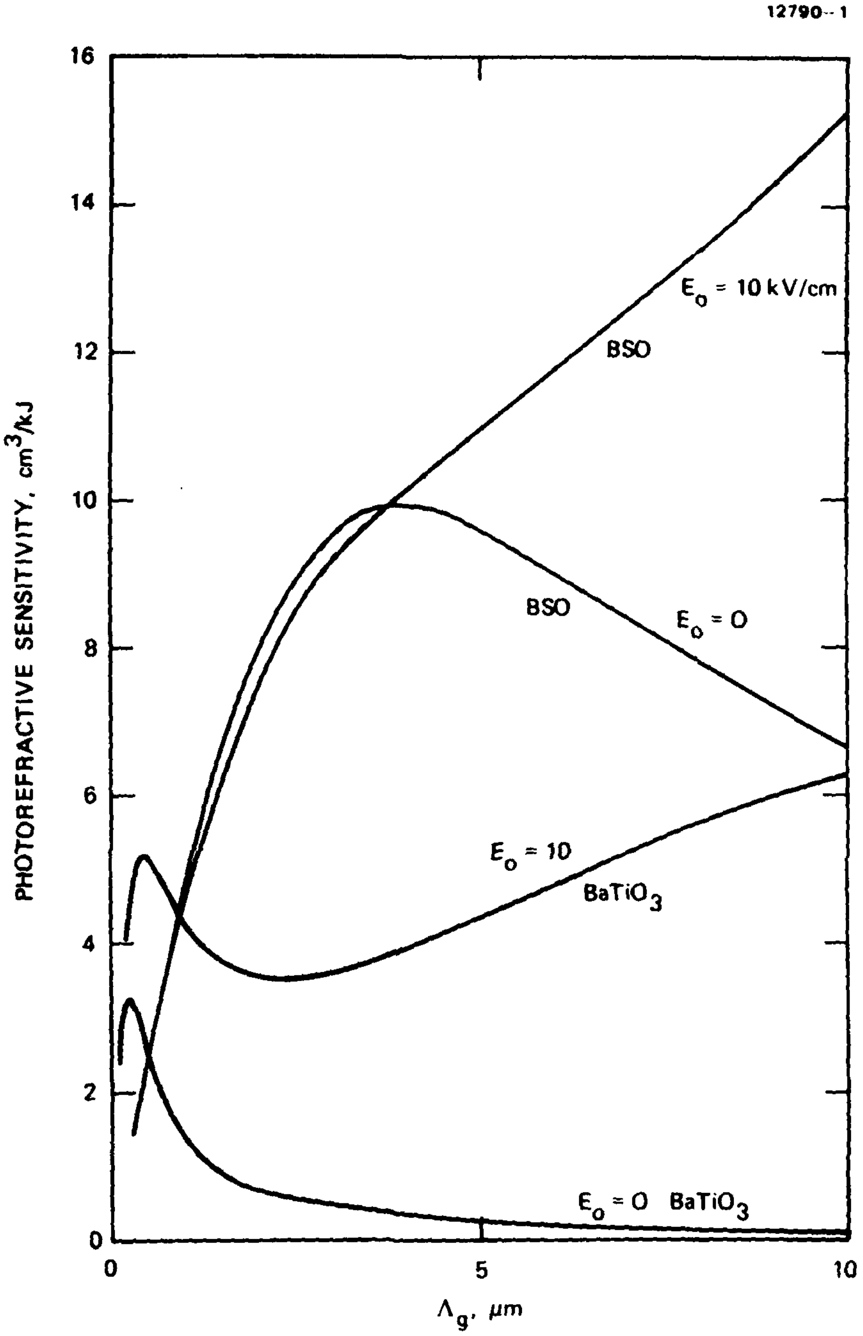

Figure 8. Photorefractive sensitivity or index charge per absorbed energy per unit volume for BSO and $BaTiO_3$ as a function of grating period for applied fields, E_O = 0, 10 kV/cm.

E. CONCLUSIONS AND OPTIMIZATION OF BSO AND $BaTiO_3$

For BSO and $BaTiO_3$ with the parameters used here, $BaTiO_3$ has by far the largest steady state index, while BSO has a much shorter response time and a somewhat smaller energy requirement for a 1% efficiency; the photorefractive sensitivities are comparable.

Other factors should also be considered in comparing these materials. Certain phase conjugation processes and image amplifiers require that the refractive index grating be shifted from the optical interference pattern by 90°. This occurs when $E_0 = 0$ or when $E_q << E_0$. Thus, BSO in the applied field limit cannot be used as an image amplifier for grating periods larger than a few microns. Some of the phase conjugation processes require that the steady-state gain, which depends directly on the steady-state index, exceed a threshold.[34] For these purposes $BaTiO_3$ may be above threshold, while BSO is below threshold.

Optimization of these materials for better performance may be possible by changing the crystal parameters, μ, N_D, N_A, s, and γ_R. Increasing the mobility is desirable for cases in which the response time is proportional to the dielectric relaxation time. Increasing the number density of filled donors, N_D, will improve both the speed of response and the energy per area requirement by increasing the absorption coefficient. N_D can be increased by reducing the crystal; i.e., increasing N_D at the expense of N_A or by increasing the number density of the dopant. The limit on useful increase in N_D is set by the total absorption. For typical 3 mm thick crystals an absorption coefficient of 3 cm^{-1} gives a transmission coefficient of 0.41. If one increased N_D in $BaTiO_3$ so that its absorption increased from 0.3 to 3 cm^{-1}, the response time and energy per area requirement would decrease a factor of 10.

Optimization of performance by varying the number density of empty traps and recombination coefficients is more complicated. On the simplest level one would want to increase N_A to increase the limiting space charge field, E_q, and one would want to decrease N_A and γ_R in order increase the recombination time, increase the carrier number density per unit irradiance, and hence decrease the dielectric relaxation time. For the energy per unit area for a 1% grating and the photorefractrive sensitivity, changing N_A would in this simple case give no effect, and decreasing γ_R would improve the response. Closer inspection of Equation (9) for the response time yields a different answer. Consider four cases at Λ_g = 1 μm: (1) BSO with E_o = 0; (2) BSO with E_o = 10 kV/cm; (3) $BaTiO_3$ with E_o = 0; and (4) $BaTiO_3$ with E_o = 10 kV/cm. In case (1)

$$\tau_e \simeq \tau_{di} \, \tau_R/\tau_D \quad .$$

Since τ_{di} is proportional to τ_R^{-1}, changing γ_R or N_A has no effect on τ_e. In case (2)

$$\tau_e \simeq \tau_I \quad ,$$

because $\tau_R/\tau_E >> 1$. Since $\tau_I \simeq 1/\gamma_R n_o$ and $n_o = \alpha I/\gamma_R N_A$, γ_R has no effect in this limit, and decreasing N_A decreases the response time. In case (3)

$$\tau_e \simeq \tau_I \, \tau_D/\tau_R \quad .$$

Substitution for τ_I and τ_R shows that τ_e is proportional to $\gamma_R N^2$. In this regime, decreasing N_A will decrease the response time and improve the 1% energy requirement and photorefractive sensitivity. In case (4)

$$\tau_e \simeq \tau_I \, \tau_E^2/\tau_R^2 \quad .$$

Here τ_e is proportional to $\gamma^2 N^3$, and decreasing N_A and γ_R is even more effective in improving performance. It should be noted that all of the conclusions in this paragraph are dependent on grating period and the other parameters of BSO and $BaTiO_3$.

F. MATERIALS PARAMETERS FOR BSO AND $BaTiO_3$

The materials parameters needed to apply the charge transport model of photorefractivity are given in Table 2. The BSO parameters are obtained from the work of Peltier and Micheron[23] and the review by Gunter,[26] which should be consulted for the original references.

Parameters for $BaTiO_3$ are more difficult to obtain. We use the large r_{42} electro-optic coefficient for our comparisons because many of the most exciting new processes discovered in $BaTiO_3$ use orientations which exploit this coefficient. To our knowledge no separate measurement of photoionization cross section and donor number density has been made in $BaTiO_3$, but for the calculations performed here the absorption coefficient, $\alpha = 0.3\ cm^{-1}$ at $\lambda \approx 0.5\ \mu m$,[28] is sufficient. The trap number density is measured from grating decay times.[15]

The recombination coefficient and mobility in $BaTiO_3$ are difficult to obtain. Mobilities of 2.10^{-4} [30] to 0.5 cm^2/Vs [29] have been measured in $BaTiO_3$. The dielectric relaxation time measured by Feinberg et al.,[15] gives the ratio γ_R/μ, if ε and α are known. Also, the short pulse observations in $BaTiO_3$ [31] suggest that the recombination time is of the order of a nanosecond. The recombination coefficient of $5 \cdot 10^{-8}$ is consistent with a mobility of 0.5 cm^2/Vs and the other observations. Mobilities as low as $2 \cdot 10^{-4}\ cm^2/Vs$ seem completely inconsistent with the photorefractive observations.[15,31] There is, however, still one problem with this set of values. The measured value of $\mu = 0.5\ cm^2/Vs$ is an electron mobility, while Feinberg et al.,[15] found that the sign of the moving charges in their $BaTiO_3$ sample was positive, and in general one expects the hole mobility to be considerably smaller than the electron mobility.

Table 2. Materials Parameters for BSO and $BaTiO_3$

Parameter	Symbol	Units	BSO	$BaTiO_3$
Background index	n_b	-	2.5^a	2.4^a
Dielectric constant	ε	-	56^a	4300^a
Electro-Optic coefficient	γ_{ij}	pm/V	5^a $_{33})$	168 $1640^e(r_{42})$* $80^e(r_{33})$*
Donor number density	N_D	cm^{-3}	10 [illegible]	---+
Trap number density	N_A	cm^{-3}	10^{16c}	$2 \cdot 10^{16c}$
Photocross-section	s	cm^2	$1.6 \cdot 10^{-19b}$	---+
Recombination coefficient	γ_R	cm^3/s	$2 \cdot 10^{-11b}$	$5 \cdot 10^{-8}$
Mobility	μ	cm^2/Vs	0.03^b	0.5,

a Gunter [26]

b Peltier and Micheron [23]

c Feinberg et al. [15]

d Bursian et al. [29]

e Landolt-Bornstein [32]

* Unclamped value. Clamped values 820, 28

+ $s(N_D-N_A) = \alpha \approx 0.3$ [28] at $\lambda \approx 0.5$ μm

REFERENCES

1. D.L. Staebler and J.J. Amodei, J. Appl. Phys. 43, 1042 (1972).
2. D.L. Staebler and W. Phillips, Appl. Opt. 13, 788 (1974).
3. D. von der Linde and A.M. Glass, Appl. Phys. 8, 85 (1975).
4. J.P. Huignard and J.P. Herriau, Appl. Opt. 17, 2671 (1978).
5. J. Feinberg, Opt. Lett. 5, 331 (1980).
6. L. Pichon and J.P. Huignard, Opt. Comm. 36, 277 (1981).
7. J.O. White and A. Yariv, Appl. Phys. Lett. 37, 5 (1980).
8. J.P. Huignard, J.P. Herriau, P. Aubourg, and E. Spitz, Opt. Lett. 4, 21 (1979).
9. J.O. White, M. Cronin-Golomb, B.Fischer, and A. Yariv, Appl. Phys. Lett. 40, 450 (1982).
10. J. Feinberg, Opt. Lett. 7, 486 (1982).
11. P.N. Gunter, Opt. Lett 7, 10 (1982).
12. M.D. Levenson, K.M. Johnson, V.C. Hanchett and K. Chiang J. Opt. Soc. Am. 71, 737 (1981).
13. N. Kukhtarev, V.B. Markov and S.G. Odulov, Opt. Comm. 23, 338 (1977).
14. N.V. Kukhtarev, V.B. Markov, S.G. Odulov, M.S. Soskin and V.L. Vinetskii, Ferroelectrics 22, 949 and 961 (1979).
15. J. Feinberg, D. Heiman, A.R. Tanguay, Jr., and R.W. Hellwarth, J. Appl. Phys. 51, 1297 (1980).
16. A. Marrakchi and J.P. Huignard, Appl. Phys. 24, 131 (1981).
17. C.-T. Chen, D.M. Kim and D. von der Linde, IEEE J. Quantum Electron. QE-16, 126 (1980).
18. J.P. Hermann, J.P. Herriau, and J.P. Huignard, Appl. Opt. 20, 2173 (1981).
19. L.K. Lam, T.Y. Chang, J. Feinberg and R.W. Hellwarth, Opt. Lett. 6, 475 (1981).
20. N.V. Kukhtarev, Sov. Tech. Phys. Lett. 2, 438 (1976).
21. J.J. Amodei, RCA Review 32, 185 (1971).
22. L. Young, W.K.Y. Wong, M.L.W. Thewalt and W.D. Cornish, Appl. Phys. Lett. 24, 264 (1974).
23. M. Peltier and F. Micheron, J. Appl. Phys. 48, 3683 (1977).
24. G.C. Valley, Erase rates in photorefractive materials with two photoactive species, submitted to Applied Optic (1983).
25. G.C. Valley, Short pulse grating formation in photorefraction materials submitted to IEEE J. Quantum Electron (1983).
26. P. Gunter, Holography, coherent light amplification and optical phase conjugation with photorefractive materials to be published in Phys. Reports (1982).
27. H. Kogelnik, Bell Syst. Tech. J. 48 2909 (1969).
28. M. Minden, Hughes Research Laboratories, private communication (1982).
29. E.V. Bursian, Ya.G. Girshberg, and A.V. Ruzhnikov, Phys. Stat. Sol. (b), 74, 689 (1976).
30. G.A. Cox and R.M. Tredgold, Phys. Lett. 11, 22 (1964).
31. L.K. Lam, T.Y. Chang, J. Feinberg, and R.W. Hellwarth, Opt. Lett. 6, 475 (1981).

32. Landolt-Bornstein, ed. by K.H. Hellwege, Numerical Data and Functional Relationships in Science and Technology, New Series (Springer-Verlag, Berlin 1979), Vol. 11.
33. J. Feinberg and R.W. Hellwarth, Opt. Lett. 5, 519 (1980).
34. J. Feinberg, Opt. Lett. 7, 486 (1982).

ACKNOWLEDGEMENTS

We thank Ms. R.A. Mullen and Drs. R.W. Hellwarth, J.F. Lam, and M. Sparks for helpful conversations.

APPENDIX D

TWO-WAVE MIXING IN THE TRANSIENT REGIME

Juan Lam

The volume grating solutions developed by Kukhtarev provide the steady state and step function response for the space charge density and space charge field, but are not directly applicable for pulsed excitation. In this study we present a model for grating formation with pulsed excitation. This model also applies to two-wave mixing and four-wave mixing where nondepleted, strong pumps and a weak probe wave are involved.

Our model relies on the following assumptions:

1. The pumps are cw.
2. The incident probe is a pulse of duration, τ_p, and magnitude, $\mathscr{E}_p$.
3. The interaction geometry is as shown in Figure D-1. For DFWM, all three input waves are present. For two-wave mixing, we shall set $\mathscr{E}_b=0$.
4. The pump waves are nondepleted during the nonlinear interaction.

The response of the material to the three input waves can be described in terms of the charge transport equations of Kukhtarev (as reviewed in Appendices B and C), in the absence of applied dc electric fields:

$$\frac{\partial n}{\partial t} + \frac{1}{q} \nabla \cdot \vec{J} = S \tag{1}$$

$$\frac{\partial N_+}{\partial t} = S \tag{2}$$

$$\nabla \cdot \vec{E}_{sc} = \frac{q}{\varepsilon \varepsilon_o} [n + N_+(O) - N_+] \tag{3}$$

$$\vec{J} = q \mu n \vec{E}_{sc} - q D \nabla n \tag{4}$$

$$S = \gamma_I I(N_D-N_+) - \gamma_r n N_+ \tag{5}$$

$$I = \frac{c\varepsilon_o}{4} \left|\sum_\alpha \left(\vec{\mathscr{E}}_\alpha e^{i\phi_\alpha} + \vec{\mathscr{E}}_\alpha e^{-i\phi_\alpha}\right)\right|^2 \tag{6}$$

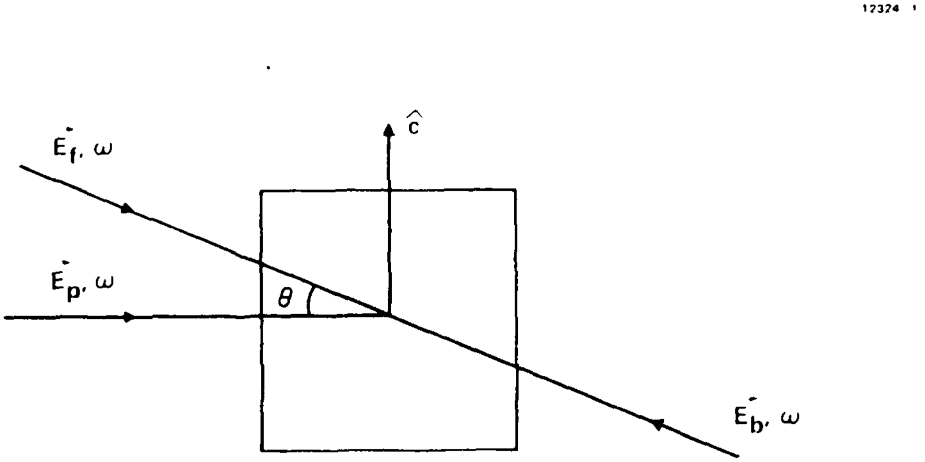
12324 1
$\hat{c}$
$\vec{E}_f, \omega$
$\vec{E}_p, \omega$
θ
$\vec{E}_b, \omega$

Figure D-1. Experimental geometry. E_f, E_b and E_p are the forward pump, backward pump, and probe waves, respectively.

with $\phi_\alpha = \vec{k}_\alpha \cdot \vec{r} - \omega t$. The quantities n and N_+ are the electron and ion densities, respectively. q is the charge of the electron, $\vec{J}$ is the electronic current density, μ and D are the electron drift and diffusion coefficients, respectively. γ_I and γ_e are the photo-ionization and recombination constants, respectively. I is the intensity of the optical radiation, and ε is the static dielectric constant.

The initial conditions for our problem can be stated as follows. In the absence of the probe wave, the space charge field and the electronic current density are null. These conditions yield the steady state electron and ion densities in the presence of the pump waves only and are given by

$$n^{(0)} + N_+(0) - N_+^{(0)} = 0 \qquad (7)$$

$$N_+^{(0)} = \frac{N_+(0)}{2} - \frac{\Gamma_p}{2\gamma_r} \pm \left(\frac{N_+(0)}{2} - \frac{\Gamma_p}{2\gamma_r}\right)^2 + \frac{\Gamma_p}{\gamma_r} N_D \, , \qquad (8)$$

where $\Gamma_p = \gamma_I I_o$ is the photo-ionization rate and $I_o = c\varepsilon_o/2 \sum_{pump} |\mathcal{E}|^2$. In the presence of the probe wave, the charge transport equations are solved in the perturbation regime, consistent with the assumption of non-depleted pump waves. The first order equations for the electron and ion densities are

$$\frac{\partial n^{(1)}}{\partial t} + (\Gamma_o + \Gamma_D + \Gamma_e) n^{(1)} + (\Gamma_p + \Gamma_N - \Gamma_o) N_+^{(1)} = \Gamma_p \frac{I_1}{I_o} (N_D - N_+^{(0)}) \qquad (9)$$

$$\frac{\partial N_+^{(1)}}{\partial t} + (\Gamma_p + \Gamma_N) N_+^{(1)} + \Gamma_e \, n^{(1)} = \Gamma_p \frac{I_1}{I_o} (N_D - N_+^{(0)}) \qquad (10)$$

where $\Gamma_o = q\mu n^{(0)}/\varepsilon\varepsilon_o$ is the dielectric relaxation rate, $\Gamma_D = D\,|\vec{k}_f-\vec{k}_p|^2$ is the electron diffusion rate, $\Gamma_N = \gamma_r n^{(0)}$ is the ion recombination rate and $\Gamma_e = \gamma_r N_+^{(0)}$ is the electron recombination rate. Equations (9) and (10) form a set of linear coupled first order differential equations subject to the initial condition that in the absence of the probe wave, $\mathscr{E}_p$, $n^{(1)} = 0 = N_+^{(1)}$. The solution for Equation (9) and (10) can be obtained by means of Laplace transform techniques. for our case we have chosen the time dependence of the probe wave to be given by

$$\mathscr{E}_p(t) = \mathscr{E}_o\,\{H(t) - H(t-\tau_p)\} \quad , \tag{11}$$

where ε_o is a constant amplitude and $H(t-t')$ is the Heavyside function. The application of the Laplace transform technique yields the following solution for the first order space charge field, E_{sc}:

$$\vec{E}_{sc} = -i\,\frac{k_f-k_p}{|\vec{k}_f-\vec{k}_p|}\,\frac{q}{\varepsilon\varepsilon_p}\,\left(n^{(1)}-N_+^{(1)}\right) \quad , \tag{12}$$

where

$$n^{(1)}-N_+^{(1)} = -\,\Gamma_p\Gamma_D\,\frac{I_1}{I_o}\,\left(N_D-N_+^{(0)}\right)$$

$$\times\ \frac{1}{s_1s_2} + \frac{1}{s_1-s_2}\left[\frac{1}{s_1}\,e^{s_1t} - \frac{1}{s_2}\,e^{s_2t}\right]$$

$$- H(t-\tau_p) \; [\frac{1}{s_1 s_2} + \frac{1}{s_1 - s_2} \; [\frac{1}{s_1} e^{s_1(t-\tau_p)} - \frac{1}{s_2} e^{s_1(t-\tau_p)}] \tag{13}$$

and

$$s_{1,2} = -\frac{A}{2} \pm \quad (\frac{A}{2})^2 - B \tag{14}$$

$$A = \Gamma_o + \Gamma_D + \Gamma_e + \Gamma_p + \Gamma_N \tag{15}$$

$$B = (\Gamma_N + \Gamma_p)(\Gamma_o + \Gamma_D) + \Gamma_e \Gamma_o \quad . \tag{16}$$

To show that the solution has the appropriate limits, we consider the cases at $t=0$ and at $t \rightarrow \infty$. At $t=0$,

$$n^{(1)} - N_+^{(1)} \sim \frac{1}{s_1 s_2} + \frac{1}{s_1 - s_2} \left(\frac{1}{s_1} - \frac{1}{s_2}\right) = 0 \quad . \tag{17}$$

And at $t \rightarrow \infty$,

$$n^{(1)} - N_+^{(1)} \propto \frac{1}{s_1 s_2} - \frac{1}{s_1 s_2} = 0 \quad . \tag{18}$$

These results are consistent with the fact that in the absence of ε_p the first order densities are small. Furthermore, the steady state result can be obtained by letting $\tau_p \rightarrow \infty$, and $t >> s_1^{-1}$ and s_2^{-1}. In the case,

$$n^{(1)} - N_+^{(1)} = -\Gamma_o \Gamma_D \frac{I_1}{I_o} \left[\frac{(N_D - N_+^{(0)})}{s_1 s_2}\right] \quad . \tag{19}$$

The space charge field, E_{sc}, gives rise to a spatial modulation in the refractive index by means of the electro-optic effect. The scattering of the forward pump, ε_f, in the case of two-wave mixing (or backward pump, ε_b, in the case of four-wave mixing) from the spatial modulation generates the signal wave, ε_s. The signal wave will have the same time dependence as the space charge field, provided that the nonlinear medium length, L, is thin enough to satisfy the condition,

$$L \ll \frac{c}{n_o} \tau_p \quad , \qquad (20)$$

where c is the speed of light and n_o is the host index of refraction.

558 OPTICS LETTERS / Vol. 7, No. 11 / November 1982

APPENDIX E

Demonstration of image transmission through fibers by optical phase conjugation

Gilmore J. Dunning and R. C. Lind

Hughes Research Laboratories, 3011 Malibu Canyon Road, Malibu, California 90265

Received May 24, 1982; revised manuscript received September 1, 1982

We have demonstrated image transmission through a multimode fiber by using optical phase conjugation. By using the wave-front reversal properties of degenerate four-wave mixing, we have compensated for the degradation of the image that is due to modal dispersion in a fiber.

We have demonstrated the transmission of images through multimode fibers by using phase conjugation.[1] The transmission of spatial information through fibers is degraded because of modal dispersion. To compensate for this degradation, Yariv[2] proposed the use of the wave-front-reversal property of certain nonlinear optical techniques. In this Letter we describe the first reported demonstration of image transmission and restoration using the nonlinear optical process of degenerate four-wave mixing (DFWM). In the past, other techniques were used for the transmission of images through fibers. These approaches include using fibers of a precise length,[3–6] lenslike index variations,[7,8] and holographic filters.[9,10]

In order to understand image degradation by transmission in an optical fiber it is necessary first to consider modal dispersion. Following the analysis by Yariv,[2] any general input picture field can be expressed as the sum of the bound modes and unbound modes of the fiber:

$$f_0(x, y, z = o, t) = \sum_{m,n=0}^{M,N} A_{mn} E_{mn}(x, y) \exp(i\omega t) + \text{radiation modes}. \qquad (1)$$

If we let the field propagate through a fiber of length L and assume that most of the energy is carried in the bound modes, the resultant output field is given by

$$f_1(x, y, z = L, t) = \sum_{m,n=0}^{M,N} A_{mn} E_{mn}(x, y) \times \exp[i(\omega t - \beta_{mn} L)]. \qquad (2)$$

The energy that is lost because of radiation will cause a slight reduction in resolution. Also, in this analysis, we have assumed no differential modal attenuation or mode mixing. In order for the output field to be proportional to the input field the following condition must be satisfied:

$$\beta_{mn} L = 2\pi I_{m,n}, \qquad (3)$$

where β_{mn} is the propagation constant associated with mode m, n and $I_{m,n}$ is an integer. Equation (3) cannot be satisfied for all modes simultaneously for an arbitrary value of L. By using phase conjugation one can reconstruct the original input field. If the beam transmitted through the fiber is first conjugated and then transmitted through an identical fiber, the original input image will be formed at the output of the second fiber. This can be seen by taking the conjugate of Eq. (2) and propagating the field through an identical fiber of length L (or back through the same fiber):

$$f_2(x, y, z = L, t) = \sum_{m,n=0}^{M,N} A_{mn}{}^* E_{mn}(x, y) \times \exp[i(\omega t + \beta_{mn} L)]. \qquad (4)$$

The output after traversing an identical fiber or retraversing the same fiber is

$$f_3(x, y, z = o, t) = f_3(x, y, z = 2L, t) = \sum_{m,n=0}^{M,N} A_{mn}{}^* E_{mn}(x, y) \exp(i\omega t), \qquad (5)$$

which is seen to be proportional to the input field in Eq. (1).

In the present experiments a single fiber was used. The purpose of these experiments was to show that phase conjugation can compensate for modal distortions introduced by a fiber.

The demonstration was accomplished by utilizing a multimode (85-μm diameter, 1.75-m-long) step-index fiber. The output of a krypton laser (6471 Å) was used to backilluminate a portion of a U.S. Air Force resolution chart that was imaged at the input end of the fiber. The fiber output was directed into a crystal of barium titanate ($BaTiO_3$) in which DFWM was used to generate the phase-conjugate signal. The phase-conjugate signal then retraversed the same fiber, resulting in a reconstructed image of the resolution chart.

The geometry employed for the four-wave mixing experiments in this work is similar to the high-reflectivity configuration for $BaTiO_3$ of Feinberg and Hellwarth.[11] It consists of two counterpropagating pumps E_f and E_b and a probe wave E_p (which is the beam with the image information imposed upon it), incident upon the nonlinear medium. These beams interact to generate the phase-conjugate signal E_s. A schematic of the experiment is shown as Fig. 1. The krypton-ion laser operates in a single longitudinal mode, giving coherence lengths of the order of 10 m. Because of crystal orien-

Reprinted from Optics Letters, Vol. 7, page 558, November 1982

Copyright © 1982 by the Optical Society of America and reprinted by permission of the copyright owner

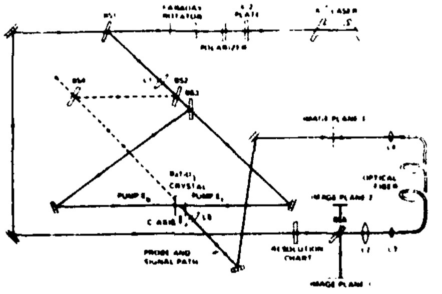

Fig. 1. Schematic of experiment for image transmission through an optical fiber.

tation, *p* polarization of the input beams is required in our experiments. This polarization is desired to couple into the large r_{42} electro-optic coefficient of $BaTiO_3$ ($r_{42} = 820 \times 10^{-12}\ mV^{-1}$). Therefore a λ/2 plate and a Faraday rotator were used to rotate the plane of polarization of the krypton laser. The Faraday rotator was also used in conjunction with a polarizer to prevent any return beams from entering the laser and spoiling the single-mode operation. Beam splitter BS1 picks off the pump beams. An f = 100-cm lens (L1) was used to reduce the pump beam in the crystal to a size that optimized the interaction length and probe overlap. Beam splitter BS2 generated a secondary probe signal that was used to optimize the crystal orientation. Beam splitter BS3 was used to generate the individual counterpropagating pumps. The pumps typically have a power ratio of 2:1 (I_B = 7.1 mW, I_f = 3.2 mW). The *throughput of beam splitter BS1 was the probe beam* propagated through the fiber. This probe beam was expanded by a beam-expanding telescope to illuminate the Air Force resolution chart. Following the resolution chart is a beam splitter (BS5), which is used to pick off the return signal that forms the reconstructed image on a film plane at image plane 1. An f/1, 7.6-cm focal-length relay lens (L2) was used to capture the light diffracted by the patterns of the resolution chart. Lenses L3 and L4 are 7× objectives with 0.20 N.A. and are used to couple the light into and out of the Corning fiber. With an N.A. of 0.184, theoretically on the order of 10^4 modes propagate at the wavelength being used. The second microscope objective (L4) quasi-collimates the output beam from the fiber. A 5-cm focal-length lens (L5) is used to reduce the probe beam to a diameter smaller than the diameter of the pump beams inside the crystal. Typically, the angle between the forward pump and the probe inside the crystal is 7°, and the grating vector makes an angle of 18° with respect to the *c* axis, a condition that yields the highest reflectivity. By using this geometry with the crystal in air, we have obtained reflectivities in excess of 150%. These large returns have enabled us to reconstruct the image and also to show image amplification.

The mutual-coherence requirements between the probe (E_p) and the pump (E_f) are important in the present experiment. It has been well established that a holographic analogy exists in four-wave mixing. In particular, one can think of the interference of the probe E_p and the pump E_f as generating a volume hologram in the $BaTiO_3$, which is then read out by pump E_b to generate the conjugate wave E_s. This would suggest that, for the experimental setup used, the coherence length of the laser must be at least as long as the path-length difference between the probe E_p and the pump E_f (which, for our experiments, is ~4 m).

In fact, the above mutual-coherence requirement strictly applies only if the time response of the nonlinear medium is infinite and approximately applies when one uses slowly responding materials, such as $BaTiO_3$ (100 msec). However, if nonlinear materials that respond instantaneously are used, then this requirement is altered. To understand this, recall that the product of the response time τ and the frequency bandwidth $\Delta\nu$ (or the pump–probe frequency difference) is unity. Thus, when $BaTiO_3$ is used, $\Delta\nu \sim 10$ Hz is required. If a material, such as sodium vapor, with nanosecond response times is used, a bandwidth of a few gigahertz is allowed (more precisely, $\Delta\nu$ is given by the generalized Rabi frequency[12]). This means that interference will occur for any length fiber as long as the frequency difference between the probe and the pump is less than a few gigahertz, which is easy to achieve by using stabilized dye lasers.

The results of this experiment are shown in Fig. 2. The first photograph shows the input image of a portion of a U.S. Air Force resolution chart. The second photograph shows the output at the end of the fiber. The output is typical of a highly multimode fiber in which a large number of modes are excited. From the output, it is impossible to discern that any spatial information has been transmitted through the fiber. The last photograph shows the image that has been reconstructed after double passing the fiber (approximately 25-μm spacings are shown).

An interesting issue related to the fidelity of the image reconstruction is the polarization. Typical commercially available fibers do not preserve polarization; therefore, when linearly polarized light is fed into a fiber, the output is randomly polarized. In our DFWM experiments, only the *p*-polarization component is conjugated. This polarization is scrambled on retraversing the fiber. Because the input image is reconstructed, we speculate that the information carried by each polarization component is similar.

Another test of the fidelity of the phase-conjugation

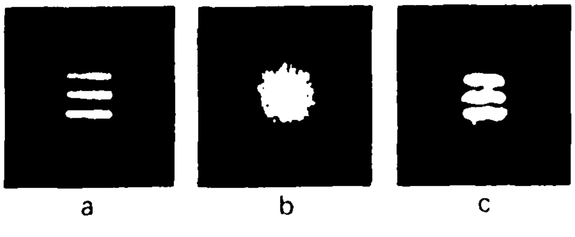
a b c

Fig. 2. Demonstration of image transmission through an optical fiber: a, input image resolution pattern; b, output after a single pass through the fiber; c, reconstruction of resolution pattern after output has been phase conjugated and retraverses fiber.

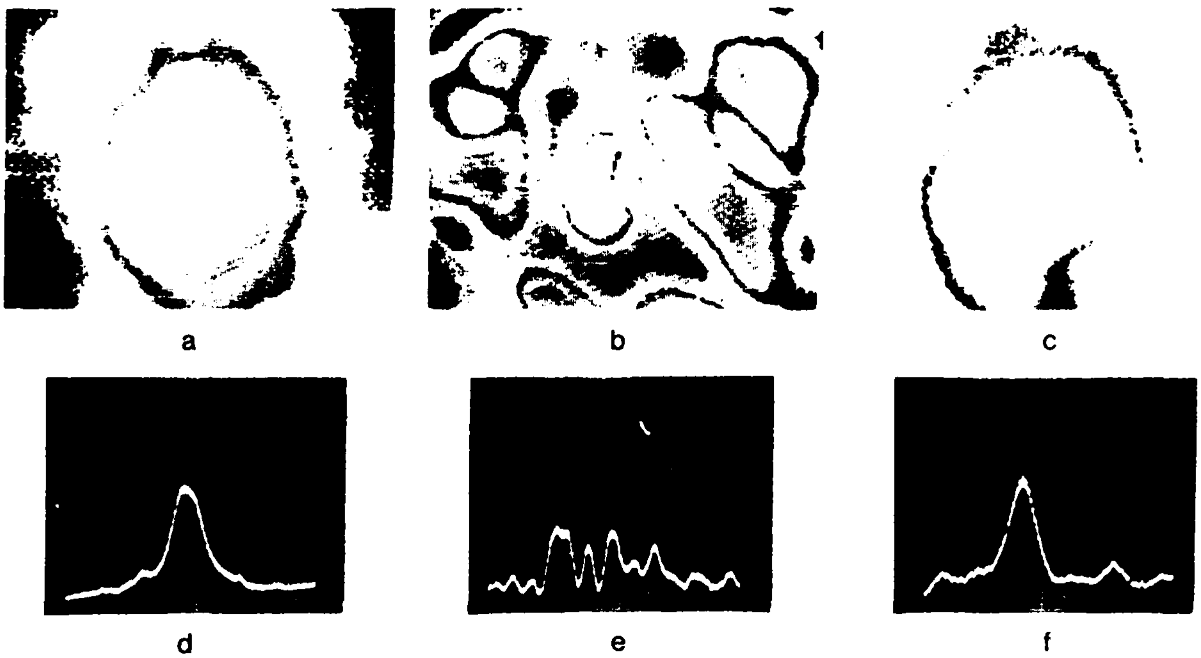

Fig. 3. Photographs of the far-field intensity distribution for a, input beam; b, single pass through fiber; c, corrected beam. Oscilloscope traces d, e, and f are the corresponding cross sections.

process is to measure its ability to reproduce a Gaussian input wave. In these experiments the beam passes through the fiber, is conjugated, retraverses the fiber, and is examined in the far field. The beam to be studied was monitored at the back focal plane of a 1-m focal-length lens. This image was magnified and then projected onto the vidicon element of a television camera. The video signal was processed by an image analyzer that produces two outputs. The first is a display of intensity versus x–y position. The video signal is level sliced, and each level is assigned a color. This output is displayed on a color television screen. The second format is an intensity profile. A cursor permits one to display a cross section of the far-field pattern on an oscilloscope. The results of the far-field experiments are shown in Fig. 3. The input beam is monitored at image plane 2 and is typical of an apodized Gaussian beam (Fig. 3a). The output from the fiber, monitored at image plane 3, is shown in Fig. 3b. It is seen to be very irregular in intensity, indicating the severe aberrations introduced by the fiber. This output is then conjugated and retraverses the fiber. The reconstructed beam is monitored at image plane 1 and is seen very nearly to reconstruct the initial input beam (Fig. 3c). The corresponding intensity cross sections 3d, 3e, and 3f were taken at the position of the horizontal line in Figs. 3a, 3b, and 3c.

In conclusion, we have demonstrated the ability of phase conjugation to compensate for modal dispersion in optical fibers. These experiments were done for a static two-dimensional image, but the technique has a wider range of applicability. In particular, the real-time correction capability for modal dispersion is limited only by the time response of the phase-conjugate medium. Many materials have the nanosecond response time exemplified by sodium vapor. These fast response times not only allow for transmission at a high data rate but also correct for dynamic thermal and mechanical stresses in the fiber. In addition, since gain can be achieved by using DFWM, the phase conjugator could be used as an optical amplifier in a transmission line.

We acknowledge valuable discussions with D. G. Steel, A. Yariv, M. Rourke, and C. Giuliano. We thank A. Pepitone and J. Shuler for their help in the assembly of the experimental apparatus. This work was supported in part by Rome Air Development Center under contract no. 19628 80-C-0185.

References

1. G. Dunning and R. Lind, in *Digest of Topical Meeting on Optical Fiber Communication and Conference on Lasers and Electro-Optics* (Optical Society of America, Washington, D.C., 1982), paper FO3.
2. A. Yariv, J. Appl. Phys. Lett. 28, 88 (1976).
3. R. Ulrich, Opt. Commun. 13, 259 (1975).
4. R. Ulrich and G. Ankele, Appl. Phys. Lett. 27, 337 (1975).
5. E. Grigor'eva and A. Semenov, Sov. J. Quantum Electron. 8, 1063 (1978).
6. L. Rivlin and A. Semenov, Laser Focus 17(2), 82, (1981).
7. T. Uchida, M. Furukawa, I. Kitano, K. Koizumi, and H. Matsumura, IEEE J. Quantum Electron. QE-6, 606 (1970).
8. K. Iga and N. Yamamoto, Appl. Opt. 16, 1305 (1977).
9. U. Levy and A. Friesem, Appl. Phys. Lett. 32, 29 (1978).
10. U. Levy and A. Friese Opt. Commun. 30, 163 (1979).
11. J. Feinberg and R Hei arth, Opt. Lett. 5, 519, (1980); 6, 257 (E) (1981).
12. D. Steel and R. C. Lind, pt. Lett. 6, 587 (1981).

MISSION
of
Rome Air Development Center

RADC plans and executes research, development, test and selected acquisition programs in support of Command, Control Communications and Intelligence (C^3I) activities. Technical and engineering support within areas of technical competence is provided to ESD Program Offices (POs) and other ESD elements. The principal technical mission areas are communications, electromagnetic guidance and control, surveillance of ground and aerospace objects, intelligence data collection and handling, information system technology, ionospheric propagation, solid state sciences, microwave physics and electronic reliability, maintainability and compatibility.

Printed by
United States Air Force
Hanscom AFB, Mass. 01731

END

FILMED

DT